



US 20060213251A1

(19) United States

(12) Patent Application Publication (10) Pub. No.: US 2006/0213251 A1  
Rinzler et al. (43) Pub. Date: Sep. 28, 2006

(54) CARBON NANOTUBE FILMS FOR  
HYDROGEN SENSING

(22) Filed: Mar. 24, 2005

(75) Inventors: Andrew Gabriel Rinzler, Newberry,  
FL (US); Jennifer Ann Sippel-Oakley,  
Gainesville, FL (US); Byoung S. Kang,  
Gainesville, FL (US); Hung-Ta Wang,  
Gainesville, FL (US); Fan Ren,  
Gainesville, FL (US); Stephen J.  
Pearton, Gainesville, FL (US)

Correspondence Address:  
**AKERMAN SENTERFITT**  
**P.O. BOX 3188**  
**WEST PALM BEACH, FL 33402-3188 (US)**

(73) Assignee: University of Florida Research Foundation, Inc.

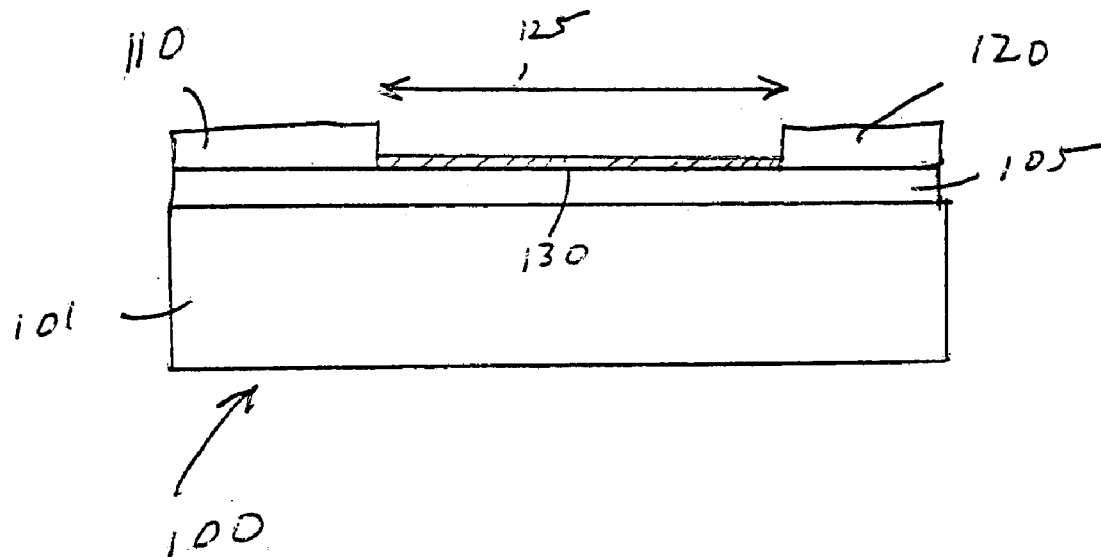
(21) Appl. No.: 11/089,311

Publication Classification

(51) Int. Cl. G01N 7/00 (2006.01)  
(52) U.S. Cl. ..... 73/23.2

(57) ABSTRACT

A multi-layer H<sub>2</sub> sensor includes a carbon nanotube layer, and a ultra-thin metal or metal alloy layer in contact with the nanotube layer. The ultra-thin metal or metal alloy layer is preferably from 10 to 50 angstroms thick. An electrical resistance of the layered sensor increases upon exposure to H<sub>2</sub> and can provide detection of hydrogen gas (H<sub>2</sub>) down to at least 10 ppm. The metal or metal alloy layer is preferably selected from the group consisting of Ni, Pd and Pt, or mixtures thereof. Multi-layered sensors and can be conveniently operated at room temperature.



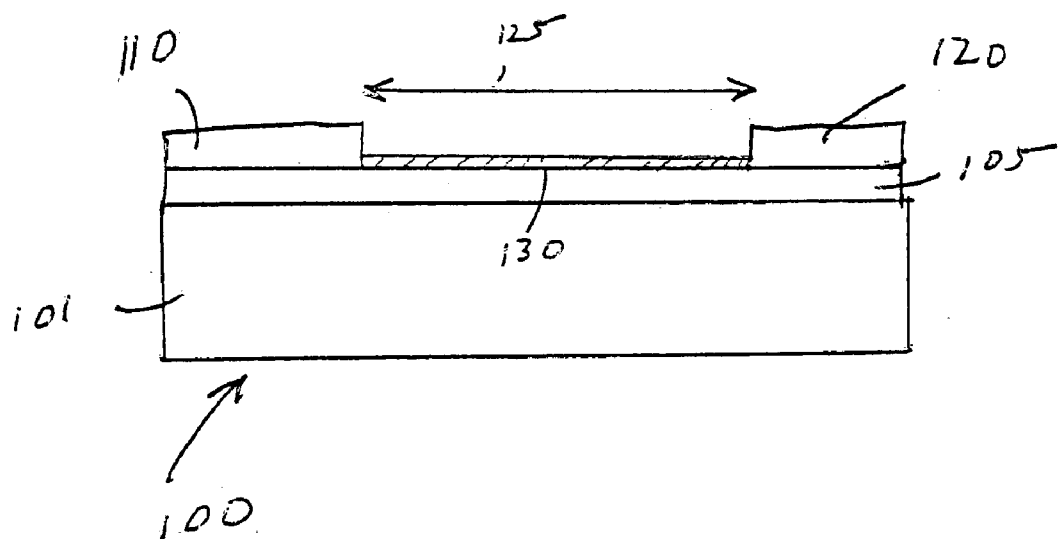


FIG. 1

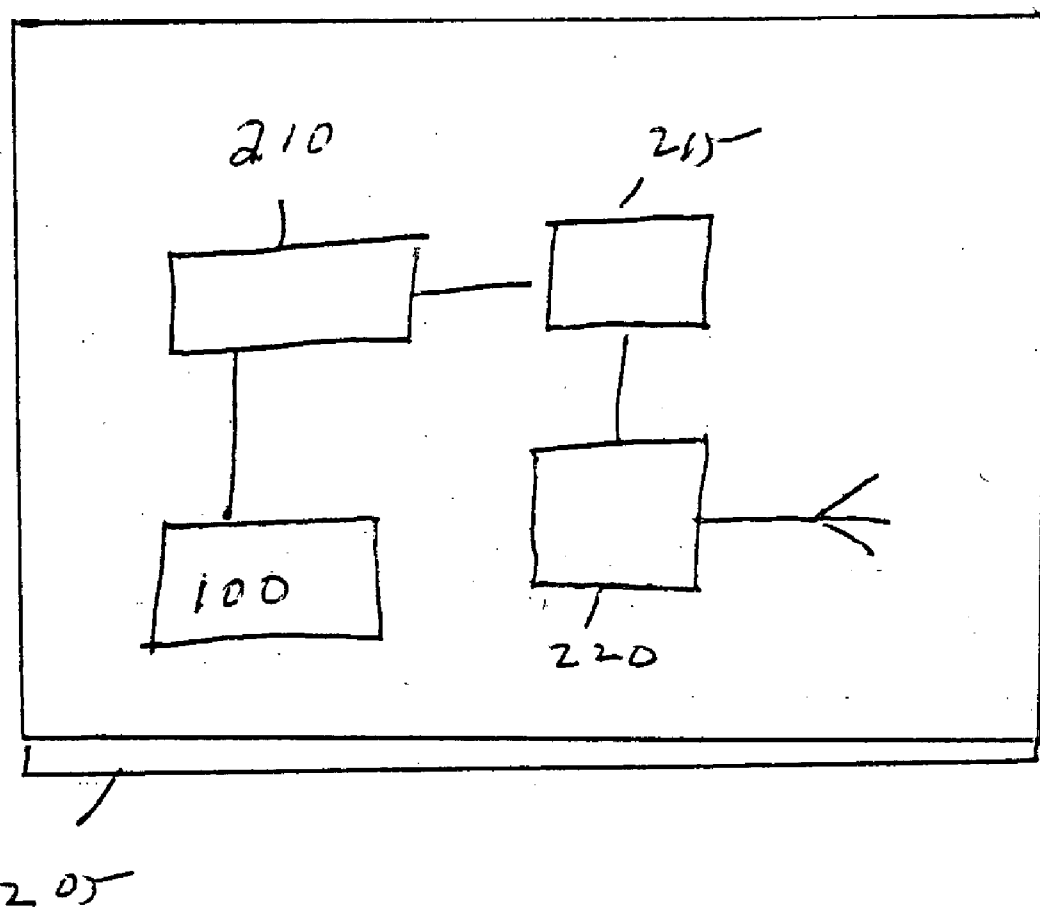


FIG. 2

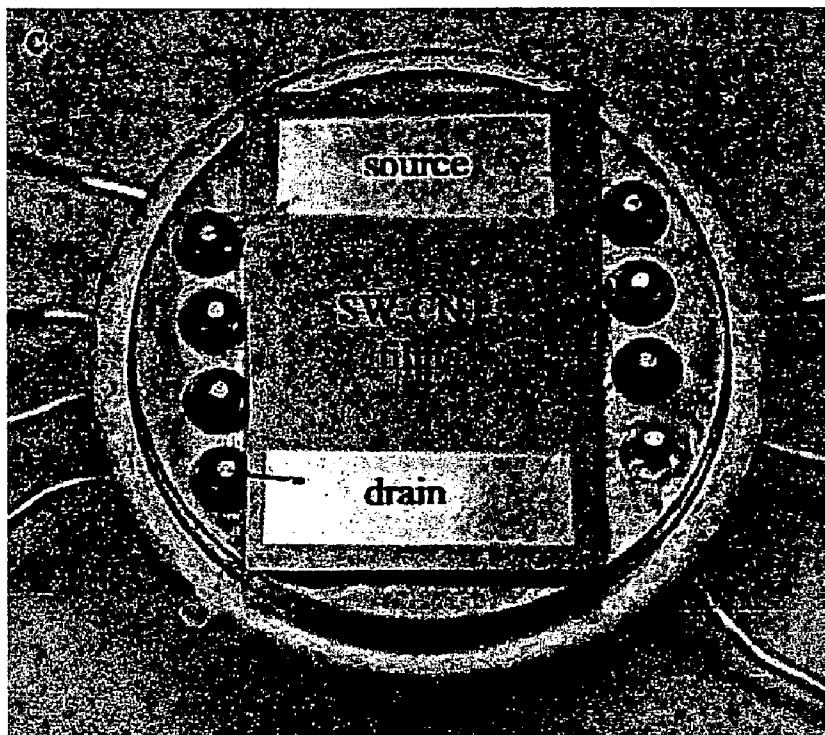


FIG. 3

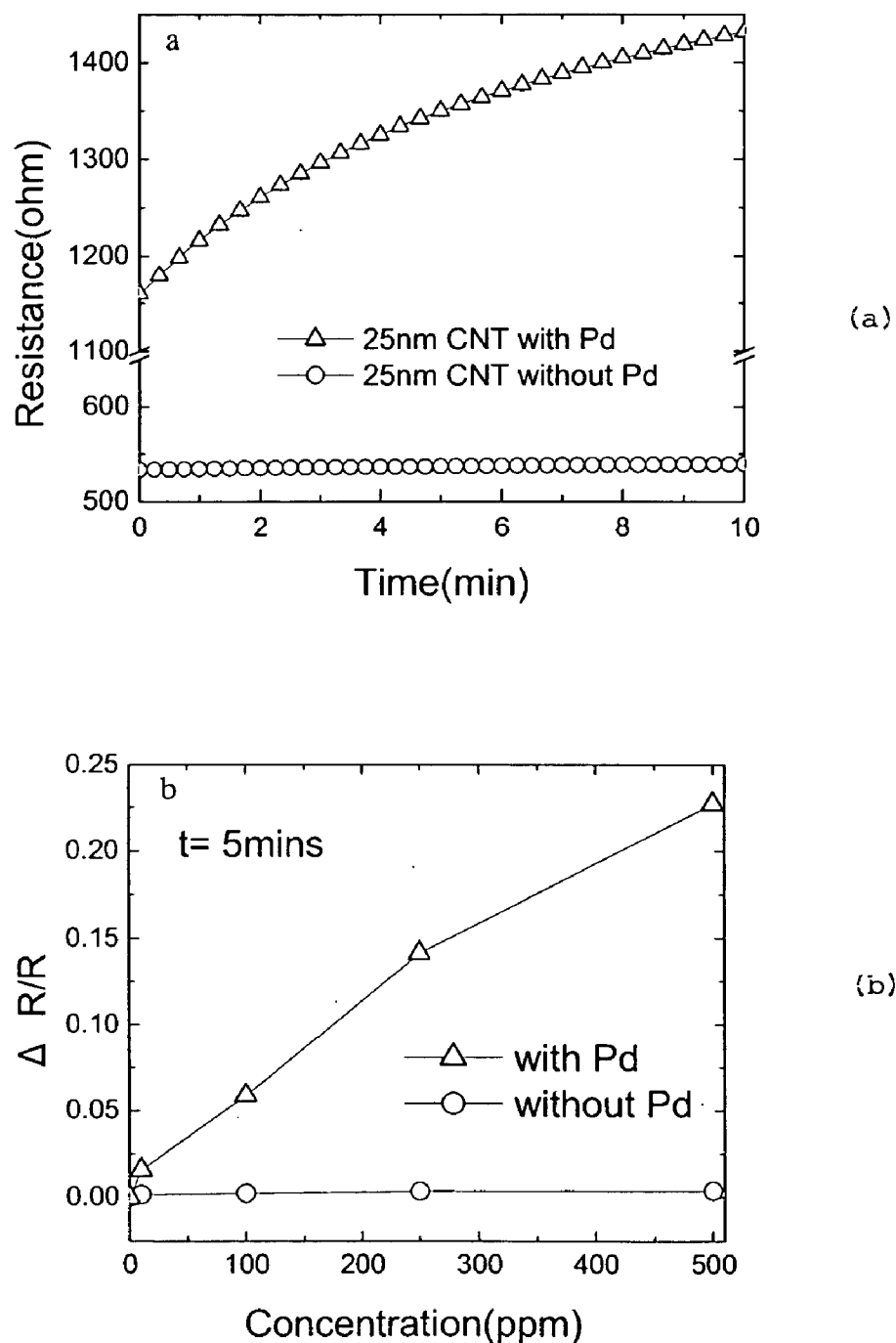


FIG. 4

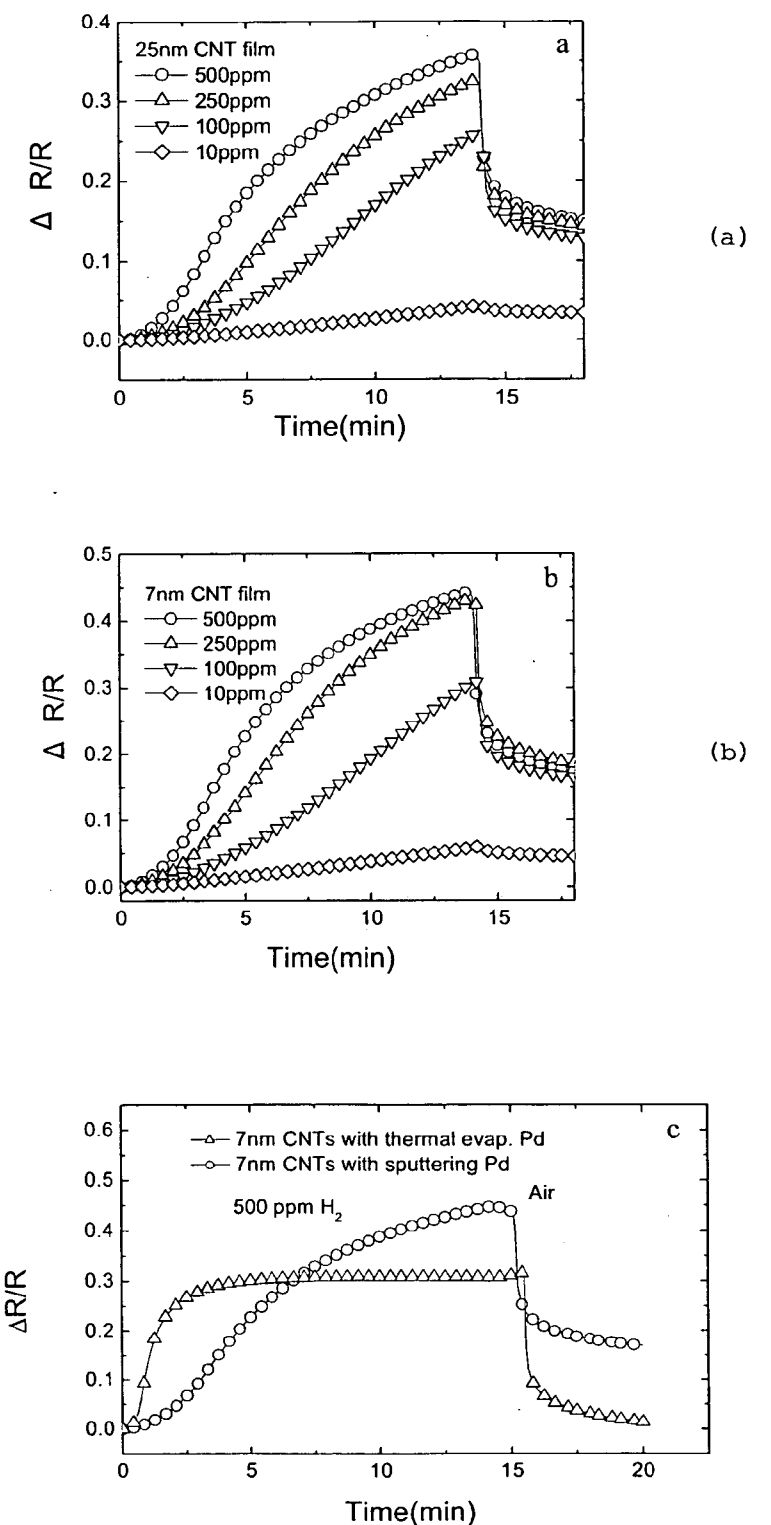


FIG. 5

## CARBON NANOTUBE FILMS FOR HYDROGEN SENSING

### STATEMENT REGARDING FEDERALLY SPONSORED RESEARCH OR DEVELOPMENT

[0001] The U.S. government may have certain rights to the invention based on AFOSR grant number F49620-03-1-0370; NSF(CTS-0301178), NASA Kennedy Space Center Grant NAG 10-316, ONR (N00014-98-1-02-04), and NSF DMR 0400416.

### CROSS-REFERENCE TO RELATED APPLICATIONS

[0002] Not applicable.

### FIELD OF THE INVENTION

[0003] The invention relates to multi-layer hydrogen sensors which include a carbon nanotube layer.

### BACKGROUND

[0004] Ongoing efforts towards a hydrogen-based transportation economy have stimulated an increased need for compact, reliable, low cost, low power consumption hydrogen sensors for monitoring and safety. These are also required for spacecraft powered by hydrogen fuel cells where long-duration space flights can last for years and potentially decades.

[0005] Single walled carbon nanotubes (SWNTs) have exhibited a charge transport sensitivity to their chemical environment, making them attractive for chemical sensing applications. In one paper (Y. Lu, J. Li, H. T. Ng, C. Binder, C. Partridge, M. Meyyapan, Chem. Phys. Lett. 391, 344 (2004), a group of researchers showed that by palladium loading the nanotube networks, the devices acquired a ppm level sensitivity for detecting methane, a gas for which the devices were otherwise insensitive. Lu et al. discloses sputter deposition of Pd onto nanotube powder followed by "shaking" and ultrasonic dispersion in purified water and subsequent drop drying across interdigitated microelectrodes. The reproducibility of devices made by such a method leaves much to be desired. For example, the amount of Pd loading was poorly controlled, as was the density of the nanotubes in the drop-dried networks bridging the electrodes of the device.

### SUMMARY

[0006] A multi-layer hydrogen sensor comprises a carbon nanotube comprising layer, and an ultra-thin metal or metal alloy layer disposed on the carbon nanotube comprising layer, wherein an electrical resistance of the layered sensor increases upon exposure to H<sub>2</sub>. The carbon nanotube comprising layer preferably consists essentially of single wall nanotubes (SWNTs).

[0007] As used herein, the phrase "ultra-thin" corresponds to a thickness of from about 0.5 nm to about 10 nm. The ultra-thin layer can be a layer having uniform thickness, or be a sub-percolation layer of metal defined herein as a plurality of discrete, nanoscale metal islands, not in themselves electrically connecting by metal to one another, or a plurality of nanoscale metal islands wherein at least a portion of the nanoscale metal islands are electrically con-

nected other islands by metal. In the case where the metal islands are not electrically connected to form a low resistance electrical path from one end of the sensor to the other, the thickness of the metal islands can be on the order of hundreds of nms, or more, since such an arrangement will not shunt the carbon nanotube comprising active sensing layer.

[0008] The thickness of the ultra-thin metal or metal alloy layer is preferably from 0.5 to 5 nm thick. The ultra-thin metal or metal alloy layer can be selected from Ni, Pd, Pt, Ti, Ag and W, or mixtures thereof. In a preferred embodiment, the ultra-thin metal or metal alloy layer comprises Pd.

[0009] The thickness of the carbon nanotube comprising layer is preferably from 4 to 60 nm, such as from 4 to 10 nm. The interface between the carbon nanotube comprising layer and the ultra-thin metal or metal alloy layer is preferably characteristic of an evaporated interface or other low energy deposition process.

[0010] In a related embodiment that can provide integrated microsensors formable generally using conventional integrated circuit processing steps, the sensor further comprises an integrated circuit substrate, wherein the sensor is disposed on the substrate. At least one electronic device can be disposed on the substrate, the electronic device coupled to an output of the sensor.

[0011] A method of forming a layered hydrogen sensor comprises the steps of providing a substrate, forming an active sensor region on the substrate, the active sensor region comprising a carbon nanotube comprising layer disposed on or under an ultra-thin metal or metal alloy layer, and forming contacts to the active sensor region on either side of the active sensor region. The ultra-thin metal or metal alloy layer can be formed using an evaporation process, or other low energy deposition process.

[0012] The forming step can comprise forming the carbon nanotube comprising layer on a porous support layer, placing the carbon nanotube comprising layer on the porous support layer on the substrate, and then removing the support layer. The support layer can comprises a porous membrane. The nanotube comprising layer on the support layer can be formed using the steps of dispersing a plurality of nanotubes into a solution, the solution including at least one surface stabilizing agent for preventing the nanotubes from flocculating out of suspension, applying the solution to the porous support, and removing the solution, wherein the nanotubes are forced onto a surface of the porous support.

### BRIEF DESCRIPTION OF THE DRAWINGS

[0013] A fuller understanding of the present invention and the features and benefits thereof will be obtained upon review of the following detailed description together with the accompanying drawings, in which:

[0014] FIG. 1 shows an exemplary multi-layer H<sub>2</sub> sensor according to an embodiment of the invention.

[0015] FIG. 2 shows an integrated sensing system including a wireless transmitter on chip, according to an embodiment of the invention.

[0016] FIG. 3 shows a scanned image of the wired up H<sub>2</sub> sensor used to acquire data presented in the Examples described herein.

[0017] FIG. 4(a) shows resistance as a function of time for sensors according to the invention using a 25 nm SWNT layer both with and without Pd coatings, respectively; FIG. 4(b) shows the relative responses or sensitivities ( $\Delta R/R$ ) obtained using a 5 minute exposure to 500 ppm H<sub>2</sub> in N<sub>2</sub>, for the Pd coated sensor.

[0018] FIG. 5(a)-(b) show the switching and recovery characteristics of H<sub>2</sub> sensing, as manifested in the change in  $\Delta R/R$  at fixed applied voltage (0.5V), while FIG. 5(c) compares the exposure/recovery response of sputtered and thermally evaporated Pd layers on 7 nm thick SWNT films.

#### DETAILED DESCRIPTION

[0019] It has been discovered that although electronic transport across pure SWNT films is relatively insensitive to the presence of H<sub>2</sub>, electronic transport across the SWNT films become sensitive to H<sub>2</sub> if thin layers of certain metals, such as Pd, are present on the SWNT layer. A multi-layer H<sub>2</sub> sensor according to the invention comprises a carbon nanotube comprising layer, and a ultra-thin metal or metal alloy layer in contact with the nanotube layer. An electrical resistance of the layered sensor increases upon exposure to H<sub>2</sub>. The metal or metal alloy layer is preferably selected from the group consisting of Ni, Pd and Pt, or mixtures thereof. However, other metals or metal alloys that provide good sensitivity may also be used, including, but not limited to, Ti, Ag, and W. As defined herein, sensitivity is defined as the change in resistance of the layered sensor (AR) divided by the initial resistance prior to exposure to the H<sub>2</sub>-containing ambient (R). Sensors according to invention provide detection of ppm levels of hydrogen gas (H<sub>2</sub>) down to at least 10 ppm, and can be conveniently operated at room temperature.

[0020] In a preferred embodiment, the carbon nanotube comprising layer consists essentially of single wall nanotubes (SWNTs). SWNTs are preferred because the inner layers in multi-walled nanotubes (MWNTs) are protected by the outer layer and will not respond to hydrogen interaction with the outer layer. Thus, the initial R will be larger and the AR upon hydrogen exposure smaller upon exposure H<sub>2</sub> for MWNTs, and thus lower sensitivity as compared to SWNTs. Although the invention is described using the preferred SWNTs, MWNTs, or mixtures of SWNTs and MWNTs may also be used, although these embodiments will generally yield a reduced device sensitivity.

[0021] As noted above, the thickness of the ultra-thin layer corresponds to a thickness of from about 0.5 nm to about 10 nm and can be embodied as a layer having uniform thickness, or a sub-percolation layer comprising a plurality of metal islands, where some or all the metal islands can be connected by metal. The thinner the metal or metal alloy layer, the higher the resulting sensitivity of the sensor since the active sensing nanotube layer is shunted by the metal or metal alloy layer generally disposed thereon or disposed thereunder. As noted above, in the case where the metal islands are not electrically connected to form a low resistance electrical path from one end of the sensor to the other, the thickness of the metal islands can be on the order of hundreds of nms, or more, since such an arrangement will not shunt the carbon nanotube comprising active sensing layer. Moreover, if maximum sensitivity is not required, a thicker metal or metal alloy layer, such as 10 nm to 200 nm, or more, may be used with the invention.

[0022] Conductance or resistance of the coated SWNT layer sensor can be conveniently measured. In a preferred embodiment, conductance is measured by measuring the change in current between two electrodes which contact opposing sides of the metal-coated SWNT sensor upon exposure to H<sub>2</sub> to determine the presence of H<sub>2</sub>, and once calibrated, the concentration of H<sub>2</sub>.

[0023] An important advantage of the invention relates to reusability. Sensors according to the invention have been found to quickly recover their initial film conductance upon exposure to air or other ambient having little or no H<sub>2</sub>. For example, it has been found that most of the initial film conductance can be recovered in as little as 30 seconds in air.

[0024] Another attractive feature of sensors according to the invention is the low power consumption, which allows batteries to be used to provide power for sensor measurements. Power consumption can be on the order of 0.25 mW. This low power requirement is in part due to the lack of need for heating the sensor as must be done for catalytic bead and semiconducting oxide sensors. This power requirement could be reduced still further by pulsed operation. Moreover, sensors according to the invention have a simple structure, and can be measured using simple measurement arrangements as described below.

[0025] The interface between the SWNT layer and the nanoscale metal or metal alloy layer is preferably characteristic of an evaporated interface, or other low energy deposition process that does not significantly damage the nanotube layer. This finding was based on measurements that indicated that sputter deposition of metals onto the nanotubes may result in damage to the nanotube layer, while thermal evaporation of metals does not result in appreciable damage. Sputtered species generally have energies significantly higher than evaporated species, likely causing damage to the nanotube layer and potentially significant penetration depths.

[0026] Methods other than evaporation and sputtering may be used to deposit the ultra-thin metal or metal alloy layer, including, but not limited to, electrochemical or electroless deposition. For example, metal deposition could be performed electrochemically, utilizing the electrical conductivity of the nanotubes to act as the electrode upon which the electrodeposition takes place. Alternatively electroless deposition may also be employed with the nanotubes as the template upon which the deposition occurs.

[0027] A preferred method of forming thin (2 to 60 nm, such as 7 to 25 nm) SWNT films which have highly uniform thickness for use with the invention is described in commonly owned U.S. patent application Ser. No. 10/622,818 entitled "Transparent electrodes from single wall carbon nanotubes" filed on Jul. 18, 2003 ('818) and published on Oct. 7, 2004 as Published App. No. 20040197546. The transparent aspect of the nanotube films provided is generally not utilized in the present invention. However the high level of electrical interconnectedness of the nanotubes in the films generated using the process described in '818 which provides very high electrical conductivity, maximizes the sensitivity of sensors according to the invention to H<sub>2</sub> because nanotubes not electrically connected with other nanotubes do not contribute to the sensitivity of the device. The uniform SWNT film thickness provided using the process described in '818 moreover provides a uniformity of

metal association with the SWNT film, thereby maximizing the sensitivity of the device, defined as noted above as the change in resistance  $\Delta R$  (upon exposure to  $H_2$ ) divided by the initial resistance ( $R$ ) of the metallized SWNT film ( $\Delta R/R$ ).

[0028] Briefly, a dilute surfactant-suspension of SWNTs is vacuum filter onto a mixed cellulose ester (MCE) filtration membrane (0.1  $\mu m$  pore size, Millipore). The SWNTs are preferably purified pulsed-laser-vaporization grown SWNTs. However, SWNTs can be grown by any method. For example, moderately dense SWNTs can be grown on a surface as an inter-connected network as disclosed by Snow E S, Novak J P, Campbell P M, Park D. *Appl Phys Lett* 2003; 82:2145. The nanotubes deposit as a thin film on the membrane. Washing with purified water removes the surfactant. Once dried, the membrane with the SWNT film attached is cut to the desired size (e.g. 3 mm $\times$ 8 mm), wetted with pure water again, and the film side placed against the substrate (e.g. 600 nm thermal  $SiO_x/Si$  wafer) to which the SWNT film transfer is to be made. The substrate and membrane are sandwiched between wicking filter paper situated between metal plates and pressure is applied via spring clamps. Once the assembly is nearly dry (accelerated by oven heating at 95° C.) the film and membrane adhere sufficiently to the substrate to permit transfer to an acetone vapor bath. Acetone condensing onto the MCE membrane in the vapor bath dissolves it away, leaving only the SWNT film adhered to the substrate. These films are preferably subsequently baked in inert atmosphere at a fairly high temperature, such as 600° C., to desorb residual contaminants and charge transfer nanotube dopants.

[0029] FIG. 1 shows an exemplary  $H_2$  sensor 100 according to an embodiment of the invention built on a substrate 101. Substrate 100 which provides mechanical support for sensor 100 can be an electrically insulating material, or semiconducting or metal material. However, when a semiconducting or metal substrate is used, a dielectric layer such as  $SiO_2$  (not shown) will generally be disposed between the substrate and the active layers of sensor 100. Nanotube comprising layer 105 is disposed on substrate 100.

[0030] Sensor 100 includes contact electrodes 110 and 120 disposed on top of the nanotube comprising layer 105. Contact electrodes can be deposited using either sputtering or thermal evaporation. However, as noted above, evaporation is preferred. Nanotube comprising layer 105 is preferably a SWNT film having a highly uniform thickness from 7 to 25 nm as described in '818. However, the invention is not limited to SWNT layers described in '818.

[0031] Although the resulting arrangement is not shown in FIG. 1, contact electrodes 110 and 120 can be pre-deposited on the substrate 101 followed by deposition of the nanotube film comprising layer 105. The contact electrode thickness should be sufficiently thick to provide a low resistance contact, such as 500 Å of a metal. Between the contact electrodes 110 and 120 is the active sensor region 125 of sensor 100 which includes the nanotube comprising film 105. An ultra-thin layer 130 of Pd, Pt or Ni is disposed across active sensor region 125 so that the active sensor portion 125 is coated with the ultra-thin metal. In another embodiment of the invention, the surface of the entire sensor 100 is coated with the ultra-thin metal layer 130.

[0032] Although sensor devices described above are described as being macroscopic, such as sensor 100 shown

in FIG. 1, sensors according to the invention can be microscopic, such as disposed on chip along with associated electronics. For example, SWNT films can readily be patterned by standard lithographic techniques (see K. Lee, Z. Wu, Z. Chen, F. Ren, S. J. Pearton, A. G. Rinzler, *Nano Lett.* 4, 911 (2004)). This allows miniaturization and mass production which should result in hydrogen sensors according to the invention requiring still less power, as well as low cost as compared to macroscopic embodiments.

[0033] FIG. 2 shows an exemplary  $H_2$  microsensor 200 according to the invention disposed on chip, such as on a Si wafer 205 adapted for remote sensing. Signals from microsensor 100 are filtered by filter 210, then amplified by amplifier 215. The output of amplifier is fed to wireless transmitter 220 which drives antenna 225 which is shown as an on chip antenna 225. Filter 210, amplifier 215, wireless transmitter 220 and antenna 225 are all disposed on Si wafer 205. A battery pack (not shown) can be adhered to the back of the die for providing the energy needed to power the various components of microsensor 200.

[0034] In another related embodiment, integrated sensing systems according to the invention can be conveniently mounted in locations of interest, such as near  $H_2$  sources and associated  $H_2$  supply lines. Such systems provide continuous, automatic and real time (or near real-time) detection of  $H_2$  in the surrounding environment. The conductance measurements provided by sensor 200 are communicated to a processor (not shown). Processor can include associated non-volatile memory, such as for storing data manipulation algorithms, calibration data, or predetermined user programmable setpoints. Upon detection of more than a predetermined level of  $H_2$  indicating possible danger, the system can provide a visual display or an audible alarm (not shown).

[0035] Systems according to the invention can be positioned at several locations along a  $H_2$  supply line which provides fuel to an electrochemical generator, such as a PEM fuel cell. In a preferred embodiment, the system includes a valve which when closed turns off the supply of  $H_2$  to the electrochemical generator. Upon the detection of  $H_2$  above a predetermined level using sensors according to the invention, a sequence of events can be initiated to close the valve.

[0036] Although not shown, sensors according to the invention can be part of sensor arrays which detect not only  $H_2$ , but other species as well. The other sensors in the array can also be thin film sensors, electrochemical sensors, or other sensor types.

## EXAMPLES

[0037] The present invention is further illustrated by the following specific Examples, which should not be construed as limiting the scope or content of the invention in any way.

[0038] FIG. 3 shows a scanned image of the wired up  $H_2$  sensor used to acquire data presented in the Examples. The  $H_2$  sensor included two contacts, denoted as "source" and "drain", and an active sensor region denoted as "SW-CNT film". Experiments were performed with and without the ultra-thin metal or metal alloy layer disposed on the active sensor region as described below. The power supply used in the experiments performed is not shown in FIG. 3.

[0039] Sample exposure to gasses including  $H_2$  was performed at room temperature and atmospheric pressure in a

quartz flow tube with electrical feed-throughs for voltage and current leads. The gasses were fed via mass flow controllers to maintain a total flow of 450 sccm of either pure nitrogen, 500 ppm H<sub>2</sub> in N<sub>2</sub>, or a mixture of the two to obtain reduced concentrations of H<sub>2</sub>, or air. Electrical measurements were performed using an HP4156B source-meter. Excitation voltages ranged  $\pm 0.5$  V for I-V measurements and were held at 0.5 V for current-time measurements.

[0040] FIG. 4(a) show resistance as a function of time for sensors according to the invention using 25 nm thick SWNTs both with and without Pd coatings, respectively. Although the sensors including the Pd showed a significant response to 500 ppm H<sub>2</sub> in N<sub>2</sub>, the no Pd control did not show any detectable response. FIG. 4(b) shows the relative responses or sensitivities defined as the change in resistance divided by the initial resistance prior to H<sub>2</sub>-containing ambients ( $\Delta R/R$ ) after a 5 minute exposure to 500 ppm H<sub>2</sub> in N<sub>2</sub>, for the Pd coated sensor. The  $\Delta R/R$  was 6% at 100 ppm and 23% at 50 ppm as shown in FIG. 4(b).

[0041] Over the concentration range investigated, there was an essentially linear dependence of  $\Delta R/R$  on H<sub>2</sub> concentration, with a slope of about 0.04%/ppm of H<sub>2</sub>. The detection limit of the 25 nm films for measurement times of about 10 minutes following exposure for sensors according to the invention was found to be about 10 ppm H<sub>2</sub> at room temperature.

[0042] FIG. 5(a)-(b) shows the switching and recovery characteristics of H<sub>2</sub> sensing, as manifested in the change in  $\Delta R/R$  at fixed applied voltage (0.5V). During the first 15 minutes of testing, the sensors were exposed to 500 ppm H<sub>2</sub> in N<sub>2</sub>. After 15 minutes, the sensors were recovered in air. FIGS. 5(a) and 5(b) show  $\Delta R/R$  for sputtered 25 nm and 7 nm sensor films according to the invention, respectively. The fractional response ( $\Delta R/R$ ) of the 7 nm film is seen to be greater than that of the 25 nm film evidencing the improved sensitivity for thinner films.

[0043] FIG. 5(c) compares the exposure/recovery response of sputtered and thermally evaporated Pd layers on 7 nm SWNT films. As noted above, the recovery tests from H<sub>2</sub> exposure used air, which has been observed to result in a faster and more complete recovery. The thermally evaporated film is seen to have a substantially faster response in both exposure and recovery, although the overall signal is somewhat smaller than that for the sputter coated sample, which could be due to small differences in the thickness of the thin Pd layers in the respective cases.

[0044] It is to be understood that while the invention has been described in conjunction with the preferred specific embodiments thereof, that the foregoing description as well as the examples which follow are intended to illustrate and not limit the scope of the invention. Other aspects, advantages and modifications within the scope of the invention will be apparent to those skilled in the art to which the invention pertains.

We claim:

1. A multi-layer hydrogen sensor, comprising:  
a carbon nanotube comprising layer, and  
an ultra-thin metal or metal alloy layer disposed on said carbon nanotube comprising layer, wherein an electrical resistance of said layered sensor increases upon exposure to H<sub>2</sub>.

2. The sensor of claim 1, wherein said carbon nanotube comprising layer consists essentially of single wall nanotubes (SWNTs).

3. The sensor of claim 1, wherein said ultra-thin metal or metal alloy layer is selected from the group consisting of Ni, Pd, Pt, Ti, Ag, and W, or mixtures thereof.

4. The sensor of claim 1, wherein said ultra-thin metal or metal alloy layer comprises said Pd.

5. The sensor of claim 4, wherein a thickness of said carbon nanotube comprising layer is from 4 to 60 nm.

6. The sensor of claim 5, wherein said thickness of said carbon nanotube comprising layer is from 4 to 10 nm.

7. The sensor of claim 1, wherein said ultra-thin metal or metal alloy layer is from 10 to 50 angstroms thick.

8. The sensor of claim 1, wherein an interface between said carbon nanotube comprising layer and said ultra-thin metal or metal alloy layer is characteristic of an evaporated interface.

9. The sensor of claim 1, further comprising an integrated circuit substrate, wherein said sensor is disposed on said substrate.

10. The sensor of claim 9, further comprising at least one electronic device disposed on said substrate, said electronic device coupled to an output of said sensor.

11. A method of forming a layered hydrogen sensor, comprising the steps of:

providing a substrate;

forming an active sensor region on said substrate, said active sensor region comprising a carbon nanotube comprising layer disposed on or under an ultra-thin metal or metal alloy layer, and

forming contacts to said active sensor region on either side of said active sensor region.

12. The method of claim 11, wherein said ultra-thin metal or metal alloy layer is selected from the group consisting of Ni, Pd, Pt, Ti, Ag and W, or mixtures thereof.

13. The method of claim 11, wherein said ultra-thin metal or metal alloy layer comprises said Pd.

14. The method of claim 11, wherein a thickness of said carbon nanotube comprising layer is from 2 to 30 nm.

15. The method of claim 11, wherein said forming step comprises forming said carbon nanotube comprising layer on a porous support layer, placing said carbon nanotube comprising layer on said porous support layer on said substrate, and removing said support layer.

16. The method of claim 15, wherein said support layer comprises a porous membrane.

17. The method of claim 15, wherein said nanotube comprising layer on said support layer is formed using the steps of:

dispersing a plurality of nanotubes into a solution, said solution including at least one surface stabilizing agent for preventing said nanotubes from flocculating out of suspension;

applying said solution to said porous support, and

removing said solution, wherein said nanotubes are forced onto a surface of said porous support.

18. The method of claim 11, wherein said ultra-thin metal or metal alloy layer is formed using an evaporation process.

19. The method of claim 11, wherein said ultra-thin metal or metal alloy layer is from 10 to 50 angstroms thick.

\* \* \* \* \*

**University of South Carolina  
Scholar Commons**

---

Theses and Dissertations

---

2015

# Graphene Based Heterojunctions for Nano-Electronic and Sensing Applications

Md A. Uddin

*University of South Carolina - Columbia*

Follow this and additional works at: <https://scholarcommons.sc.edu/etd>

 Part of the [Electrical and Computer Engineering Commons](#)

---

## Recommended Citation

Uddin, M. A.(2015). *Graphene Based Heterojunctions for Nano-Electronic and Sensing Applications*. (Doctoral dissertation). Retrieved from <https://scholarcommons.sc.edu/etd/3137>

This Open Access Dissertation is brought to you by Scholar Commons. It has been accepted for inclusion in Theses and Dissertations by an authorized administrator of Scholar Commons. For more information, please contact [dillarda@mailbox.sc.edu](mailto:dillarda@mailbox.sc.edu).

**GRAPHENE BASED HETEROJUNCTIONS FOR NANO-ELECTRONIC AND SENSING  
APPLICATIONS**

by

Md Ahsan Uddin

Bachelor of Science  
University of Dhaka, 2009

Master of Science  
University of Dhaka, 2010

Master of Science  
University of Notre Dame, 2011

---

Submitted in Partial Fulfillment of the Requirements

For the Degree of Doctor of Philosophy in

Electrical Engineering

College of Engineering and Computing

University of South Carolina

2015

Accepted by:

Goutam Koley, Major Professor

Mohammad Ali, Committee Member

MVS Chandrashekhar, Committee Member

Thomas Vogt, Committee Member

Lacy Ford, Vice Provost and Dean of Graduate Studies

© Copyright by Md Ahsan Uddin, 2015  
All Rights Reserved.

## ACKNOWLEDGEMENTS

First, I would like to thank my advisor, Prof. Goutam Koley for endless support and patient guidance throughout my graduate study and research. Prof. Koley gave me the opportunity to conduct cutting-edge research in the area of graphene and related materials, always encouraged me to think and improvise new ideas and gave me freedom to pursue those. I have been extremely benefited from his training on scientific writing which would be helpful for my future career.

I thank and appreciate my PhD committee members, Prof. Ali, Dr. Chandrashekhar, and Prof. Vogt for their valuable suggestions and insightful questions for my research work. I am grateful to Prof. Ali and Prof. Vogt for taking the hassle and rearranging their schedule to accommodate my proposal defense within a very short notice.

I would like to express my gratitude to Prof. Sudarshan, who generously allowed me to use his clean room facility without which I would not be able to fabricate my devices. I would also like to thank Dr. Chandrashekhar for giving me his valuable time frequently to answer all the questions both related to research as well as for troubleshooting of various equipment in cleanroom. His suggestion about the impedance spectroscopy related study and allowing me to use the set-up is particularly important for chapter 5 of this dissertation. I am also grateful to Prof. Webb from Physics for allowing access to his lab facilities and for the collaboration on magneto-transport study described in chapter 6.

I would like to thank Dr. Voevodin at Air Force Research laboratory (AFRL), for providing the BN samples. Without the access of Raman spectroscopy set-up at Prof. Williams lab in Chemical Engineering, it would have been really difficult to carry out graphene related research. I would like to thank Dr. Ghoshroy and stuffs at electron microscopy center, for their help.

I would also like to express my gratitude to past and present members of Dr. Koley's lab, Dr. Chandra's lab, Dr. Sudarshan's lab, Dr. Webb's lab who have been always helpful to me throughout my graduate study and research. Particularly, I thank Amol for helping me out with various measurements and processing. Together we solved many problems. I really appreciate for the help of Bochen (Physics) regarding Hall measurement and Nick Glavin (AFRL) for BN samples. I am really grateful to the friends from Bangladeshi student community and faculty members at University of South Carolina, who made my stay at Columbia bearable. A big thanks also goes to staff at the department of Electrical Engineering specially Nat, Ashley, Alicia to help me out in administrative works.

Finally, I would like to express my gratitude to my family members, who have always been a source of encouragement and provided guidance throughout my life.

## ABSTRACT

Graphene, an atomically thin and semi-metallic two dimensional material, has been extensively researched over the past decade due to its superior intrinsic carrier velocity, electrical and chemically tunable work function, ability to form layered heterostructure with other materials, and relevant potential applications in electronics, sensing, optoelectronics, energy storage, etc. However, the confinement of charge carriers within one atomic layer results in an electrical transport that is extremely sensitive to the surrounding environment, which is beneficial for sensing applications, but at times unfavorable for electronic applications due to scattering from extrinsic impurities. In addition, due to its rather delicate structure, engineering a high quality gate dielectric without altering its characteristic electronic structure while enabling optimal surface passivation and gate control is one of the major challenges for graphene device development.

Hexagonal Boron Nitride (hBN) has emerged as a possible option to meet the challenges, and has been exploited to alter graphene electronic structure by intentional crystallographic misalignment between the layers at the time of transfer or synthesis. The variation in electronic structure by hBN is possible due to its unique properties such as inert surface, similar hexagonal and nearly lattice matched structure with graphene

and high surface optical phonon modes. Low temperature Pulsed laser deposition (PLD) grown amorphous BN on SiO<sub>2</sub>/Si, phase transformed to hBN by forming gas annealing, has been employed for graphene device application. Graphene field effect transistor (FET) fabricated from layered heterostructure of graphene/hBN on SiO<sub>2</sub>/Si exhibited electrical performance enhancement over graphene on SiO<sub>2</sub>/Si substrate in terms of mobility, carrier inhomogeneity and extrinsic doping.

In a parallel effort, taking advantage of graphene's tunable work function, a novel genre of sensor based on noble metal nanoparticle functionalized graphene/Si heterojunction Schottky diode has been developed for sensing non-polar H<sub>2</sub>, and enhancing response for polar NH<sub>3</sub> molecular species. Reverse bias operation of the diode sensor exhibited orders of magnitude higher response compared to graphene FET based sensors due to exponential change in reverse current originated from interface barrier height change. The reverse bias operation also allows low power operation and modulation of the Fermi level of graphene, which can lead to the tuning of sensitivity and expansion of the dynamic range. Impedance Spectroscopic analysis of the diode sensor has been carried out to understand the underlying current transport mechanism. Fitting the impedance spectra for different gaseous exposure conditions with an equivalent circuit model, the changes in junction resistance and capacitance have been extracted. Along with these two parameters, experimentally obtained 3-dB cut off frequency for each gas exposure has been utilized for multimodal sensing by the diode sensor.

Finally, temperature dependent magneto-transport study of PdH<sub>x</sub> passivated graphene has been carried out to elucidate the effect of metal nanoparticle assisted doping and molecular adsorption on graphene electrical transport properties. It has been observed

from the systematic study that, the dominant scattering mechanism in bilayer graphene switched from coulomb scattering to thermal excited surface optical phonon scattering after  $\text{PdH}_x$  passivation, and Hall mobility exhibited significant enhancement at the measurement temperature range of 298 to 10 K. Due to recent interests in exploiting metallic nanoparticles as dopant for 2D crystals, as well as enhancing sensitivity of chemical sensors and photodetectors, the findings are significant and would pave the way for future research efforts in this area.

## TABLE OF CONTENTS

ACKNOWLEDGEMENTS.....	iii
ABSTRACT .....	v
LIST OF FIGURES .....	x
<b>CHAPTER 1: INTRODUCTION.....</b>	<b>1</b>
1.1 ELECTRONIC STRUCTURE OF GRAPHENE .....	3
1.2 ELECTRONIC TRANSPORT AND FIELD EFFECT BEHAVIOR OF GRAPHENE.....	6
1.3 PRESENT STATUS, OPPORTUNITIES AND CHALLENGES .....	8
1.4 OUTLINE OF THE DISSERTATION .....	13
<b>CHAPTER 2: GRAPHENE GROWTH, AND ELECTRICAL CHARACTERIZATION .....</b>	<b>16</b>
2.1 CHEMICAL VAPOR DEPOSITION GROWTH OF GRAPHENE .....	17
2.2 STRUCTURAL AND MATERIAL CHARACTERIZATION OF GRAPHENE .....	20
2.3 GRAPHENE TRANSFER.....	23
2.4 GRAPHENE FET AND ELECTRICAL TEST PATTERN FABRICATION .....	26
2.5 ELECTRICAL CHARACTERIZATION OF GRAPHENE DEVICES .....	27
<b>CHAPTER 3: ENHANCED GRAPHENE ELECTRICAL TRANSPORT PROPERTIES ON PLD GROWN BN ON SILICON DIOXIDE/SILICON SUBSTRATE .....</b>	<b>32</b>
3.1 INTRODUCTION .....	32
3.2 SYNTHESIS OF BORON NITRIDE BY PULSED LASER DEPOSITED .....	35
3.3 BORON NITRIDE MATERIAL CHARACTERIZATION .....	38

3.4 GRAPHENE FET FABRICATION ON PLD BORON NITRIDE .....	41
3.5 GRAPHENE ON BN ELECTRICAL CHARACTERIZATION.....	43
<b>CHAPTER 4: FUNCTIONALIZED GRAPHENE/SILICON CHEMI-DIODE H<sub>2</sub> SENSOR WITH TUNABLE SENSITIVITY .....</b>	<b>54</b>
4.1 INTRODUCTION .....	54
4.2 FABRICATION AND CHARACTERIZATION OF GRAPHENE/SI SCHOTTKY DIODE ....	56
4.3 SENSING RESPONSE .....	61
<b>CHAPTER 5: IMPEDANCE SPECTROSCOPIC ANALYSIS OF FUNCTIONALIZED GRAPHENE/P-SILICON SCHOTTKY DIODE FOR SENSING APPLICATION.....</b>	<b>75</b>
5.1 INTRODUCTION.....	75
5.2 SENSITIVITY ENHANCEMENT BY METAL NANO-PARTICLE FUNCTIONALIZATION..	77
5.3 IMPEDANCE SPECTROSCOPY OF GRAPHENE/SI DIODE SENSOR FOR MULTIMODAL SENSING.....	82
5.4 ANALYSIS OF DIODE SENSOR IMPEDANCE SPECTRA BY FITTING EQUIVALENT CIRCUIT MODEL.....	87
<b>CHAPTER 6: EFFECT OF METAL HYDRIDE SURFACE FUNCTIONALIZATION ON GRAPHENE: A HALL MEASUREMENT STUDY.....</b>	<b>95</b>
1.1 INTRODUCTION .....	95
1.2 HALL EFFECT .....	96
1.3 FABRICATION OF HALL BAR AND MEASUREMENT SET-UP .....	99
1.4 RESULTS AND DISCUSSION .....	101
<b>CHAPTER 7: CONCLUSIONS AND FUTURE DIRECTIONS .....</b>	<b>118</b>
REFERENCES .....	122

# CHAPTER 4

## FUNCTIONALIZED GRAPHENE/SILICON CHEMI-DIODE H<sub>2</sub> SENSOR WITH TUNABLE SENSITIVITY

### 4.1. Introduction

Due to its two-dimensional (2D) nature that makes it essentially a surface, and very high carrier mobility [1-6], graphene is especially suited for sensing applications [3-10]. Although it has excellent sensitivity to a large variety of polar molecules, (i.e. NO<sub>2</sub> and NH<sub>3</sub>) it is insensitive to most non-polar molecules, such as H<sub>2</sub>, with which it does not exchange charge. A surface functionalization is therefore necessary for detecting these non-polar molecules. It has been demonstrated that surface functionalization of graphene by catalytically active noble metals (such as Pd and Pt) leads to charge transfer between graphene and the metal hydride formed in presence of H<sub>2</sub> facilitating its detection [11–13]. There are reports on H<sub>2</sub> sensors utilizing epitaxial graphene [12], graphene synthesized through chemical vapor deposition (CVD) [11], and chemically synthesized graphene nanoribbon networks [13], which are functionalized with either Pd or Pt to impart H<sub>2</sub> sensitivity. Of these, only the chemically synthesized graphene nanoribbon network based sensor has so far shown good H<sub>2</sub> sensitivity (producing ~55% change in resistance for 40 ppm H<sub>2</sub>), while others showed much lower sensitivity in the range of few percent for tens

of ppm H<sub>2</sub> exposure. The higher sensitivity of the graphene nanoribbon networks [13] can be attributed to its porous structure and high specific surface area. In general, the sensitivity of these commonly used “chemiresistor” type sensors is dependent on two factors: (i) the amount of charge exchanged from the analytes (facilitated by the functionalization layer), and (ii) the mobility of the charge carriers, since resistivity is inversely proportional to the product of mobility and charge density. The former depends on the material properties and thickness of the functionalization layer used, while the latter is controlled by the graphene quality, and more significantly, by the charge carrier scattering caused by the functionalization layer [14, 15] and substrate underneath the graphene [16]. Although the material property of graphene can be controlled to a large extent through optimization of the synthesis process, in general, the choices are very limited in terms of the substrate and the functionalization layer used to realize the sensors. However, the effects of the last two factors are extremely significant on graphene mobility, which reduces from 200,000 cm<sup>2</sup>/Vs for suspended graphene [2] to only a few thousand cm<sup>2</sup>/Vs for graphene on SiO<sub>2</sub> or SiC substrates [16, 17]. The functionalization layer can further reduce the mobility [18], and if conducting, can also provide a parallel path for current flow thereby further reducing sensitivity. Therefore, sensing paradigms where the sensitivity of the sensor does not directly depend on the mobility of the charge carriers would be of significant interest.

Recent demonstration of graphene/Si Schottky heterojunction [19], and its usage in several devices from solar cells to “barrisitors” [20-22] have opened up the possibility for developing a new class of “chemi-diode” sensors. Due to the atomically thin and semimetallic nature of graphene, its Fermi level can be easily modulated by electrical, optical or chemical means which in-turn changes the Schottky barrier height (SBH) at the

heterointerface. This is in contrast to classical metal-semiconductor Schottky junctions, where the Fermi level of the metal remains fixed regardless of external factors. Nevertheless, this property of graphene/Si heterojunctions can be utilized to design sensors with ultra-high sensitivity, since change in SBH induced by adsorbates exchanging charge with graphene, will change the current flowing across the junction exponentially. Graphene/Si Schottky diode based sensor has been demonstrated recently in large forward bias operation, where the diode current is controlled by series resistance, hence, high sensitivity was not observed [23]. In this work, we have demonstrated for the first time, catalytically active noble metal functionalized Graphene/Si Schottky diode H<sub>2</sub> sensor operated in reverse bias, which takes advantage of the exponential change in current due to SBH change, and exhibits several times higher sensitivity compared to the best performance of graphene based chemiresistor type H<sub>2</sub> sensor functionalized similarly. In fact, the sensitivity of the sensor allows us to reach a detection limit close to the atmospheric concentration of H<sub>2</sub> (~0.6 ppm) [24]. The reverse bias operation also allows modulation of the Fermi level of graphene depending on the magnitude of the bias, which can lead to the tuning of sensitivity of the sensor and expansion of the dynamic range. Another advantage of the reverse bias operation of the sensor is its low power requirement due to low steady state current in the range of μA flowing in reverse bias.

## **4.2. Fabrication and Characterization of Graphene/Si Schottky Diode**

In this work, both Pd and Pt-functionalized graphene/p-Si Schottky diodes were investigated in terms of their sensing behavior toward H<sub>2</sub>. Graphene samples were synthesized through chemical vapor deposition (CVD) on Cu (catalyst) foils (Alfa Aesar, 99.999% purity) in a quartz tube furnace. The synthesis was performed at 1035 °C and 10

Torr pressure with CH<sub>4</sub> as the precursor (nominal flow rate of 40 sccm) along with H<sub>2</sub> (nominal flow rate 50 sccm), following earlier reports [25, 26]. Graphene on copper foil was lithographically patterned and strips were defined by O<sub>2</sub> plasma etch. The Cu foil with graphene strips was coated with two layers of poly methyl methacrylate (PMMA), to add mechanical strength during subsequent processing, and baked for 1 min at 150 °C. Next, the graphene layer on the back side of the sample was removed by oxygen plasma etching, which was followed by Cu etching in 0.5 M ammonium persulfate solution for more than 12 hour, releasing the graphene/PMMA bi-layer [16]. SiO<sub>2</sub> (100 nm) on p-Si has been selectively removed by 1:5 diluted buffered HF just prior to transfer of graphene. Ti/Au was deposited selectively on top side of Si and annealed in Ar/H<sub>2</sub> atmosphere at 400 °C to form ohmic contacts. After rinsing in deionized water and IPA, the graphene/PMMA bi-layer was scooped and placed on the patterned SiO<sub>2</sub>/Si substrate. It was then baked at 220 °C for 5 minutes to reflow the PMMA resulting in more uniformity and less cracking in transferred graphene. Afterwards, the sample was placed in acetone for 2 hour to remove PMMA [16, 27]. Ti (20 nm)/Au (80 nm) contacts were evaporated on graphene transferred on SiO<sub>2</sub>/Si using shadow mask. The p-Si used in this work is lightly doped and have resistivity in the range of 1-10 Ω-cm. The device length is 200 μm and width is ~1000 μm in all the cases where ~80% of the total area is functionalized. There is an additional 200 μm Graphene on SiO<sub>2</sub> between the metal contact and Graphene/Si interface. Different thickness (1-3 nm) of Pd and Pt were evaporated on graphene in e-beam metal deposition chamber.

Raman spectra were measured on graphene transferred to the Si substrate to determine the quality of transferred graphene. Figure 4.1 (a), (b), and (c) show the

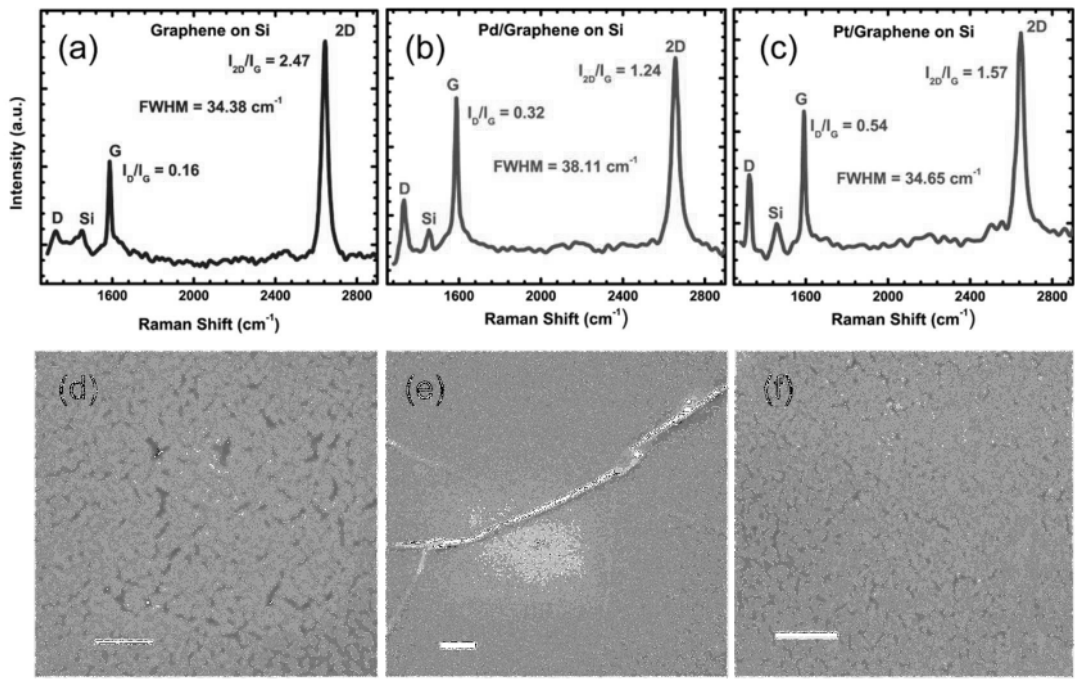


**Figure 4.1** Raman spectra of (a) Graphene on p-Si, (b) Pd-deposited graphene on p-Si, (c) Pt-deposited graphene on p-Si; (d) SEM top view image of 3 nm Pd-functionalized graphene on p-Si. Scale Bar is 50 nm. (e) Zoomed out image of that shown in (d) showing graphene wrinkles. Scale Bar is 100 nm. (f) Pt-functionalized graphene on p-Si. Scale Bar is 100 nm.

representative Raman spectra of graphene transferred on Si as well as Pd and Pt decorated graphene on Si. All signature peaks, D, G and 2D, along with the Si peak at  $1451 \text{ cm}^{-1}$ , can be observed. The transferred graphene layer on top of Si [Figure 4.1(a)] shows intensity ratio,  $I_D/I_G$  ratio of 0.16, suggesting high quality graphene [28]. The  $I_{2D}/I_G$  ratio of 2.47, and 2D peak full width at half maximum of  $34.38 \text{ cm}^{-1}$ , are indicative of single layer graphene [29]. The  $I_D/I_G$  ratio of 0.32 for Pd decorated graphene [Figure 4.1(b)] suggests some degradation in the quality of graphene following electron beam evaporation of 3 nm thick Pd nanoparticles for functionalization. This degradation might be due to the creation of point defects in graphene by the metal atoms hitting it during e-beam evaporation. For 2 nm thick Pt functionalized graphene the  $I_D/I_G$  ratio is higher, 0.54 [Figure 4.1(c)], which

indicates higher defect density in the film. It is probably a consequence of higher film damage caused by heavier Pt atoms during evaporation process compared to Pd atoms. Deposited metal films typically grow on crystalline substrates through nucleation followed by grain growth. The growing grains coarsen and coalesce to form complete film coverage as metal evaporation continues. Figure 4.1(d) captures the initially formed grains of Pd on graphene/Si in a scanning electron microscopy (SEM) micrograph. Due to the small growth duration, (~2 minutes for 3 nm thickness) the Pd grains could not become large enough to coalesce completely, therefore partial coverage of Pd film is observed. A zoomed out SEM micrograph [Figure 1(e)] at the same location shows an overall smooth coverage with a few wrinkles in the graphene layer. Figure 4.1(f) shows an SEM micrograph depicting similar coverage for deposited Pt film with 2 nm thickness.

Figure 4.2(a) shows the schematic of a graphene chemiresistor sensor fabricated side by side with a graphene/Si heterojunction chemi-diode sensor with metal film functionalization layer. Optical microscopy image of the fabricated Pd-functionalized graphene/Si Schottky diode sensor is shown in Figure 4.2(b). The initial electrical characteristic of chemi-diode before Pd and Pt deposition is shown by the solid black curves in Figure 4.2(c) and Figure 4.2(d), respectively, which exhibits typical rectifying characteristic in agreement with previous reports [19-23]. A Schottky type response is expected since the work function of graphene is around 4.5 eV, which is lower than that of p-Si, with an estimated work function of ~4.97 eV (electron affinity and bandgap of Si are

4.05 and 1.12 eV, respectively [30], and from resistivity of  $1 - 10 \Omega\text{cm}$  for the p-type Si,

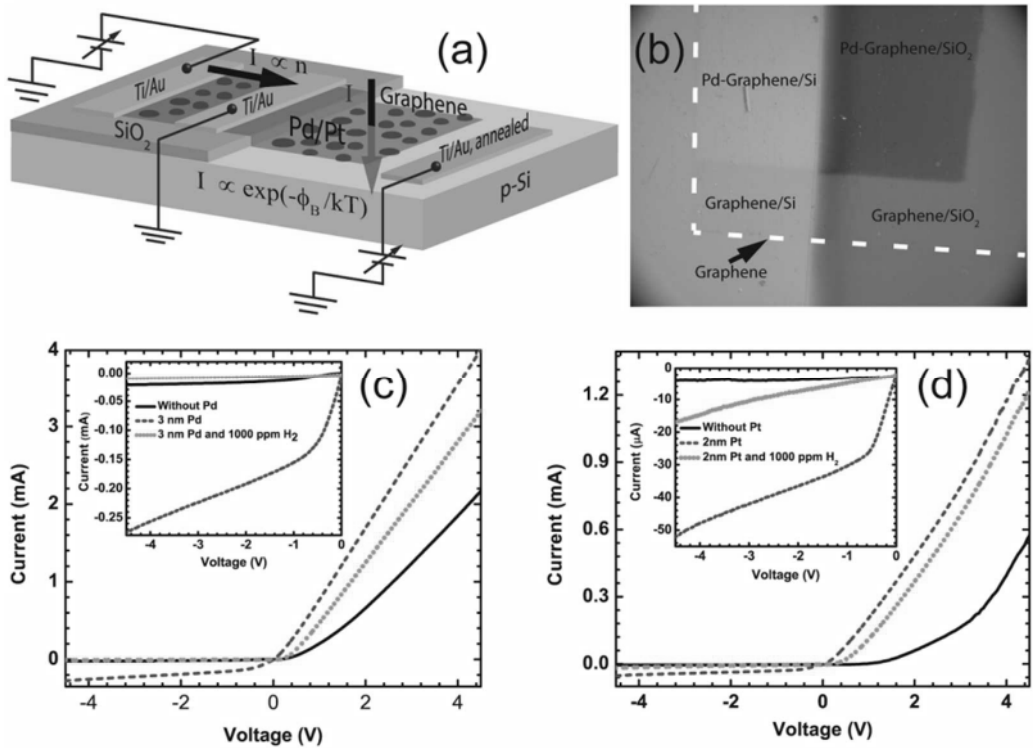


**Figure 4.2** (a) Device schematic and biasing scheme of Pt/Pd functionalized graphene chemiresistor and graphene/Si Schottky diode sensors fabricated on the same chip. Gray spots indicate metal decoration. (b) Optical Image of graphene/p-Si heterojunction Schottky diode sensor with H<sub>2</sub> nm Pd-functionalization, white dashed box approximately enclosed the graphene on both Si and SiO<sub>2</sub>, graphene is visible on SiO<sub>2</sub>, and Pd-functionalization is also showing contrast on SiO<sub>2</sub> region covered by graphene. (c) Current-Voltage (I-V) characteristics of graphene/p-Si (black solid line), after Pd-functionalization (blue dashed line), and after 10 minutes exposure of the Pd-functionalized sensor to 1000 ppm H<sub>2</sub> (orange dotted line). (d) I-V characteristics of graphene/p-Si (black solid line), after Pt-functionalization (blue dashed line) and after 10 minutes exposure of the Pt-functionalized sensor to 1000 ppm H<sub>2</sub> (orange dotted line). The rectifying current-voltage characteristics of  $E_F - E_V$  is estimated to be  $\sim 0.2$  eV). The rectifying current-voltage characteristics of

graphene/Si heterojunction can be expressed using thermionic emission model formulated by the following equation [30],

$$I = I_S \left[ e^{\left( \frac{qV}{\eta kT} \right)} - 1 \right] = A A^* T^2 e^{-\frac{q\phi_B}{kT}} \left[ e^{\left( \frac{qV}{\eta kT} \right)} - 1 \right] \quad (4.1)$$

Here,  $I_S$  is the reverse saturation current,  $q$  is the electronic charge,  $A$  is the contact area,  $A^*$  is the effective Richardson Constant,  $\eta$  is the diode ideality factor,  $T$  is the temperature,  $\phi_B$  is the SBH, and  $k$  is the Boltzmann constant. The contact area for the junction is 0.2117 mm<sup>2</sup> (obtained from SEM image) and  $A^*$  for p-Si is 46.32 Acm<sup>-2</sup>K<sup>-2</sup> [31]. From Figure 4.2(c), the extrapolated ideality factor and SBH using the thermionic emission model are 1.68 and 0.648 eV, respectively, which are quite close to those reported in the literature [20].

The higher ideality factor has been attributed to various factors including SBH variation with reverse bias arising from graphene's bias dependent work function, Schottky Barrier inhomogeneity and image charge induced SBH lowering [32-34]. Due to graphene's bias dependent work function, with the increase in reverse bias magnitude the SBH at graphene/Si interface decreases and correspondingly the reverse current increases, and is noticeable from the inset of Figure 4.2(c).

### 4.3. Sensing Response

After separate deposition of 3 nm Pd and 2 nm Pt over the graphene/Si heterojunction on two different devices, both forward and reverse currents were found to increase, however, the I-V characteristics still remained distinctly Schottky (dashed blue curve in Figure 4.2(c) and (d)). The increase in current is due to the reduction in graphene/Si barrier height caused by “p-type doping” of the deposited Pd/Pt layer. Such doping of graphene by metallic thin

films resulting in significant movement of the Dirac point, to both right and left (depending on the work function of the deposited metal compared to that of graphene), has been reported earlier [35]. Since the work function of Pd and Pt [36] is much higher than graphene (4.5 eV), electrons from graphene are expected to move to Pd/Pt, effectively inducing p-type doping in graphene, and causing downward movement of its Fermi level. This effect has been both theoretically predicted [37] and experimentally observed for Pt-functionalized graphene [12]. The downward movement of graphene Fermi level would then reduce the hole barrier height at the graphene/Si interface, which was experimentally observed as the SBH changed from 0.648 to 0.546 eV after the 3 nm Pd deposition and 0.643 to 0.592 eV after 2 nm Pt deposition. To investigate the effect of H<sub>2</sub> exposure, the I-V characteristic was retaken after 10 minutes of 1000 ppm H<sub>2</sub> flow as shown by the orange dotted curve in Figure 4.2(c) and (d). From Figure 4.2(c), we find that both forward and reverse currents decreased in magnitude with H<sub>2</sub> exposure, which is expected since the SBH increased from 0.546 to 0.59 eV in case of Pd functionalized device. The SBH increase can be explained by the following mechanism: In presence of Pd or Pt, H<sub>2</sub> dissociates into atomic hydrogen and forms metal hydrides (PdH<sub>x</sub>, PtH), which have lower work function than the pure Pd and Pt, respectively [11-13]. This results in electron transfer to graphene reducing its p-doping, and increasing hole barrier height at the graphene/Si interface. However, the percentage change in forward current is much smaller than the reverse current, i.e. at 4V forward bias, the current decreased from 3.56 to 2.81 mA (21.06% change) while at -4 V bias it changed from -256.65 to -9.42 μA (96.33%). We have extracted the series resistance from the diode forward characteristics (following the similar methods employed in reference 20), and found it to change from 1.05 (pre-

exposure) to  $1.32\text{ k}\Omega$ , after exposure to 1000 ppm  $\text{H}_2$ , for Pd functionalization. In terms of resistance change, a commonly used metric for  $\text{H}_2$  sensing [11-13], the changes at 4 V forward and reverse bias are  $\sim 1.26$  and  $\sim 27$  times, respectively. Clearly, the sensitivity (defined as the ratio of change in resistance due to  $\text{H}_2$  exposure to the initial resistance before exposure, expressed as a percentage) is dramatically enhanced in reverse bias. In addition, the power consumed is much reduced in reverse bias, only 1.03 mW, compared to 14.24 mW in forward bias, which is  $\sim 14$  times higher. Reverse bias operating power can be further reduced to  $\mu\text{W}$  range simply by scaling down the device dimensions. However, the device dimensions should be carefully chosen to keep signal to noise ratio (SNR) acceptable since SNR degrades as the device is scaled down. A similar response is also observed for Pt functionalization, and shown in Figure 4.2(d), the SBH changed from 0.592 to 0.623 eV with the exposure of 1000 ppm  $\text{H}_2$  and at -4 V bias, current decreased from -47.8 to -14.94  $\mu\text{A}$  (68.74% change) which is higher than the response obtained at 4 V forward bias, 1.168 to 1.1017 mA (5.68% change). The series resistance increased from 3.11 to  $3.44\text{ k}\Omega$  after exposure to 1000 ppm  $\text{H}_2$ .

Noble metal nanoparticle functionalization induced doping in graphene, resulting decrease in the heterojunction interface Schottky barrier height and subsequent increase after  $\text{H}_2$  exposure is also confirmed by capacitance-voltage (C-V) measurement which is discussed at the end of this chapter.

To directly compare the performances of Graphene/Si chemi-diode and graphene chemiresistor, they were fabricated side by side on the same chip (schematically shown in Figure 4.2(a)) using the same graphene sample and functionalized by 3 nm Pd and 2 nm Pt, separately. Performances of both chemi-diode and chemiresistor sensors with 3 nm Pd

functionalization upon exposure to 200 ppm H<sub>2</sub> for 10 minutes, at -5V bias are shown together in Figure 4.3(a). Graphene/Si diode sensor shows 122% resistance change (red curve), while the response for graphene chemiresistor is a mere 2.9% (blue curve). Thus, more than 40 times performance enhancement for the same exposure and bias conditions are observed for the chemi-diode sensor compared to the chemiresistor sensor. Of course,

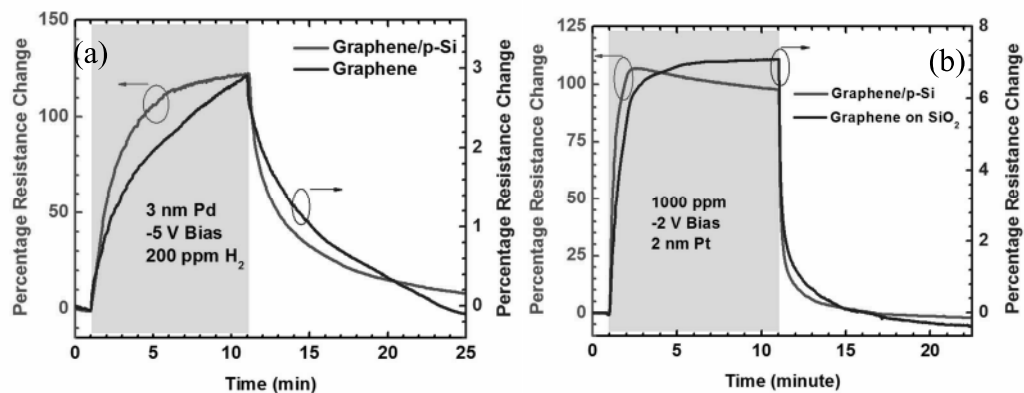


**Figure 4.3** (a) Comparison between the H<sub>2</sub> responses for similarly functionalized graphene/p-Si chemi-diode device and graphene chemiresistor on SiO<sub>2</sub>, fabricated on the same chip. (a) Response for 200 ppm H<sub>2</sub> (pink box) in case of Pd- functionalization where red one (left y-axis) is for graphene/p-Si chemi-diode and blue one (right y-axis) is for graphene chemiresistor. (b) Response for 1000 ppm H<sub>2</sub> (pink box) when Pt- functionalization was employed where red curve (left y-axis) is for graphene/p-Si chemi-diode and blue curve (right y-axis) is for graphene chemiresistor.

the operating power for chemiresistor is 46.425 mW, which is much higher than 64.7  $\mu$ W for the diode sensor. The performance enhancement of the graphene/Si diode sensor was verified with 2 nm Pt decoration as well. The responses are shown in Figure 4.3(b) for 10 minutes of 1000 ppm H<sub>2</sub> exposure at -2V bias condition. Once again the diode sensor

showed a much higher sensitivity of 106% compared to only 7% for the chemiresistor, a 15 fold improvement.

We would like to point out here that the performance of our graphene/Si chem-diode sensor is at least an order of magnitude improved over other graphene based H<sub>2</sub> sensors reported utilizing the same Pd functionalization [11, 38]. The performance is also better compared to the high-sensitivity graphene nano-ribbon based sensor [13], which owes its high sensitivity to the porous nature and large surface area of the nanoribbons. The very high sensitivity of our sensors can be attributed to the usage of a Schottky junction to perform sensing, where the current changes exponentially with the change in SBH induced by H<sub>2</sub> adsorption. The Schottky diode type H<sub>2</sub> sensor based on Pd/semiconductor (i.e. Pd/Si [39] and Pd/InP [40]) junction has been reported earlier, utilizing various methods for depositing Pd contacts and resulting in high H<sub>2</sub> sensitivity. It should, however, be kept in mind that the role of the Pd layer in our sensor is that of a functionalization layer, i.e. it is not directly forming a Schottky contact with the Si, it is just allowing graphene/Si junction to respond to H<sub>2</sub> by facilitating its adsorption and changing the SBH. In addition, the Fermi level of the graphene layer may be altered using the reverse bias to tune the hydrogen sensitivity, a feature that is completely unique to this sensing paradigm as compared to metal/semiconductor Schottky diode where modulation of SBH by inducing strain in a piezoelectric semiconductor, such as ZnO, have shown improvements in tactile [41] and O<sub>2</sub> [42] sensitivity.

The response of Pt (2 nm) functionalized sensor was investigated for H<sub>2</sub> concentration varying from 1000 to 10 ppm at a fixed reverse bias of -4V. The sensing response illustrated in Figure 4.4(a) can be seen to vary from 103 to 5.5% as the H<sub>2</sub>

concentration changes from 1000 to 10 ppm, for 15 minutes exposure. As mentioned earlier, an advantage of the sensor operation in reverse bias is that the bias magnitude can be varied to change the Fermi level of graphene and consequently tune the sensor response. With the higher reverse bias applied to the graphene/Si diode, the graphene Fermi level moves further down [33, 43], compared to the donor states induced by the metal hydride and the graphene/Si SBH will decrease. Thus, in presence of H<sub>2</sub>, more electrons would transfer to graphene, which will in turn change the SBH by a larger amount, and the sensitivity can be expected to be higher. To verify this concept, negative voltage biases varying from -1 to -5 V were applied to the p-Si (with 1 nm Pt and Pd functionalization layers), and the sensor responses upon exposure to 1000 ppm H<sub>2</sub> were recorded. Here, the statistical errors were within ~ 10% of the mean values of sensitivity plotted in the graph. For the 1 nm Pt deposited device the response varied from 27.5 to 77.5% for the aforementioned voltage range, with higher rise rate observed for the larger reverse bias voltages, which also resulted in higher peak response (Figure 4.4(b)). To further substantiate the idea, the responses of the 2 nm Pt functionalized device (which are shown in Figure 4.4(a) for -4 V bias) were retaken at -8V bias, and shown in Figure 4.4(c). The percentage resistance change increased from 5.5% at -4V to 13% at -8V for 10 ppm H<sub>2</sub> exposure over the same 10 minute duration. In fact, this also enabled detection of H<sub>2</sub> down to 1 ppm level, which is significant, as it is close to the atmospheric background of 0.6 ppm [24].

Since, our sensing experiments were conducted in atmospheric conditions, strictly speaking the sensor response for 1 ppm H<sub>2</sub> exposure actually corresponds to ~0.4 ppm of H<sub>2</sub> concentration. Utilizing an optimized Pd coating the sensor sensitivity was significantly

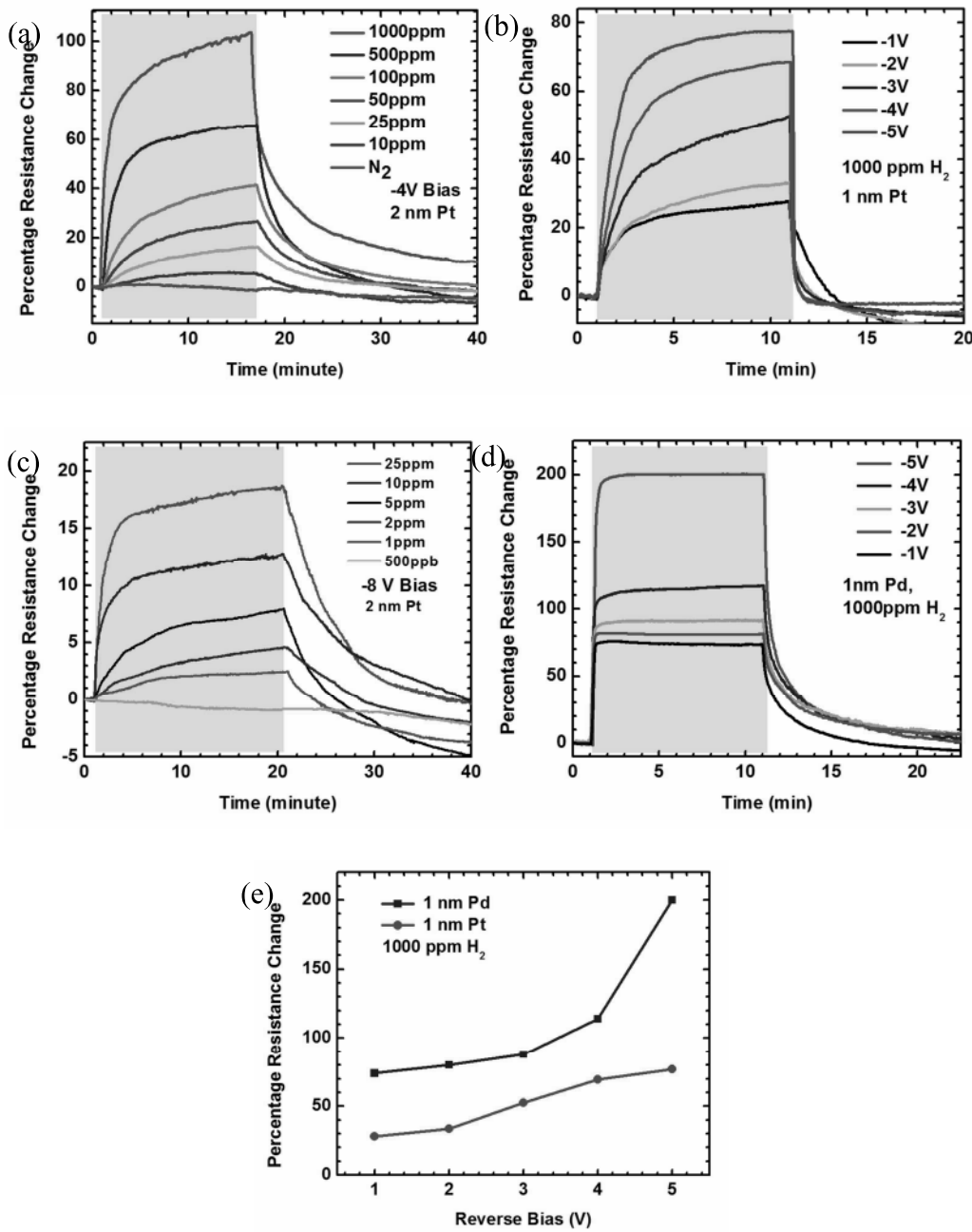


**Figure 4.4** (a) Percentage resistance change of Pt-deposited graphene/p-Si device at -4 V bias for different  $\text{H}_2$  concentration in the range of 1000-10 ppm and in  $\text{N}_2$  environment (pink box). (b) Bias dependence of sensor response for 1000 ppm  $\text{H}_2$  (pink box) as the voltage was changed from -1 to -5 V for Pt-functionalized device. (c) Sensitivity enhancement at higher bias (-8V) for the same device with response shown in part (a) for applied bias of -4V. (d) Bias dependence of sensor response for 1000 ppm  $\text{H}_2$  (pink box) as the voltage was changed from -1 to -5 V for Pd-functionalized device. (e) Comparison between the responses for Pt and Pd-functionalized sensor at

enhanced (explained later), which highlights the possibility of performing detection of H<sub>2</sub> in the ppb level in a controlled environment. These results clearly indicate that the sensitivity of the graphene/Si chemi-diode sensor is significantly tunable with magnitude of reverse bias, which is not possible with typical metal/semiconductor diode sensors.

Since Pd has a 3 times higher H<sub>2</sub> solubility compared to Pt (while having same H<sub>2</sub> diffusion coefficient) [44], it causes a larger reduction in p-type doping upon H<sub>2</sub> adsorption, which can result in a larger increase in SBH, hence Pd functionalized graphene/Si chemi-diode sensors are expected to show better response than Pt functionalized ones. Indeed for the 1 nm Pd functionalized device the response varied from 200% at -5V to 74% at -1 V (Figure 4.4(d)), which is ~2.5 times higher compared to 1 nm Pt functionalized sensor for the same applied bias (Figure 4.4(b)). Additionally, there are significant differences between the Pt and Pd coated devices in terms of the transient responses. For the former, the response time is much slower than the later, while the recovery time is somewhat faster. This is however expected due to higher H<sub>2</sub> solubility in Pd, which leads to higher concentration in the Pd functionalization layer, which would make the response time faster but the recovery time a little slower. The sensitivity for Pt and Pd functionalized (1 nm thick metal coating) devices are compared in Figure 4.4(e) for various reverse bias voltages from where it is apparent that the later always show better sensitivity to H<sub>2</sub> irrespective of the voltage bias. Interestingly, with increasing reverse bias, the sensitivity of the Pd-coated sensor keeps increasing sharply, while that of the Pt-coated sensor displays a saturating trend.

Defining the response time as the time elapsed to attain 50% of the maximum resistance change, we find that for Pt-functionalization (Figure 4.4(a)), the response time

increases from 38 to 180 sec as the H<sub>2</sub> concentration decreases from 1000 ppm to 25 ppm. This definition of response time deviates from the traditional definition (which considers the time elapsed between 10% and 90% of the maximum value), but is more practical for sensor design since it is proportional to the rise rate, and has been used earlier.[13] The observed variation in response time with concentration is consistent with earlier observations for graphene nanoribbon network based sensor [13], and is actually expected since under lower concentration additional time is needed for same number of H<sub>2</sub> molecules to get adsorbed. Using similar definitions, the recovery time is found to increase from 84 sec for 1000 ppm to 160 sec for 25 ppm H<sub>2</sub>. Careful consideration of Figure 4.4(b) and (d) indicates that the response and recovery time generally improves at higher negative biases. For the Pt-functionalized device and 1000 ppm H<sub>2</sub> exposure, the response and recovery times are both ~44 sec for 1 V reverse bias, which reduces to 42 sec and 4 sec, respectively, for 5 V reverse bias. The response times for the Pd functionalized device for 1000 ppm H<sub>2</sub> exposure are much lower at 6 sec for 1 V reverse bias which however remains almost the same for 5 V reverse bias. The recovery times are 34 sec and 18 sec for 1 and 5 V reverse bias, respectively.

Thicker Pd layer is expected to improve the H<sub>2</sub> sensitivity in two ways. First, it would lower the graphene Fermi level by a larger magnitude due to higher p-type doping, which would improve sensitivity as discussed below. Second, it would adsorb higher volume of H<sub>2</sub>, and cause higher movement of the graphene Fermi level, thereby resulting in higher sensitivity. In fact, a previous study on graphene chemiresistor based H<sub>2</sub> sensor [38] indicate that 3 nm Pd functionalization layer provides maximum sensitivity to H<sub>2</sub>. From the I-V characteristics, we find that higher Pd thickness of 3 nm changes the

graphene/Si SBH by 102 meV compared to 61 meV caused by 1 nm Pd deposition. This means the graphene Fermi level moves further down by 3 nm Pd deposition, which causes the SBH to be lower (lower resistance) initially, so with H<sub>2</sub> adsorption, the relative change in resistance becomes much larger. Sensing experiments were carried out using the 3 nm Pd functionalized chemi-diodes, with the H<sub>2</sub> concentration varying from 1000 to 2 ppm, with exposure duration of 10 minutes, at a fixed reverse bias of -4 V.

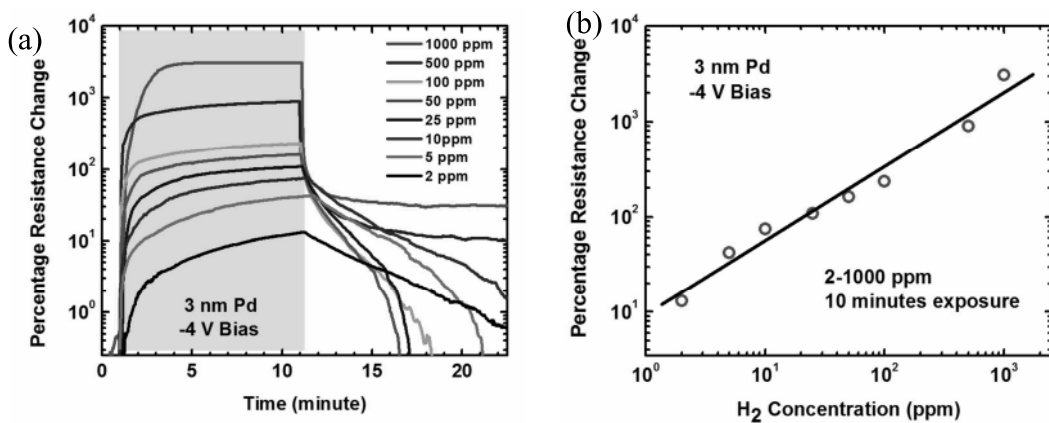


**Figure 4.5** (a) Responses of 3 nm Pd functionalized graphene/p-Si device for H<sub>2</sub> concentration ranging from 1000 to 2 ppm (pink box) for 10 minutes exposure. (b) Sensor response as a function of H<sub>2</sub> concentration plotted in log-log scale. The solid straight line shows a least square fit to the data.

We find from figure 5(a) that sensitivity changes from 13.55% to 3088% as the H<sub>2</sub> concentration increases from 2 to 1000 ppm, where, the statistical errors were within ~10% of the mean values of sensitivity plotted in the graph. The response time is increased from 90 sec to 270 sec as the H<sub>2</sub> concentration changes from 1000 to 2 ppm. The recovery times are very fast, taking only 1 sec to recover to 50% of the maximum resistance change for 1000 ppm H<sub>2</sub>. Interestingly, the full recovery times are faster for the smaller concentrations of H<sub>2</sub> as can be seen from Figure 4.5(a), with complete recovery observed within a few

minutes for most concentrations other than 500 and 1000 ppm. This is probably due to the larger amount of H<sub>2</sub> adsorption by thicker Pd layer (3nm) functionalized chemi-diode compared to that of 1nm Pd functionalized graphene/p-Si device, which recovered completely as shown in Figure 4.4(d). The plot of sensitivity versus H<sub>2</sub> concentration [Figure 4.5(b)] indicates that the sensitivity in these sensors varies almost linearly with the H<sub>2</sub> concentration when both of them are plotted in logarithmic scale. The work function change of the Pd layer (and hence the SBH) is expected to vary linearly with log of H<sub>2</sub> concentration [40], while the sensor current, which controls the sensitivity, varies exponentially with the SBH. Thus, the log-log relationship between H<sub>2</sub> concentration and sensitivity is expected to be linear as observed in Figure 4.5(b). It is noteworthy that this exponential behavior is different from that obtained previously from graphene and graphene nanoribbon network based chemiresistive H<sub>2</sub> sensors, where the sensitivity got saturated at higher H<sub>2</sub> concentration (plotted in log scale) [11,13,45]. This difference in the sensing response, is however expected, and follows from the difference in the detection principles of the chemiresistor and the proposed reverse biased chemi-diode sensor as discussed above.

To further validate H<sub>2</sub> sensing mechanism of the diode sensor, capacitance-voltage (C-V) measurement has been carried out at three different stages, as fabricated device, after 2 nm Pd deposition and finally, after 1000 ppm H<sub>2</sub> exposure. The C-V measurements were performed on the sensor using HP 4284A Precision LCR Meter with a frequency range of 20 Hz to 1 MHz. A four terminal pair scheme was used for the measurements. The ac signal amplitude was chosen as 50 mV (rms) with a frequency of 3 kHz. The dc reverse bias was

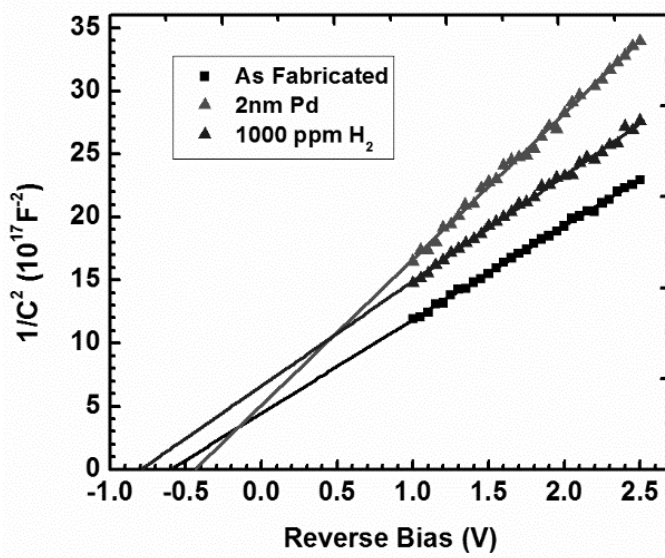


**Figure 4.6** Capacitance-Voltage (C-V) plot of Pd-functionalized graphene/p-Si Schottky diode and effect of H<sub>2</sub> exposure.

varied from 1 to 2.5 V. As obtained measurements results are plotted in the widely used  $1/C^2 - V$  format to extract the built-in voltage ( $V_{bi}$ ) using the following equation,

$$1/C^2 = 2(V_{bi} + V_R)/(q \epsilon_s N_{A/D}) \quad (4.2)$$

Here, q is the electronic charge,  $\epsilon_s$  is the semiconductor permittivity, and  $N_{A/D}$  is the acceptor/donor doping [46]. Figure 4.6 is showing the C-V plots which are linearly extrapolated and  $V_{bi}$  are determined as 0.58 eV for the initial diode, 0.44 and 0.79 eV after 2 nm Pd deposition and 10 minutes exposure to H<sub>2</sub>, respectively. The graphene/p-Si SBH is given as,  $\phi_B = V_{bi} + (E_F - E_V)$ , where  $E_F$  is the Fermi level and  $E_V$  is the valance band edge of Si.  $E_F - E_V$  is estimated to be  $\sim 0.2$  eV for the p-type Si used from the resistivity of  $1 - 10 \Omega\text{cm}$  specified by the manufacturer. Thus, graphene/p-Si diode SBH becomes 0.78 eV, which is in good agreement with earlier results. [33,47] The SBH determined from C-V measurement is higher than that obtained from I-V measurements, i.e. 0.78 and 0.65 eV, respectively for graphene/p-Si diodes. The difference can arise partly from the uncertainty

in determining  $E_F - E_V$ , and also from Schottky barrier inhomogeneity and additional leakage paths at the junction, which generally underestimates the SBH determined from I-V measurements [32-34]. The SBH reduced from 0.78 to 0.64 eV after 2 nm Pd deposition due to its p-type doping of graphene as explained before. After 10 minutes of 1000 ppm H<sub>2</sub> exposure, the SBH jumped up from 0.64 to 0.99 eV due to PdH<sub>x</sub> formation which decreases the hole density in graphene and increases the interface barrier for carrier flow. Large increase in SBH also substantiates the huge response of the diode sensor towards H<sub>2</sub> compared to similar electron donor molecular species NH<sub>3</sub> which has been reported in reference 48.

Finally, both the Pd- and Pt-functionalized graphene/Si diode sensors showed good repeatability in terms of response and recovery when subjected to several cycles of H<sub>2</sub> exposure and recovery in air as shown in Figure 4.7(a) and (b), respectively.

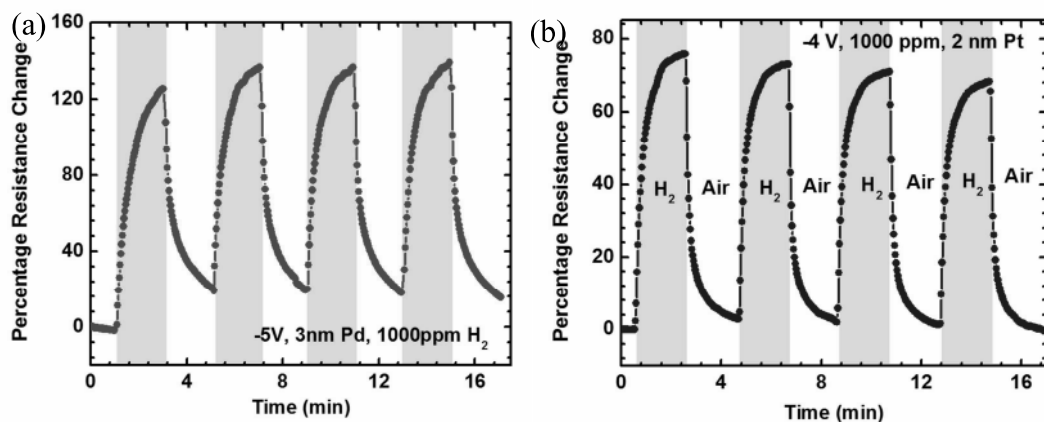


**Figure 4.7** Sensor response for repetitive cycles of 1000 ppm H<sub>2</sub> exposure (pink box) and recovery in air for (a) Pd-functionalized, and (b) Pt-functionalized graphene/p-Si Schottky diode sensor. Both the sensors are showing excellent response and recovery even in 2 minutes of exposure and recovery time.

In conclusion, Pt and Pd functionalized graphene/p-Si heterojunction chemi-diode H<sub>2</sub> sensor with very high sensitivity, down to sub-ppm level, has been demonstrated. These heterojunction diode sensors show at least an order of magnitude higher response compared to the graphene based chemiresistor type sensors for both Pd and Pt-functionalization, due to exponential dependence of the reverse bias diode current on the molecular adsorption induced SBH change. In addition, the reverse bias operation of these sensors enables them to perform sensing with very low power consumption. The magnitude of the reverse bias can be effectively utilized to modulate the Fermi level of graphene, and hence the graphene/Si SBH, leading to tunable sensitivity over a wide range of analyte concentration.

# Detection of individual gas molecules adsorbed on graphene

F. SCHEDIN<sup>1</sup>, A. K. GEIM<sup>1</sup>, S. V. MOROZOV<sup>2</sup>, E. W. HILL<sup>1</sup>, P. BLAKE<sup>1</sup>, M. I. KATSNELSON<sup>3</sup>  
AND K. S. NOVOSELOV<sup>1\*</sup>

<sup>1</sup>Manchester Centre for Mesoscience and Nanotechnology, University of Manchester, Manchester, M13 9PL, UK

<sup>2</sup>Institute for Microelectronics Technology, 142432 Chernogolovka, Russia

<sup>3</sup>Institute for Molecules and Materials, University of Nijmegen, 6525 ED Nijmegen, Netherlands

\*e-mail: Konstantin.Novoselov@manchester.ac.uk

Published online: 29 July 2007; doi:10.1038/nmat1967

The ultimate aim of any detection method is to achieve such a level of sensitivity that individual quanta of a measured entity can be resolved. In the case of chemical sensors, the quantum is one atom or molecule. Such resolution has so far been beyond the reach of any detection technique, including solid-state gas sensors hailed for their exceptional sensitivity<sup>1–4</sup>. The fundamental reason limiting the resolution of such sensors is fluctuations due to thermal motion of charges and defects<sup>5</sup>, which lead to intrinsic noise exceeding the sought-after signal from individual molecules, usually by many orders of magnitude. Here, we show that micrometre-size sensors made from graphene are capable of detecting individual events when a gas molecule attaches to or detaches from graphene's surface. The adsorbed molecules change the local carrier concentration in graphene one by one electron, which leads to step-like changes in resistance. The achieved sensitivity is due to the fact that graphene is an exceptionally low-noise material electronically, which makes it a promising candidate not only for chemical detectors but also for other applications where local probes sensitive to external charge, magnetic field or mechanical strain are required.

Solid-state gas sensors are renowned for their high sensitivity, which—in combination with low production costs and miniature sizes—have made them ubiquitous and widely used in many applications<sup>1,2</sup>. Recently, a new generation of gas sensors has been demonstrated using carbon nanotubes and semiconductor nanowires (see, for example, refs 3,4). The high acclaim received by the latter materials is, to a large extent, due to their exceptional sensitivity allowing detection of toxic gases in concentrations as small as 1 part per billion (p.p.b.). This and even higher levels of sensitivity are sought for industrial, environmental and military monitoring.

The operational principle of graphene devices described below is based on changes in their electrical conductivity,  $\sigma$ , due to gas molecules adsorbed on graphene's surface and acting as donors or acceptors, similar to other solid-state sensors<sup>1–4</sup>. However, the following characteristics of graphene make it possible to increase the sensitivity to its ultimate limit and detect individual dopants. First, graphene is a strictly two-dimensional material and, as such, has its whole volume exposed to surface adsorbates, which maximizes their effect. Second, graphene is highly conductive, exhibiting metallic conductivity and, hence, low Johnson noise even in the limit of no charge carriers<sup>6–9</sup>, where a few extra electrons

can cause notable relative changes in carrier concentration,  $n$ . Third, graphene has few crystal defects<sup>6–10</sup>, which ensures a low level of excess ( $1/f$ ) noise caused by their thermal switching<sup>5</sup>. Fourth, graphene allows four-probe measurements on a single-crystal device with electrical contacts that are ohmic and have low resistance. All of these features contribute to make a unique combination that maximizes the signal-to-noise ratio to a level sufficient for detecting changes in a local concentration by less than one electron charge,  $e$ , at room temperature.

The studied graphene devices were prepared by micromechanical cleavage of graphite at the surface of oxidized Si wafers<sup>7</sup>. This allowed us to obtain graphene monocrystals of typically 10 μm in size. By using electron-beam lithography, we made electrical (Au/Ti) contacts to graphene and then defined multiterminal Hall bars by etching graphene in an oxygen plasma. The microfabricated devices (Fig. 1a, upper inset) were placed in a variable temperature insert inside a superconducting magnet and characterized by using field-effect measurements at temperatures,  $T$ , from 4 to 400 K and in magnetic fields,  $B$ , up to 12 T. This allowed us to find the mobility,  $\mu$ , of charge carriers (typically,  $\approx 5,000 \text{ cm}^2 \text{ V}^{-1} \text{ s}^{-1}$ ) and distinguish between single-, bi- and few-layer devices, in addition to complementary measurements of their thickness carried out by optical and atomic force microscopy<sup>6–9</sup>. Figure 1a, lower inset, shows an example of the field-effect behaviour exhibited by our devices at room temperature. This plot shows that longitudinal ( $\rho_{xx}$ ) and Hall ( $\rho_{xy}$ ) resistivities are symmetric and antisymmetric functions of gate voltage,  $V_g$ , respectively.  $\rho_{xx}$  exhibits a peak at zero  $V_g$ , whereas  $\rho_{xy}$  simultaneously passes through zero, which shows that the transition from electron to hole transport occurs at zero  $V_g$  indicating that graphene is in its pristine undoped state<sup>6</sup>.

To assess the effect of gaseous chemicals on graphene devices, the insert was evacuated and then connected to a relatively large (5 l) glass volume containing a selected chemical strongly diluted in pure helium or nitrogen at atmospheric pressure. Figure 1b shows the response of zero-field resistivity,  $\rho = \rho_{xx}(B=0) = 1/\sigma$ , to NO<sub>2</sub>, NH<sub>3</sub>, H<sub>2</sub>O and CO in concentrations,  $C$ , of 1 part per million (p.p.m.). Large easily detectable changes that occurred within 1 min and, for the case of NO<sub>2</sub>, practically immediately after letting the chemicals in can be seen. The initial rapid response was followed by a region of saturation, in which the resistivity changed relatively slowly. We attribute this region to redistribution

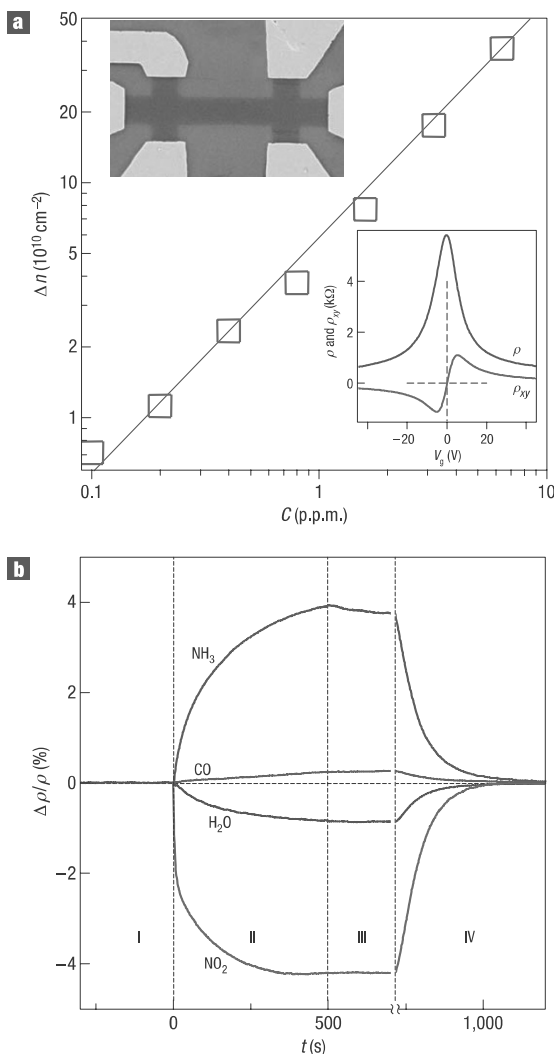


**Figure 1** Sensitivity of graphene to chemical doping. **a**, Concentration,  $\Delta n$ , of chemically induced charge carriers in single-layer graphene exposed to different concentrations,  $C$ , of  $\text{NO}_2$ . Upper inset: Scanning electron micrograph of this device (in false colours matching those seen in visible optics). The scale of the micrograph is given by the width of the Hall bar, which is  $1\ \mu\text{m}$ . Lower inset: Characterization of the graphene device by using the electric-field effect. By applying positive (negative)  $V_g$  between the Si wafer and graphene, we induced electrons (holes) in graphene in concentrations  $n = \alpha V_g$ . The coefficient  $\alpha \approx 7.2 \times 10^{10}\ \text{cm}^{-2}\ \text{V}^{-1}$  was found from Hall-effect measurements<sup>6–9</sup>. To measure Hall resistivity,  $\rho_{xy}$ ,  $B = 1\ \text{T}$  was applied perpendicular to graphene's surface. **b**, Changes in resistivity,  $\rho$ , at zero  $B$  caused by graphene's exposure to various gases diluted in concentration to 1 p.p.m. The positive (negative) sign of changes is chosen here to indicate electron (hole) doping. Region I: the device is in vacuum before its exposure; II: exposure to a 5 l volume of a diluted chemical; III: evacuation of the experimental set-up; and IV: annealing at  $150^\circ\text{C}$ . The response time was limited by our gas-handling system and a several-second delay in our lock-in-based measurements. Note that the annealing caused an initial spike-like response in  $\rho$ , which lasted for a few minutes and was generally irreproducible. For clarity, this transient region between III and IV is omitted.

of adsorbed gas molecules between different surfaces in the insert. After a near-equilibrium state was reached, we evacuated the container again, which led only to small and slow changes in  $\rho$  (region III in Fig. 1b), indicating that adsorbed molecules were

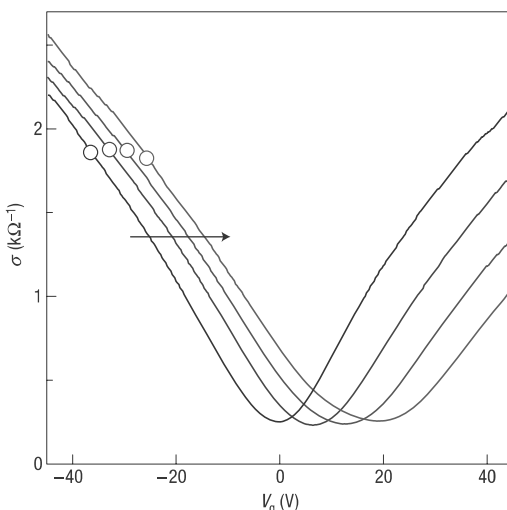


**Figure 2** Constant mobility of charge carriers in graphene with increasing chemical doping. Doping increased from zero (black curve) to  $\sim 1.5 \times 10^{12}\ \text{cm}^{-2}$  (red curve) due to increasing exposure to  $\text{NO}_2$ . Conductivity,  $\sigma$ , of single-layer graphene away from the neutrality point changes approximately linearly with increasing  $V_g$  and the steepness of the  $\sigma(V_g)$  curves (away from the neutrality point) characterizes the mobility,  $\mu$  (refs 6–9). Doping with  $\text{NO}_2$  adds holes but also induces charged impurities. The latter apparently do not affect the mobility of either electrons or holes. The parallel shift implies a negligible scattering effect of the charged impurities induced by chemical doping. The open symbols on the curves indicate the same total concentration of holes,  $n_i$  ( $\sim 2.7 \times 10^{12}\ \text{cm}^{-2}$ ), as found from Hall measurements. The practically constant  $\sigma$  for the same  $n_i$  yields that the absolute mobility,  $\mu = \sigma / n_i e$ , as well as the Hall mobility are unaffected by chemical doping. For further analysis and discussions, see the Supplementary Information.

strongly attached to the graphene devices at room temperature. Nevertheless, we found that the initial undoped state could be recovered by annealing at  $150^\circ\text{C}$  in vacuum (region IV). Repetitive exposure–annealing cycles showed no ‘poisoning’ effects of these chemicals (that is, the devices could be annealed back to their initial state). A short-time ultraviolet illumination offered an alternative to thermal annealing.

To gain further information about the observed chemical response, we simultaneously measured changes in  $\rho_{xx}$  and  $\rho_{xy}$  caused by gas exposure, which allowed us to find directly (1) concentrations,  $\Delta n$ , of chemically induced charge carriers, (2) their sign and (3) mobilities. The Hall measurements revealed that  $\text{NO}_2$ ,  $\text{H}_2\text{O}$  and iodine acted as acceptors, whereas  $\text{NH}_3$ ,  $\text{CO}$  and ethanol were donors. We also found that, under the same exposure conditions,  $\Delta n$  depended linearly on the concentration,  $C$ , of an examined chemical (see Fig. 1a). To achieve the linear conductance response, we electrically biased our devices (by more than  $\pm 10\ \text{V}$ ) to higher-concentration regions, away from the neutrality point, so that both  $\sigma = ne\mu$  and Hall conductivity,  $\sigma_{xy} = 1/\rho_{xy} = ne/B$ , were proportional to  $n$  (see Fig. 1a, lower inset)<sup>6–9</sup>. The linear response as a function of  $C$  should greatly simplify the use of graphene-based sensors in practical terms.

Chemical doping also induced impurities in graphene in concentrations  $N_i = \Delta n$ . However, despite these extra scatterers, we found no notable changes in  $\mu$  even for  $N_i$  exceeding  $10^{12}\ \text{cm}^{-2}$ . Figure 2 shows this unexpected observation by showing the electric-field effect in a device repeatedly doped with  $\text{NO}_2$ . V-shaped  $\sigma(V_g)$  curves characteristic for graphene<sup>6–9</sup>

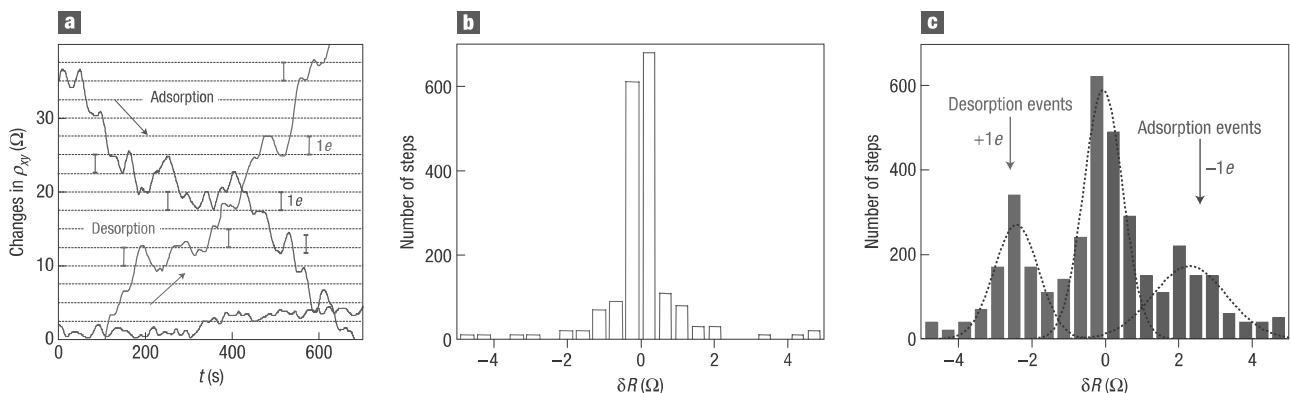


**Figure 3 Single-molecule detection.** **a**, Examples of changes in Hall resistivity observed near the neutrality point ( $|n| < 10^{11} \text{ cm}^{-2}$ ) during adsorption of strongly diluted  $\text{NO}_2$  (blue curve) and its desorption in vacuum at  $50^\circ\text{C}$  (red curve). The green curve is a reference—the same device thoroughly annealed and then exposed to pure He. The curves are for a three-layer device in  $B = 10\text{ T}$ . The grid lines correspond to changes in  $\rho_{xy}$  caused by adding one electron charge,  $e$  ( $\delta R \approx 2.5\text{ }\Omega$ ), as calibrated in independent measurements by varying  $V_g$ . For the blue curve, the device was exposed to 1 p.p.m. of  $\text{NO}_2$  leaking at a rate of  $\approx 10^{-3}\text{ mbar s}^{-1}$ . **b,c**, Statistical distribution of step heights,  $\delta R$ , in this device without its exposure to  $\text{NO}_2$  (in helium) (**b**) and during a slow desorption of  $\text{NO}_2$  (**c**). For this analysis, all changes in  $\rho_{xy}$  larger than  $0.5\text{ }\Omega$  and quicker than 10 s (lock-in time constant was 1 s making the response time of  $\approx 6$  s) were recorded as individual steps. The dotted curves in **b,c** are automated gaussian fits (see the Supplementary Information).

can be seen. Their slopes away from the neutrality point provide a measure of impurity scattering (so-called field-effect mobility,  $\mu = \Delta\sigma/\Delta ne = \Delta\sigma/e\alpha\Delta V_g$ ). The chemical doping only shifted the curves as a whole, without any significant changes in their shape, except for the fact that the curves became broader around the neutrality point (the latter effect is discussed in the Supplementary Information). The parallel shift unambiguously proves that the chemical doping did not affect scattering rates. Complementary measurements in magnetic field showed that the Hall-effect mobility,  $\mu = \rho_{xy}/\rho_{xx}B$ , was also unaffected by the doping and exhibited values very close to those determined from the electric-field effect. Further analysis yields that chemically induced ionized impurities in graphene in concentrations  $> 10^{12} \text{ cm}^{-2}$  (that is, less than 10 nm apart) should not be a limiting factor for  $\mu$  until it reaches values of the order of  $10^5 \text{ cm}^2 \text{ V}^{-1} \text{ s}^{-1}$ , which translates into a mean free path as large as  $\approx 1\text{ }\mu\text{m}$  (see the Supplementary Information). This is in striking contrast with conventional two-dimensional systems, in which such high densities of charged impurities are detrimental for ballistic transport, and also disagrees by a factor of  $>10$  with recent theoretical estimates for the case of graphene<sup>11–13</sup>. Our observations clearly raise doubts about charged impurities being the scatterers that currently limit  $\mu$  in graphene<sup>11–13</sup>. In the Supplementary Information, we show that a few-nanometre-thick layer of absorbed water provides sufficient dielectric screening to explain the suppressed scattering on charged impurities. We also suggest there that microscopic corrugations of a graphene sheet<sup>14,15</sup> could be dominant scatterers.

The detection limit for solid-state gas sensors is usually defined as the minimal concentration that causes a signal exceeding the sensors' intrinsic noise<sup>1–4</sup>. In this respect, a typical noise level in our devices,  $\Delta\rho/\rho \approx 10^{-4}$  (see Fig. 1b), translates into the detection limit of the order of 1 p.p.b. This already puts graphene on par with other materials used for most sensitive gas sensors<sup>1–4</sup>. Furthermore, to demonstrate the fundamental limit for the sensitivity of graphene-based gas sensors, we optimized our devices and measurements as described in the Supplementary Information. In brief, we used high driving currents to suppress the Johnson noise, annealed devices close to the neutrality point, where relative changes in  $n$  were largest for the same amount of chemical

doping, and used few-layer graphene (typically, 3–5 layers), which allowed a contact resistance of  $\approx 100\text{ }\Omega$ , much lower than for single-layer graphene. We also used the Hall geometry that provided the largest response to small changes in  $n$  near the neutrality point (see Fig. 1a, lower inset). In addition, this measurement geometry minimizes the sensitive area to the central region of the Hall cross ( $\approx 1\text{ }\mu\text{m}^2$  in size) and allows changes in  $\rho_{xy}$  to be calibrated directly in terms of charge transfer by comparing the chemically induced signal with the known response to  $V_g$ . The latter is important for the low-concentration region, where the response of  $\rho_{xy}$  to changes in  $n$  is steepest, but there is no simple relation between  $\rho_{xy}$  and  $n$ .

Figure 3 shows changes in  $\rho_{xy}$  caused by adsorption and desorption of individual gas molecules. In these experiments, we first annealed our devices close to the pristine state and then exposed them to a small leak of strongly diluted  $\text{NO}_2$ , which was adjusted so that  $\rho_{xy}$  remained nearly constant over several minutes (that is, we tuned the system close to thermal equilibrium where the number of adsorption and desorption events within the Hall cross area was reasonably small). In this regime, the chemically induced changes in  $\rho_{xy}$  were no longer smooth but occurred in a step-like manner as shown in Fig. 3a (blue curve). If we closed the leak and started to evacuate the sample space, similar steps occurred but predominantly in the opposite direction (red curve). For finer control of the adsorption/desorption rates, we found it useful to slightly adjust the temperature while keeping the same leak rate. The characteristic size,  $\delta R$ , of the observed steps in terms of ohms depended on  $B$ , the number of graphene layers and, also, varied strongly from one device to another, reflecting the fact that the steepness of the  $\rho_{xy}$  curves near the neutrality point (see Fig. 1a, lower inset) could be different for different devices<sup>6–9</sup>. However, when the steps were recalibrated in terms of equivalent changes in  $V_g$ , we found that to achieve the typical value of  $\delta R$  it always required exactly the same voltage changes,  $\approx 1.5\text{ mV}$ , for all of our  $1\text{ }\mu\text{m}$  devices and independently of  $B$ . The latter value corresponds to  $\Delta n \approx 10^8 \text{ cm}^{-2}$  and translates into one electron charge,  $e$ , removed from or added to the area of  $1 \times 1\text{ }\mu\text{m}^2$  of the Hall cross (note that changes in  $\rho_{xy}$  as a function of  $V_g$  were smooth, that is, no charge quantization in the devices' transport characteristics occurred—as expected). As a reference, we repeated

the same measurements for devices annealed for 2 days at 150 °C and found no or very few steps (green curve).

The curves shown in Fig. 3a clearly suggest individual adsorption and desorption events but statistical analysis is required to prove this. To this end, we recorded a large number of curves such as that in Fig. 3a ( $\approx 100$  h of continuous recording). The resulting histograms with and without exposure to  $\text{NO}_2$  are shown in Fig. 3b,c (a histogram for another device is shown in the Supplementary Information). The reference curves exhibited many small (positive and negative) steps, which gave rise to a ‘noise peak’ at small  $\delta R$ . Large steps were rare. On the contrary, slow adsorption of  $\text{NO}_2$  or its subsequent desorption led to many large, single-electron steps. The steps were not equal in size, as expected, because gas molecules could be adsorbed anywhere including the fringes of the sensitive area, which should result in varying contributions. Moreover, because of a finite time constant (1 s) used in these sensitive measurements, random resistance fluctuations could overlap with individual steps either enhancing or reducing them and, also, different events could overlap in time occasionally (such as the largest step on the red curve in Fig. 3a, which has a quadruple height). The corresponding histogram (Fig. 3c) shows the same ‘noise peak’ as the reference in Fig. 3b but, in addition, there are two extra maxima that are centred at a value of  $\delta R$ , which corresponds to removing/adding one acceptor from the detection area. The asymmetry in the statistical distribution in Fig. 3c corresponds to the fact that single-acceptor steps occur predominantly in one direction, that is,  $\text{NO}_2$  on-average desorbs from graphene’s surface in this particular experiment. The observed behaviour leaves no doubt that the changes in graphene conductivity during chemical exposure were quantized, with each event signalling adsorption or desorption of a single  $\text{NO}_2$  molecule.

In summary, graphene-based gas sensors allow the ultimate sensitivity such that the adsorption of individual gas molecules could be detected. Large arrays of such sensors would increase the catchment area<sup>16</sup>, allowing higher sensitivity for short-time exposures and the detection of active (toxic) gases in as minute concentrations as practically desirable. The epitaxial growth of few-layer graphene<sup>17,18</sup> offers a realistic promise of mass production of such devices. Our experiments also show that graphene is sufficiently electronically quiet to be used in single-electron detectors operational at room temperature<sup>19</sup> and in ultrasensitive sensors of magnetic field or mechanical strain<sup>20</sup>, in which the resolution is often limited by  $1/f$  noise. Equally important<sup>21,22</sup> is the demonstrated possibility of chemical doping of graphene by both electrons and holes in high concentrations without deterioration of its mobility. This should allow microfabrication of p-n junctions, which attract significant interest from the point of view of both fundamental physics and applications. Despite its short history,

graphene is considered to be a promising material for electronics by both academic and industrial researchers<sup>6,17,22</sup>, and the possibility of its chemical doping further improves the prospects of graphene-based electronics.

Received 14 May 2007; accepted 2 July 2007; published 29 July 2007.

## References

- Moseley, P. T. Solid state gas sensors. *Meas. Sci. Technol.* **8**, 223–237 (1997).
- Capone, S. *et al.* Solid state gas sensors: State of the art and future activities. *J. Optoelect. Adv. Mater.* **5**, 1335–1348 (2003).
- Kong, J. *et al.* Nanotube molecular wires as chemical sensors. *Science* **287**, 622–625 (2000).
- Collins, P. G., Bradley, K., Ishigami, M. & Zettl, A. Extreme oxygen sensitivity of electronic properties of carbon nanotubes. *Science* **287**, 1801–1804 (2000).
- Dutta, P. & Horn, P. M. Low-frequency fluctuations in solids:  $1/f$  noise. *Rev. Mod. Phys.* **53**, 497–516 (1981).
- Geim, A. K. & Novoselov, K. S. The rise of graphene. *Nature Mater.* **6**, 183–191 (2007).
- Novoselov, K. S. *et al.* Two dimensional atomic crystals. *Proc. Natl Acad. Sci. USA* **102**, 10451–10453 (2005).
- Novoselov, K. S. *et al.* Two dimensional gas of massless Dirac fermions in graphene. *Nature* **438**, 197–200 (2005).
- Zhang, Y., Tan, J. W., Stormer, H. L. & Kim, P. Experimental observation of the quantum Hall effect and Berry’s phase in graphene. *Nature* **438**, 201–204 (2005).
- Dresselhaus, M. S. & Dresselhaus, G. Intercalation compounds of graphite. *Adv. Phys.* **51**, 1–186 (2002).
- Ando, T. Screening effect and impurity scattering in monolayer graphene. *J. Phys. Soc. Jpn.* **75**, 074716 (2006).
- Nomura, K. & MacDonald, A. H. Quantum Hall ferromagnetism in graphene. *Phys. Rev. Lett.* **96**, 256602 (2006).
- Hwang, E. H., Adam, S. & Das Sarma, S. Carrier transport in two-dimensional graphene layers. *Phys. Rev. Lett.* **98**, 186806 (2007).
- Morozov, S. V. *et al.* Strong suppression of weak localization in graphene. *Phys. Rev. Lett.* **97**, 016801 (2006).
- Meyer, J. C. *et al.* The structure of suspended graphene sheets. *Nature* **446**, 60–63 (2007).
- Sheehan, P. E. & Whitman, L. J. Detection limits for nanoscale biosensors. *Nano Lett.* **5**, 803–807 (2005).
- Berger, C. *et al.* Electronic confinement and coherence in patterned epitaxial graphene. *Science* **312**, 1191–1196 (2006).
- Ohta, T., Bostwick, A., Seyller, T., Horn, K. & Rotenberg, E. Controlling the electronic structure of bilayer graphene. *Science* **313**, 951–954 (2006).
- Barbolina, I. I. *et al.* Submicron sensors of local electric field with single-electron resolution at room temperature. *Appl. Phys. Lett.* **88**, 013901 (2006).
- Bunch, J. S. *et al.* Electromechanical resonators from graphene sheets. *Science* **315**, 490–493 (2007).
- Zhou, C., Kong, J., Yenilmez, E. & Dai, H. Modulated chemical doping of individual carbon nanotubes. *Science* **290**, 1552–1555 (2000).
- Obradovic, B. *et al.* Analysis of graphene nanoribbons as a channel material for field-effect transistors. *Appl. Phys. Lett.* **88**, 142102 (2006).

## Acknowledgements

We thank A. MacDonald, S. Das Sarma and V. Falko for illuminating discussions. This work was supported by the EPSRC (UK) and the Royal Society. M.I.K. acknowledges financial support from FOM (Netherlands).

Correspondence and requests for materials should be addressed to K.S.N.

Supplementary Information accompanies this paper on [www.nature.com/naturematerials](http://www.nature.com/naturematerials).

## Author contributions

K.S.N. designed the experiment and carried out both experimental work and data analysis, A.K.G. suggested the research direction and wrote the manuscript, E.S. and P.B. made graphene devices, S.V.M. and E.W.H. helped with experiments and their analysis and M.I.K. provided theory support. All authors participated in discussions of the research.

## Competing financial interests

The authors declare no competing financial interests.

Reprints and permission information is available online at <http://npg.nature.com/reprintsandpermissions/>



# Graphene Schottky diodes: An experimental review of the rectifying graphene/semiconductor heterojunction



Antonio Di Bartolomeo

Dipartimento di Fisica "E. R. Caianiello" and Centro Interdipartimentale Nano-Mates, Università degli Studi di Salerno,  
Via Giovanni Paolo II, 132, I-84084 Fisciano (SA), Italy

---

## ARTICLE INFO

*Article history:*

Accepted 19 October 2015

Available online 30 October 2015

editor: G. E. W. Bauer

---

## ABSTRACT

In the past decade graphene has been one of the most studied materials for several unique and excellent properties. Due to its two dimensional nature, physical and chemical properties and ease of manipulation, graphene offers the possibility of integration with the existing semiconductor technology for next-generation electronic and sensing devices. In this context, the understanding of the graphene/semiconductor interface is of great importance since it can constitute a versatile standalone device as well as the building-block of more advanced electronic systems. Since graphene was brought to the attention of the scientific community in 2004, the device research has been focused on the more complex graphene transistors, while the graphene/semiconductor junction, despite its importance, has started to be the subject of systematic investigation only recently. As a result, a thorough understanding of the physics and the potentialities of this device is still missing. The studies of the past few years have demonstrated that graphene can form junctions with 3D or 2D semiconducting materials which have rectifying characteristics and behave as excellent Schottky diodes. The main novelty of these devices is the tunable Schottky barrier height, a feature which makes the graphene/semiconductor junction a great platform for the study of interface transport mechanisms as well as for applications in photo-detection, high-speed communications, solar cells, chemical and biological sensing, etc. In this paper, we review the state-of-the art of the research on graphene/semiconductor junctions, the attempts towards a modeling and the most promising applications.

© 2015 Elsevier B.V. All rights reserved.

---

## Contents

1. Introduction.....	2
2. The Schottky junction.....	2
3. Applications of Schottky diodes.....	11
4. Graphene .....	15
5. Experimental aspects of the graphene/semiconductor junction.....	20
6. Modeling the graphene/semiconductor junction.....	28
7. Applications of graphene/semiconductor Schottky diodes.....	31
8. Van der Waals heterostructures with 2D layered semiconductors.....	46
9. Conclusions.....	52
References.....	53

---

E-mail address: [antonio.dibartolomeo@fisica.unisa.it](mailto:antonio.dibartolomeo@fisica.unisa.it).

where  $\tau$  is the time scale for carrier injection from the contact,  $T(E)$  is the transmission probability over the zero bias barrier  $\phi_B^0$ ,  $D(E) = D_0 |E|$  is the graphene density of states of Eq. (73),  $f_g$  and  $f_s$  are the Fermi functions of graphene and the semiconductor, respectively. Eq. (95) can be quite easily evaluated under the simplifying assumptions that  $\phi_B^0 \gg kT$  (the condition needed for rectification) and that carriers with energy greater than the Schottky barrier are transmitted, while those with energy lower than  $\phi_B^0$  are reflected, i.e.

$$T(E) = \begin{cases} 1 & \text{for } E \geq \phi_B^0 \\ 0 & \text{for } E < \phi_B^0 \end{cases}. \quad (96)$$

With these assumptions Eq. (95) can be written as

$$J = -\frac{e}{\tau} D_0 \int_{\phi_B^0}^{+\infty} E \left( \frac{1}{e^{(E-E_F)/kT} + 1} - \frac{1}{e^{(E-E_{FS})/kT} + 1} \right) dE. \quad (97)$$

As can be seen in Fig. 17, for transmitted electrons  $E - E_F \approx E - E_{FS} \geq \phi_B^0 \gg kT$ . Then, the Fermi distributions can be approximated by a Boltzmann distribution,  $(e^{(E-E_F)/kT} + 1)^{-1} \approx e^{-(E-E_F)/kT}$ , and

$$J = -\frac{e}{\tau} D_0 (kT)^2 \left( \frac{\phi_B^0}{kT} + 1 \right) e^{-\phi_B^0/kT} (e^{E_F/kT} - e^{E_{FS}/kT}). \quad (98)$$

When a bias V is applied to graphene with respect to semiconductor, then  $E_F - E_{FS} = -eV$  and Eq. (98) ultimately yields an equation formally identical to the ideal diode one:

$$J = J_0 (e^{eV/kT} - 1), \quad (99)$$

where the reverse current  $J_0$  depends on  $T$ ,  $\tau$  and  $V$ :

$$J = \frac{e}{\tau} D_0 (kT)^2 \left( \frac{\phi_B^0}{kT} + 1 \right) e^{-\phi_B^0/kT} e^{E_F/kT} = \frac{e}{\tau} D_0 (kT)^2 \left( \frac{\phi_B^0}{kT} + 1 \right) e^{-\phi_B/kT}. \quad (100)$$

Here, as in Eq. (92),  $\phi_B = \phi_B^0 - E_F(V)$  is the bias dependent SBH. According to Eq. (100), the Richardson constant is now

$$A^* = \frac{e}{\tau} D_0 k^2 \left( \frac{\phi_B^0}{kT} + 1 \right), \quad (101)$$

and depends on  $\tau$ , on the temperature as well as on the ZB SBH.  $\tau^{-1}$  is the injection rate of carriers from the contact to graphene (which is also the injection rate from graphene to the semiconductor) and is related to the coupling energy which controls the contact resistance (larger coupling energy corresponds to lower contact resistance). According to this model the injection rate from contact to graphene plays a key role in the transport properties of a G/S junction.

## 7. Applications of graphene/semiconductor Schottky diodes

(a) *Photodetectors*. A general overview of state-of-the-art photodetectors based on graphene (and other two-dimensional materials) was recently published by Koppens et al. [157]. Here we solely focus on photodetectors based on the graphene/semiconductor junction.

G/S Schottky diodes, when operated under reverse bias, can be used as photodetectors. In these devices, optical absorption takes place mainly in the semiconductor, and graphene (which is the exposed side of the junction) acts as optically transparent and anti-reflecting carrier collector. Absorption in graphene may become important at lower energies, e.g. for *IR* radiation.

Devices with graphene as optical absorber, as metal-graphene-metal (MGM) or FET structures, although highly appealing for ultrafast applications, suffer the limitations of the weak absorption ( $A \approx 2.3\%$ ) and the short lifetime of the order of picoseconds of photogenerated carriers in graphene [158,159] and the small effective photodetection area. These limitations result in low quantum efficiency and photocurrent responsivity, which in absence of a gain mechanism, remains limited to few tens mA/W ( $10 \div 20$  mA/W in the wavelength range  $400 \text{ nm} \leq \lambda \leq 1550 \text{ nm}$ ) [160–168]. In MGM devices, photo-generated carriers are captured by the electric field of the graphene–metal contacts, so only the small fraction of carriers generated very close to the contacts can be collected by the external circuit, while the rest of the carriers generated in graphene quickly recombines without any contribution to the external photocurrent. As a result, the effective photo detection area in MGM detectors is restricted to narrow regions adjacent to the graphene–metal interface. G/S Schottky diodes can effectively address these issues and produce a higher responsivity with the further benefit of a semiconductor compatible technology. In GSJs, light is absorbed in the thicker depletion layer of the semiconductor and the effective photo detection area is only restricted by the G/S contact area. The separation and transport of photo-generated carriers happen in the depletion layer of the semiconductor; if the photogenerated carriers are able to reach the graphene, they

will contribute to the photocurrent, independently of their excitation location along the sensible area and without the issue of the fast of  $e-h$  pair recombination in graphene. The important point here is that once photogenerated carriers are injected into graphene by the built-in electric field, these carriers can survive much longer than intrinsically photoexcited pairs in graphene. Their lifetime is related to the probability of being back injected into the semiconductor. Furthermore, if the semiconductor has a slow intrinsic recombination time, this can further reduce the recombination rate. As results the lifetime of carriers photogenerated at the G/S junction can be several order of magnitude higher (up to milliseconds) than the lifetime in graphene. Consequently, G/S Schottky junctions can have a higher quantum efficiency than MGM devices; the external quantum efficiency is in the range of 50% and 65% depending on the wavelength. Actually, as we will discuss in this section, GSJ can even have an intrinsic gain mechanism resulting in giant responsivity. Another important and unique feature of the GSJ is that responsivity can be tuned by the applied reverse voltage bias which makes these devices an ideal platform for fast and sensitive photodetection at variable brightness.

An extensive study on the photodetection properties of the G/n-Si Schottky junction was performed by X. An and coworkers [169] who investigated devices with CVD-grown monolayer and few-layer graphene on lightly doped n-Si (Fig. 18(a)), built with a scalable and CMOS-compatible fabrication process.

In the dark or under low power illumination (less than few  $\mu\text{W}$ ), the  $I-V$  characteristics of the junction follow the conventional photodiode behavior, as shown in Fig. 18(b), while at higher power some anomalies are observed (Fig. 18(c)). From detailed measurements of the Schottky barrier heights made using graphene, doped graphene and Ti/Au on Si, the Fermi level of the substrate was found pinned to the charge-neutrality level by its own surface states, with a Schottky barrier height  $\Phi_B \approx 0.8 \text{ eV}$ . Fig. 18(d) shows the energy band diagram at thermal equilibrium and in dark condition. Here graphene is assumed neutral and the Fermi levels of graphene and n-Si are denoted as  $E_F$  and  $E_{FS}$ , respectively. Incident photons generate  $e-h$  pairs in Si. In steady state, these excess carriers can be accounted for by introducing quasi-Fermi levels, separately for holes and electrons, near the valence and conduction band edges. The quasi-Fermi levels in Si, indicated as  $E_{FS,n}^q$  and  $E_{FS,p}^q$ , are defined such that, in the steady state, the concentrations of electrons  $n$  and holes  $p$  (including the photogenerated carriers) are:

$$n = N_c e^{-\frac{E_C - E_{FS,n}^q}{kT}}, \quad (102)$$

$$p = N_v e^{-\frac{E_{FS,p}^q - E_V}{kT}}. \quad (103)$$

At low power, the electron quasi-Fermi level of n-Si is slightly above the dark Fermi level  $E_{FS}$  and below  $E_C$ ,  $E_{FS} \leq E_{FS,n}^q < E_C$ , while the quasi-Fermi level for holes is below  $E_{FS}$  and above  $E_V$ :  $E_{FS} > E_{FS,p}^q > E_V$ . The separation of  $E_{FS,n}^q$  and  $E_{FS,p}^q$  increases with power, since the photogenerated  $e-h$  pairs (excess carriers) move  $E_{FS,n}^q$  and  $E_{FS,p}^q$  towards  $E_C$  and  $E_V$ , respectively.

Excess (photogenerated) holes from Si are injected into graphene and, similarly to Si, can be described by a quasi-Fermi level  $E_{F,p}^q < E_F$  ( $E_F$  is the dark Fermi level).  $E_F$  is lowered with respect to the bulk Si bands if a forward bias is applied to graphene, and so is  $E_{F,p}^q$  (Fig. 18(e)). However  $E_{F,p}^q$  cannot go lower than the quasi-Fermi level of silicon  $E_{FS,p}^q$ . This limits the number of accessible states for the injection of photogenerated holes from Si to graphene. At low incident powers, all the photogenerated holes can find accessible states in graphene to inject into, resulting in the conventional photodiode-like response.  $E_{F,p}^q$  lies between  $E_F$  and  $E_{FS,p}^q$ ,  $E_{FS,p}^q \leq E_{F,p}^q \leq E_F$  and no limiting condition is reached. Something different happens at high incident power, since there are not enough states in graphene for the photogenerated hole injection and the  $I-V$  behavior deviates from that of a conventional photodiode. Fig. 18(c) shows that for high light powers (up to 6.5 mW) there is a strong suppression of photocurrents close to  $V = 0$ , and a sharp rise and rapid saturation of photocurrents at low reverse biases. At forward bias, the lowering of the graphene Fermi level reduces the range for  $E_{F,p}^q$  which is easily brought to the limit  $E_{FS,p}^q$ . This greatly diminishes the number of accessible states for the photoexcited holes to inject into graphene from Si (the available states are those for which  $E_{F,p}^q \geq E_{FS,p}^q$ , corresponding to the small red area of Fig. 18(e)). Hence, under a forward bias, an increasing incident power quickly aligns  $E_{F,p}^q$  to the quasi-Fermi level of holes in Si,  $E_{F,p}^q = E_{FS,p}^q$ , and this condition stops further injection. Increasing the incident light power beyond this point disallows any further photogenerated holes to inject into graphene, and no change in the forward  $I-V$  characteristic is observed.

Vice-versa, a reverse bias on graphene lifts  $E_F$  with respect to the bulk silicon bands, opens up a larger number of accessible states for the holes to inject into (corresponding to the wider red part of the cone in Fig. 18(f)) and allows the collection of all the injected holes. As a result, the photocurrent, can completely recover under small reverse biases. At high reverse bias (with enough density of states to accommodate all photoexcited holes), the photocurrent is limited by the photogeneration rate which results in a saturated current, as shown in Fig. 18(c).

At high power, in the region of low reverse bias, the maximum allowed photocurrent (related to the condition  $E_{F,p}^q \geq E_{FS,p}^q$ ) can be controlled by the reverse bias itself. Fig. 18(c) shows that in this region the current is proportional to the reverse bias. This bias tunable photocurrent responsivity is an attractive feature of a GSJ photodetector which can be adapted for variable-brightness imaging.

An alternative explanation of the current suppression shown in Fig. 18(c) at low forward biases was proposed by Y. Song et al. [170], who considered the interfacial native oxide as a key knob to control the junction current, following a previous work on CNT/Si devices [171]. They suggested a model where the native oxide and the relatively low work function of

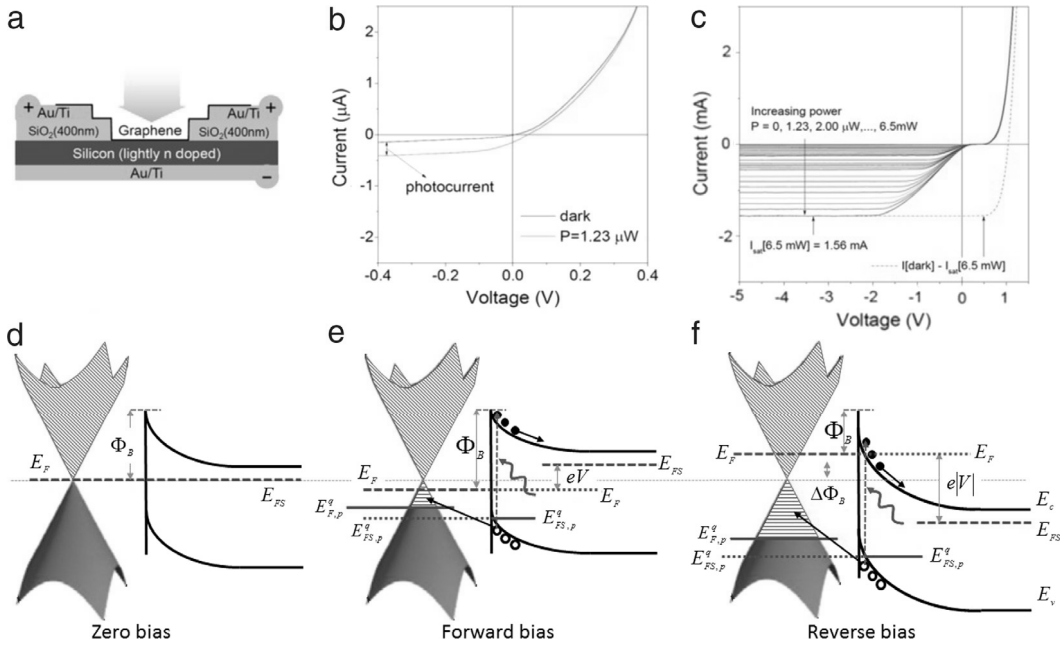


**Fig. 18.** (a) Schematic of the monolayer G/Si junction device of Ref. [169]. (b)  $I$ - $V$  curves of the device under darkness and weak illumination ( $P = 1.23 \mu\text{W}$ ,  $\lambda = 488 \text{ nm}$ ) showing a conventional photodiode-like behavior. (c) Deviation of the  $I$ - $V$  curves from a conventional photodiode response as the incident light power is increased up to  $P = 6.5 \text{ mW}$  (the red dashed line corresponds to the expected behavior of a conventional M/S diode). (d) Thermal equilibrium energy band diagram in darkness (the Fermi level of n-Si is pinned to the charge neutrality level of its own surface states and  $\Phi_B \approx 0.8 \text{ eV}$ ). Band diagrams and Fermi level  $E_F$  in darkness (dashed line), and quasi-Fermi level at high irradiation power ( $E_F^q$ , continuous line) under (e) forward and (f) reverse bias (the subscript S is used for silicon). (For interpretation of the references to colour in this figure legend, the reader is referred to the web version of this article.)

Source: Figure adapted from Ref. [169].

graphene cause significant carrier recombination that suppresses the photocurrent and results in a “s-shaped kink” at low bias as that observed in Fig. 18(c). We will review this model in the section on solar cells.

X. An et al. [169] demonstrated devices with high photovoltaic responsivity  $R_V$  (see Eq. (51)) exceeding  $10^{+7} \text{ V/W}$  at low power ( $\sim 10 \text{ nW}$ ). This very high responsivity renders G/Si Schottky diodes competitive devices for weak signal detection. At the lowest power of  $10 \text{ nW}$ , a  $NEP \sim 1 \text{ pW/Hz}^{0.5}$  was measured, confirming the low detection limit of these devices (a power as low as  $1 \text{ pW}$  can be detected above the noise level, when integrated over  $0.5 \text{ s}$ ). The corresponding detectivity (Eq. (55)) was  $D^* = 7.69 \cdot 10^{+9} \text{ Jones}$ . To further characterize the sensitivity of the device to small changes of incident power, the photovoltaic responsivity (or contrast sensitivity defined as  $dV_{ph}/dP_{in}$ ) was used, largely resulting independent of the device area and with the remarkable value of  $10^{+6} \text{ V/W}$  at low light intensities. In the photocurrent mode, at a given negative bias ( $-2 \text{ V}$ ), the response was found to remain linear over at least six decades of incident power, with a photocurrent responsivity (see Eq. (50)) up to  $225 \text{ mA/W}$ , which is at least 1–2 order of magnitude higher than that reported for Ge or Si photodetectors [172,173].

The time required to switch, when the incident light is turned on or off, was a few milliseconds, which is quite appealing for applications such as high speed photography, videography, etc.

The measured maximum quantum efficiency was  $EQE \sim 57\%$  over at least 4 order of magnitude of the incident power ( $10^{-3}$  to  $1 \text{ mW}$ ).

According to the proposed model, the device performances can be further improved by controlling the number of graphene layers and the graphene doping. Layer-thickening provides more states for injection of holes while doping the graphene can increase the sheet conductance thus improving the photocurrent responsivity.

F. Liu and S. Kar [174] recently demonstrated that devices similar to those of Ref. [169] can operate with ultra-high responsivity, up to  $10^{+7} \text{ A/W}$ , also in current mode. The devices, when operated in a “horizontal” (or high gain) configuration (see inset of Fig. 19(a)) rather than in vertical photodiode mode (see inset of Fig. 19(b)), are capable of an internal gain mechanism which they call Quantum Carrier Reinvestment (QCR). The QCR exploits the ultrafast transition of photogenerated carriers within graphene and the relatively large recombination time scale in the G/Si system, which can exceed a millisecond, to achieve ultrahigh quantum gain values. F. Liu and S. Kar [174] achieved quantum gains greater than  $10^{+6}$  electrons per incident photon and responsivities approaching  $\sim 10^{+7} \text{ A/W}$ .

Fig. 19(a) and (b) compare the responsivity of the same device when operated in high gain mode (a) and in photodiode mode (b). As we have already pointed out, the intrinsic photocurrent in graphene is limited to a few mA/W, while the photocurrent responsivity seen in Fig. 19(a) is many order of magnitude higher. This implies that the photocurrent of the

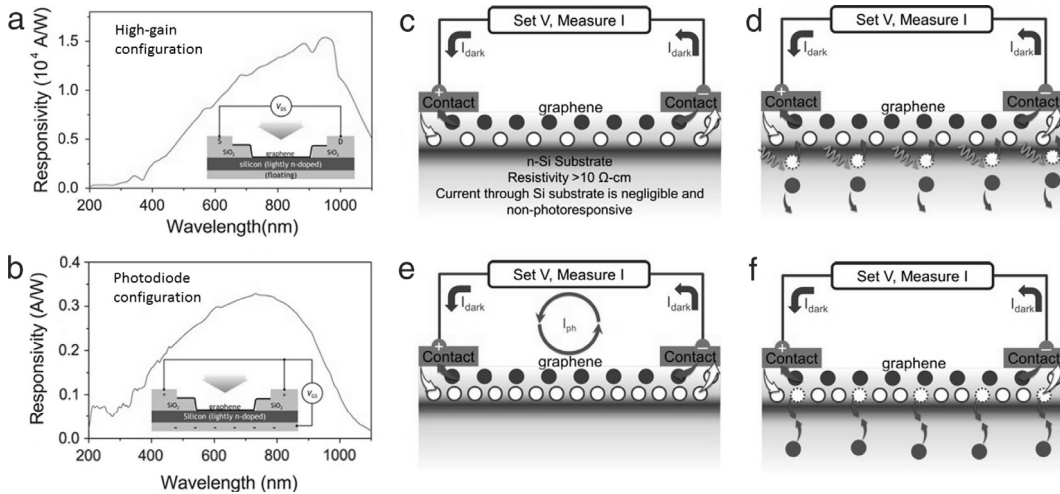


**Fig. 19.** Spectral responsivity of the device (shown in the inset) of Ref. [169] in (a) high-gain mode and (b) photodiode mode. A dramatic difference in their magnitudes is observed, even though the spectral shapes are similar. (c)–(e) Schematics outlining the gain mechanism at the G/Si junction (see text for explanation). Electrons and holes are denoted by dark and light circles, respectively. In (c) the dark current  $I_{dark}$  is due to intrinsic carriers in graphene. (d) Incident photons generate e-h pairs in the (lightly n-doped) silicon. Holes are swept into graphene by the built-in electric field of the junction and contribute to the current in the external circuit. Due to the fast transit time of graphene and the low probability of back injection in silicon, a single injected photocarrier can circulate several times (e) and substantially contribute to the current before recombine (f). This mechanism generate an internal quantum gain. (For interpretation of the references to colour in this figure legend, the reader is referred to the web version of this article.)  
Source: Figure adapted from [174].

device under study (no matter the configuration) has insignificant contributions from photocarriers generated in graphene. At the same time, the spectral shape of the responsivity curve in Fig. 19(a) is similar to that of Fig. 19(b), which is obtained in photodiode mode, clearly indicating that most of the photoinduced carriers originate in silicon and then get injected into graphene. The model developed to account for the far higher efficient photon-to-charge conversion in the gain-mode configuration is sketched in Fig. 19(c)–(f). This qualitative model is based on the photoinduced injection of carriers from Si into graphene. Compared to graphene, the lightly n-doped Si is highly nonconductive and under an applied external bias  $V_{DS}$  (as in Fig. 19(a)), and in darkness, a dark current  $I_{dark}$  flows through the external circuit due to the intrinsic carriers in graphene, as shown in Fig. 19(c). When light is shined on the device, photogenerated e-h pairs are separated by the built-in electric field: electrons move away into the body of silicon while holes get injected across the junction into graphene, as shown in Fig. 19(d). These additional holes, injected into graphene, add a current in graphene and in the external circuit, denoted as  $I_{ph}$  in Fig. 19(e). Due to the extremely rapid transit of carriers within graphene, a single injected hole can “circulate” (in the sense that a hole can be removed by an electrode and replaced by a hole injected by the other electrode) many times before another “equivalent” hole reverse-injects across the junction into silicon (Fig. 19(f)). During the lifetime of an injected hole carrier,  $\tau_r$ , a time scale determined by the quantum-mechanical probability of recombination, the hole can be “reinvested” several times into the external circuit, adding to the net photocurrent, and leading to a quantum gain (QCR mechanism).

The quantum gain is easily estimated by introducing the source-to-drain transit time  $\tau_t$ . The ratio of the recombination time  $\tau_r$  and  $\tau_t$  is the number of times that each injected carrier is “circulated” or “reinvested”. Reminding that the external quantum efficiency  $EQE$  (see Eq. (48)) is the number of carriers generated in Si and injected in graphene per incident photon, the quantum gain,  $QG$ , can be expressed as the  $EQE$  times the number of “reinvestments” of each hole:

$$QG = EQE \times (\tau_r / \tau_t). \quad (104)$$

On the other hand, in the simple diffusion transport model, the transit time can be related to mobility of graphene and to the external bias as

$$\tau_t = \frac{L}{v_d} = \frac{L}{\mu E} = \frac{L^2}{\mu V}, \quad (105)$$

where  $L$  is the inter-electrode distance. The photocurrent responsivity  $R_I$  (Eq. (50)) can be obtained as

$$R_I = EQE \frac{e}{h\nu} \tau_r \left( \frac{\mu V}{L^2} \right). \quad (106)$$

According to Eq. (106) the photocurrent response is linearly dependent on the applied drain-source bias, inversely proportional to the square of the device size, and directly proportional to the recombination time scale of the system. Each of these dependences were experimentally tested and verified in Ref. [174].

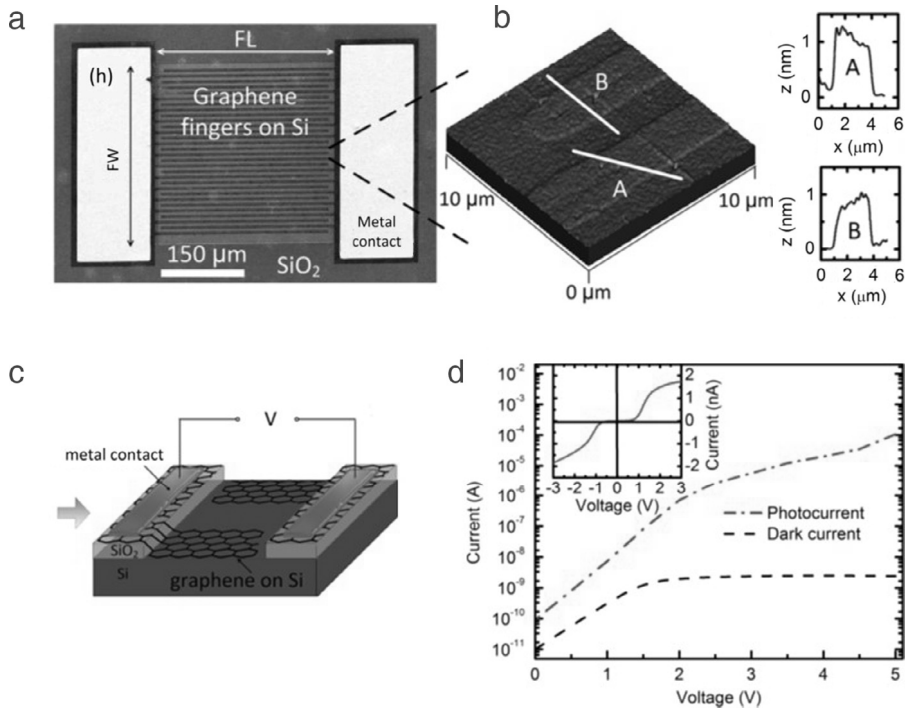


**Fig. 20.** (a) SEM image of a fabricated graphene/p-Si/graphene interdigitated device (finger width and spacing is 5 μm, active area is 300 × 300 μm<sup>2</sup>). (b) AFM image of patterned graphene fingers on Si. The height profiles along “A” and “B” lines are shown on the right (x is the distance along the lines and z is the height) (c) schematic of the interdigitated device. (d) Dark current and photocurrent as a function of bias voltage measured on an interdigitated photodetector with finger width and spacing of 10 μm and active area 400 × 400 μm<sup>2</sup>. The photocurrent is measured under 633 nm He-Ne laser illumination with 5.1 mW power and ∼830 μm spot size. The inset shows the dark I-V characteristic at positive and negative bias. (For interpretation of the references to colour in this figure legend, the reader is referred to the web version of this article.)  
Source: Adapted from Ref. [139].

The photodetecting properties of Cu-CVD graphene on *p*-type Si (heavily doped  $3 \times 10^{16} \text{ cm}^{-3}$ ) were reported in Ref. [139]. Photocurrent measurements were performed on interdigitated structures graphene/p-Si/graphene (Fig. 20).

The dark *I*-*V* characteristics at room temperature for the graphene/p-Si/graphene structure in the bias range from -3V to 3V, reported in the inset of Fig. 20(d), shows the typical behavior expected for two back-to-back Schottky diodes. The symmetry of the *I*-*V* indicates also that the Schottky junctions formed by opposite fingers are uniform.

To characterize the photoresponse of such photodetectors, the device was irradiated with a He-Ne laser (633 nm wavelength, 5.1 mW power, and ∼830 μm spot size) at room temperature. Fig. 20(d) shows the dark and the photocurrent of the same device as a function of voltage bias. Under illumination the current increases by about five orders of magnitude at 5V bias, from which a current responsivity  $R_I \approx 110 \text{ mA/W}$  was evaluated. This value is of the same order of magnitude of that obtained for graphene on n-Si, thus confirming the great potential of the interface G/Si for low power photodetection. An often reported metric for MSM (metal/semiconductor/metal) photodiodes is the normalized photocurrent-to-dark current ratio (*NPDR*) defined as

$$\text{NPDR} = \frac{I_{ph}}{I_{dark} \cdot P_{inc}} = \frac{R_I}{P_{inc}}, \quad (107)$$

which resulted  $4.55 \times 10^{4} \text{ mW}^{-1}$ , a value higher than that reported for similar devices fabricated with carbon nanotubes or Ti/Au on *p* and n-Si [175], due to a lower dark current.

Graphene-Si Schottky junctions have been proposed and demonstrated also as sensitive infrared (IR) detectors [176]. Infrared radiation in the C band of 1528–1561 nm and the L band 1561–1620 nm is of great interest and importance for optical communications. Differently from the detection of visible light where graphene is used as a transparent electrode and photoconversion happens in the Si depletion layer, at IR wavelengths the photocurrent is generated in graphene.

The great advantage of the G/Si diode is that all the photo-generated carriers in graphene, independent of their excitation location, have a similar chance to be separated and transferred to Si. In fact, whenever the generated carriers pass through the thin layer of graphene, they are swept by the electric field of Si depletion layer and contribute to the photocurrent. Furthermore, the relatively short lifetime of the photo-generated carriers of graphene is not a limitation in this case because the thin graphene layer is shorter than the mean recombination length of the carriers and the photo-generated carriers in graphene in all parts of the junction have high probability to be separated at the interface with Si before recombining.

M. Amirmazlaghani et al. [176], in particular, studied the effect of 1550 nm excitation laser on  $I$ - $V$  characteristics of an exfoliated G/p-Si Schottky junction. The reverse current of the junction (with a ZB Schottky barrier in the range 0.44–0.47 eV) increased under irradiation, corresponding to a photocurrent responsivity  $R_I = I_{ph}/P_{inc} = 2.8 – 9.9 \text{ mA/W}$  respectively at  $-5 \text{ V}$  and  $-15 \text{ V}$  reverse bias (the responsivity increased with reverse bias, but so did the level of noise). For comparison, all-Si detectors at the same wavelength have responsivity at least an order of magnitude lower [177].

Monolayer G/Si junctions were studied as near-infrared photodetectors also in Ref. [178], by fabricating a device able to operate at zero external voltage bias because of a strong photovoltaic behavior of the G/Si Schottky junction. A responsivity and detectivity  $R_I = 29 \text{ mA/W}$  and  $D = 3.9 \times 10^{11} \text{ cm} \sqrt{\text{Hz}}/\text{W}$  were measured at room temperature. The device showed great potential for low light detection with intensity down to  $\sim 1 \text{ nW cm}^{-2}$  at 10 K and a fast time response with speed of  $100 \mu\text{s}$ , which allowed the device following a fast varied light with frequency up to 2100 Hz.

The possibility of using G/Si junctions for near to mid-infrared detection was further investigated in Ref. [179], which demonstrated the use of in-plane absorption in a graphene-monolayer structure and the feasibility of exploiting indirect transitions in G/Si junction waveguides for mid-infrared detection. A graphene/silicon photodiode was formed by integrating graphene onto a silicon optical waveguide on a silicon-on-insulator (SOI). The waveguide enabled absorption of evanescent light that propagates parallel to the graphene sheet, and resulted in a responsivity as high as  $R_I = 130 \text{ mA/W}$  at 1.5 V bias for 2750 nm light at room temperature. A photocurrent dependence on bias polarity was observed and attributed to two distinct mechanisms for optical absorption, that is, direct and indirect transitions in graphene at 1550 nm and 2750 nm, respectively.

The potential of G/Si junctions for detection of THz frequencies is at the moment under study.

(b) *Solar cells.* Solar cells have become very popular in recent decades as alternative energy source, due to enormous energy obtained by earth from the sun ( $\sim 1.2 \times 10^{17} \text{ W}$ ). The current Si-based photovoltaic devices require high-quality raw materials and quite costly processing techniques to increase power conversion efficiency (PCE). Improvement in efficiency and cost reduction are relentlessly pursued to promote extensive solar cell applications. In this context, graphene is considered primarily as the conductive transparent electrode far long sought to replace the expensive ITO (indium tin oxide) (or FTO, fluorine tin oxide) electrode commonly used in solar cells for charge injection or collection. ITO suffers from many drawbacks, such as high cost, limited resource of indium, brittleness, etc., while graphene has the advantage of a better transparency to UV/blue light, a higher thermal conductivity as well as chemical stability, mechanical strength and flexibility. Furthermore, graphene has a low sheet resistance  $R_{sh}$ , which although depending on the production method, can be tuned by doping or by the number of layers. Thus, graphene enables easy tradeoff between high transparency and low  $R_{sh}$  requested in solar cell [180–184]. Graphene films with  $R_{sh}$  of few hundred ohm per square at about 80% optical transparency have been demonstrated on photovoltaic devices [185].

Other than as electrode, graphene microsheets have been dispersed into conjugated polymers to improve exciton dissociation and charge transport in organic solar cells [186,187]. Recent reviews on graphene applications in solar cells are found in Ref. [188–190].

In this section we focus on specific applications of the G/S junction as photovoltaic power generator. Photons absorbed in the semiconductor depletion layer generate  $e-h$  pairs that are separated by the built-in electric field and can be collected at the graphene and semiconductor contacts, thus generating power. In addition to the high transparency and to the controllable electrical conductivity, graphene allows the work function, and hence the characteristics of the GSJ, to be tuned as desired to optimize the solar cell PCE. G/Si solar cells are considered among the lower-cost candidates in photovoltaics due to the simple fabrication process and to the already competitive conversion efficiency, with values around  $\sim 10\%$  or  $\sim 15\%$  with the addition of antireflective coatings. The techniques developed for G/Si can be applied to other semiconductors (as GaAs, CdSe, etc.) with enhanced optical properties.

The photovoltaic properties of the carbon/Si interface were initially studied with the successful formation of p-type a-C/n-Si heterojunctions (a-C denotes a diamond-like amorphous carbon film) which showed efficiencies less than 1% at AM 1.5 [191–193]. Further development involved carbon nanotubes (CNTs)/Si junctions. The photovoltaic properties of films of CNTs on Si have been extensively studied with efficiencies varying from few percents to 14% [194–202]. Typically films of CNTs combines two types of heterostructures (Schottky and p-n), since both metallic and semiconducting nanotubes coexist in as-grown materials. A drawback of films composed of CNT networks is the interspace between bundles which reduces the conductivity of the film and the effective absorbing area, even though this can be advantageous for transparency. In this regard, graphene films are convenient since they can easily guarantee better electrical connection and full area coverage with superposing flakes.

One of the first studies on the G/n-Si Schottky junction for solar cells was reported by X. Li et al. [138] with devices consisting of a conform and continuous film of graphene sheets coated onto a patterned n-Si/SiO<sub>2</sub> substrate with Au contacts (Fig. 21(a)). Individual sheets were formed mostly by mono-layer, bilayer and few layer graphene. The graphene film served as transparent and anti-reflecting electrode for light illumination (reflection was reduced by  $\sim 70\%$  in the visible region and  $\sim 80\%$  in the near-IR) as well as active layer for  $e-h$  separation and hole transport. The built in field responsible for the photogenerated charge separation was estimated correspond to a barrier  $\Phi_i = 0.55 – 0.75 \text{ eV}$ . The corresponding band-structure is shown in Fig. 21(b). The  $I$ - $V$  characteristics of the devices were highly rectifying (rectification ratio of  $10^{+4} – 10^{+6}$ ) (Fig. 21(c)) and with  $\ln I$  nearly linear in the range of 0.1–0.4 V, corresponding to a diode ideality factor  $\eta = 1.57$ .

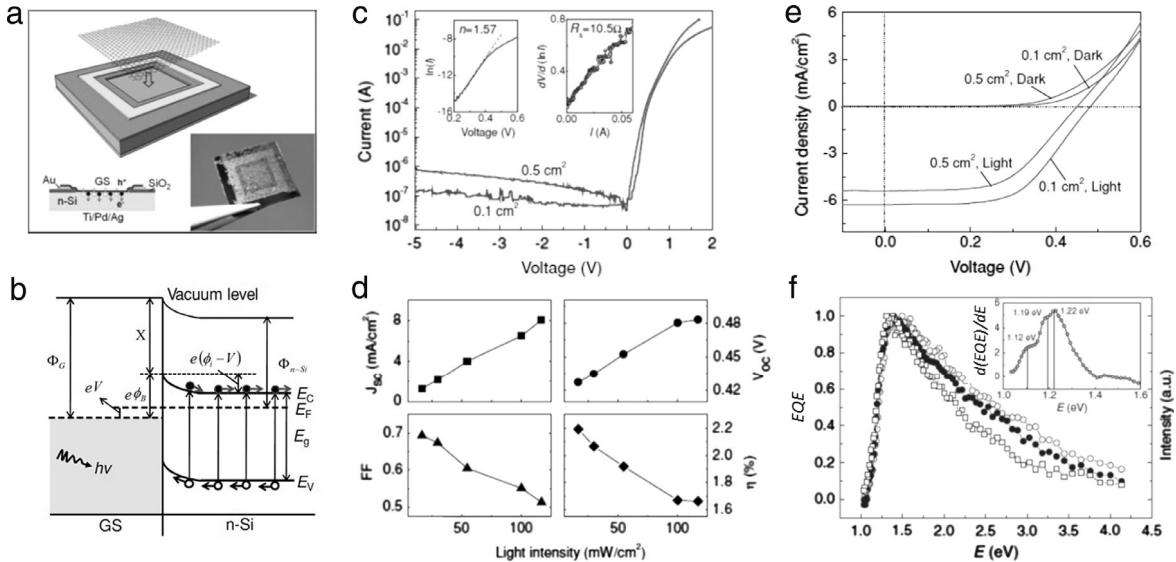


**Fig. 21.** Solar cell with films of graphene on n-Si. (a) Layout and a photograph of the devices. (b) Energy diagram of forward-biased G/n-Si Schottky junction upon illumination (c)  $I$ - $V$  characteristics of two devices ( $0.1\text{ cm}^2$  and  $0.5\text{ cm}^2$ ) showing excellent rectification. The insets show the ideality factor and the series resistance of the  $0.1\text{ cm}^2$  cell extrapolated from the forward linear region (d) Solar cell parameters ( $J_{\text{SC}}$ ,  $V_{\text{OC}}$ ,  $\text{FF}$ , and  $\text{PCE}$ ) vs. light intensity for the  $0.1\text{ cm}^2$  G/n-Si cell (e)  $J$ - $V$  curves of cells illuminated at AM1.5 equivalent light (f) External quantum efficiency (EQE) vs. photon energy (the inset shows the differential EQE spectrum) for cells with different area. (For interpretation of the references to colour in this figure legend, the reader is referred to the web version of this article.)

Source: Figure adapted from Ref. [138].

The reverse leakage current is nearly proportional to the area of the contact as the leakage current is restricted to the area of n-Si directly under the graphene sheet. The ZB Schottky barrier was estimated as  $0.75\text{--}0.8\text{ eV}$ . The photovoltaic properties of the cell were characterized at AM 1.5 illumination (Fig. 21(e)) yielding an open-circuit voltage  $V_{\text{OC}} = 0.42 \div 0.48\text{ V}$ , a short-circuit current density  $J_{\text{SC}} = 4 \div 6.5\text{ mA cm}^{-2}$  and a FF of 45%–56%, which corresponds to an overall  $\text{PCE} = 1 \div 1.7\%$  (Fig. 21(d)). Both  $V_{\text{OC}}$  and  $J_{\text{SC}}$  depend linearly on the light-intensity incident on the cell, consistent with a systematic increase in photogenerated carriers. The EQE vs photon energy is shown in Fig. 21(f); its first derivative, displayed in the inset, presents a sharp peak around  $1.2\text{ eV}$ , which corresponds to the fastest photon-to-electron conversion and can be assigned to the bandgap of silicon.

The PCE of these devices was almost an order of magnitude lower than that reported for CNTs on Si, but it was obtained without any balancing of the conductivity and the transparency of graphene sheets and no optimization of the G/Si interface. Ref. [138] also reported the successful series and parallel combination of the cells to multiply  $V_{\text{OC}}$  and  $J_{\text{SC}}$  respectively, thus checking the feasibility of arrays of solar panels.

The photovoltaic effect of a single graphene sheet on p or n-Si was observed by C.C. Chen et al. in Ref. [132]. Solar cells were also demonstrated with graphene on CdS [204] and CdSe [205] nanowires or nanobelts, with PCE up to 1.65% at AM 1.5.

Single layer G/n-Si solar cells with higher PCE were reported by X. Miao et al. [203]. Such cells exhibited a PCE of  $\sim 1.9\%$  under AM 1.5 illumination, which was increased till 8.6% with chemical doping by bis(trifluoromethanesulfonyl)-amide (TFSA),  $((\text{CF}_3\text{SO}_2)_2\text{NH})$ . TFSA, which has the advantage of environmental stability due to its hydrophobic nature, provides graphene with p-doping, thus reducing its sheet resistance and increasing its work function, without changing its optical properties [206]. The result is an increase of  $V_{\text{OC}}$ ,  $J_{\text{SC}}$ , FF and EQE which benefit from increased hole SBH and built-in potential, and reduced series resistance  $R_s$  (see the model of Fig. 5(e)).

The devices were fabricated by transferring CVD graphene grown on Cu foils on Si/SiO<sub>2</sub> substrates with pre-deposited Au/Cr contacts (Fig. 22(a) and (b)). Processing included exposure of bare Si to ambient air, for up to 2 h, to take advantage from oxygen passivation of dangling bonds that reduces surface states and improves the cell performance, as reported for conventional MIS cells [207]. The role of interfacial native oxide on Si is further discussed at the end of this sub-section. Doping of graphene was accomplished by spin-casting TFSA.

Fig. 22(c) shows the  $I$ - $V$  curves of pristine and TSFA-doped solar cells. The zero bias Schottky barrier, obtained from Eqs. (33) and (35) in the forward region of negligible  $R_s$ , is increased of about 0.1 eV by TFSA doping (from 0.79 eV to 0.89 eV). The doping down-shits the graphene Fermi level and increases the SBH and the built-in barrier,  $\Phi_i$  (Fig. 22(e) and (f)). Greater  $\Phi_i$  and widened depletion layer allow a more efficient collection of photogenerated charge. Furthermore, according to Eq. (60), the increase of the SBH results in a larger  $V_{\text{OC}}$  which is beneficial for EQE. Fig. 22(d) also shows an increase of  $I_{\text{SC}}$  for doped device and a higher FF, which can be partially attributed to the improvement in graphene electrical conductivity and the associated reduction of ohmic losses. The PCE is increased by doping from 1.9% to 8.6%. Doped devices also show a reduced ideality factor (from 1.6  $\div$  2.0 to 1.3  $\div$  1.5 range). Higher ideality factor is likely caused by charge

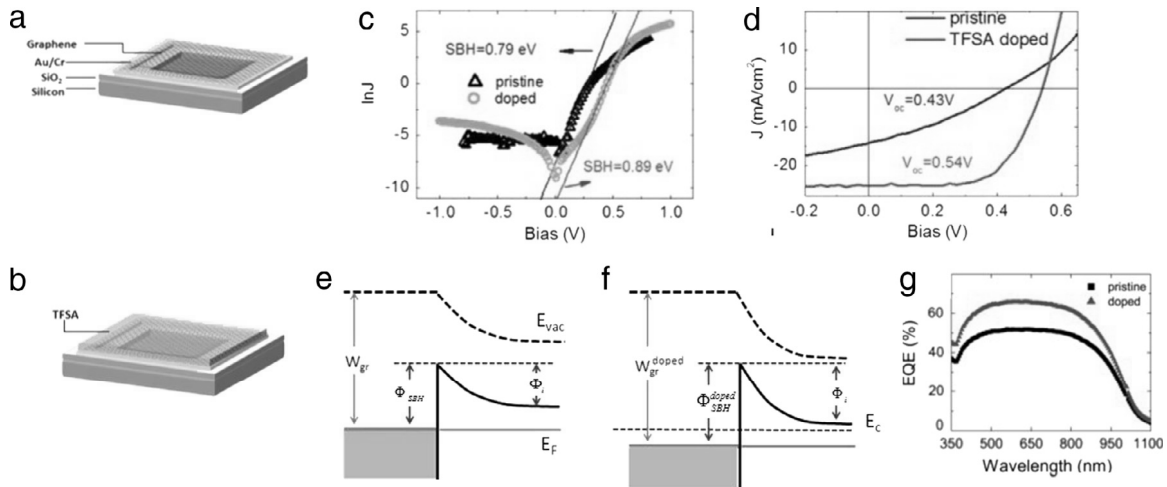


**Fig. 22.** Graphene/n-Si solar cell (a) without and (b) with TFSA (c)  $J$ - $V$  characteristics of pristine and doped solar cell. (d) Zoom in of  $J$ - $V$  characteristics. (e) band diagram at the G/n-Si interface before (e) and after doping of graphene (f). External quantum efficiency vs. wavelength (g). (For interpretation of the references to colour in this figure legend, the reader is referred to the web version of this article.)  
Source: Figure adapted from Ref. [203].

puddles on the graphene that are unintentionally formed during the process and which give rise to associated Schottky barrier inhomogeneities. The controlled doping of graphene by TFSA can possibly yield more uniformly doped regions, thus reducing the Schottky barrier inhomogeneity and the ideality factor.

Finally Fig. 22(g) shows the external quantum efficiency before and after doping. The EQE of the pristine cell is similar to state-of-the-art Si solar cells as expected since only Si absorbs and converts photons in  $e$ - $h$  pairs [208]. After TFSA-doping, the EQE is increased over 60%, representing a  $\sim 30\%$  enhancement compared to the pristine cell as result of the more efficient charge separation and charge collection and the reduced  $R_s$ , as we have pointed out.

The doping approach to enhance the PCE has been pursued in several other works. Some of them use nitric acid ( $HNO_3$ ) for its  $p$ -type chemical doping effect on graphene. Ref. [209] reported devices consisting of a heterojunction of graphene-based woven fabric on n-Si, where the graphene-based woven fabric served as transparent conducting window electrode, hole collector and anti-reflection layer. It was prepared by interlacing two sets of graphene micron-ribbons with ribbons passing each other essentially at right angles. By using a woven copper mesh as template, the graphene-based woven fabric grown from chemical vapor deposition retains the network configuration of the copper mesh. Such devices showed a PCE of  $\sim 3\%$  which after  $HNO_3$  doping was pushed to  $6.1\%$ .  $HNO_3$  is also used to dope graphene in Ref. [210] and Ref. [183] for devices made of graphene films on array of Si nanowires or nanoholes.

While doping is an attractive method to improve the cell efficiency, its impact is limited by the PCE of the starting junction. For this reason, it is highly desirable that the most ideal junction configuration is first established by optimizing key parameters as the optical transmittance and the sheet resistance of graphene sheets, before the doping.

A systematic effort in quantifying the impact of the sheet resistance and optical transmittance on the PCE of graphene-based solar cells was done by X. An et al. [211]. By varying the number of graphene layers, they studied the effects of optical transmittance and sheet resistance of graphene on  $V_{OC}$ ,  $J_{SC}$ ,  $FF$ ,  $EQE$ , etc., and through optimization of the cell they achieved  $PCE > 3\%$  without any doping and with near-100% internal quantum efficiency. Layer thickening favors carrier collection till the point it prevents a large fraction of light from reaching the junction, resulting in a worsening of the cell performance.

Moreover, they  $p$ -doped graphene via solutions of 1-pyrenecarboxylic acid (PCA) dissolved in methanol and powder of  $AuCl_3$  dissolved in Nitrometane to achieve a maximum PCE of  $\sim 7.5\%$  and a short-circuit current density exceeding  $J_{SC} = 424 \text{ mA cm}^{-2}$ .

To enhance light absorption Refs. [210,183] proposed devices made of graphene films on nanostructured Si prepared as Si nanowire (SiNW) and Si nanohole (SiNH) arrays on planar Si substrates (Fig. 23(a) and (b)). In comparison with planar Si, nanostructured silicon provides increased light absorption due to multiple reflections and more efficient charge separation/transport due to the larger surface area. Furthermore they tried to overcome some inherent limitations of Schottky type solar cells, as the large leakage current resulting from the low barrier height, by the addition of a thin organic layer to form graphene/organic/inorganic heterojunctions. Few layers CVD graphene films, doped with  $HNO_3$ , were deposited on passivated n-Si, with surface consisting of methyl-group terminated Si ( $CH_3-Si$ ). Methyl groups have been demonstrated to be highly effective in reducing carrier recombination velocity [212,213], with the benefit of higher photocurrent.

A thin layer of polymer poly(3-hexylthiophene) (P3HT) was coated on the surface of Si nanoarray (see Fig. 23(a) and (b)) with the purpose of acting as hole transport layer and electron blocking layer.

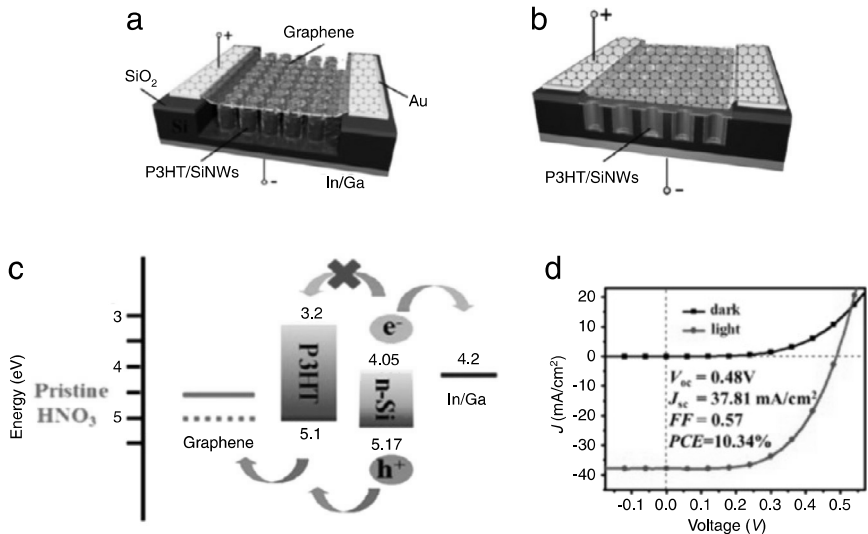


**Fig. 23.** Schematic illustrations of (a) graphene/P3HT/Si nanowire array and (b) graphene/P3HT/Si nanohole array hybrid devices. (c) Band diagram of the hybrid solar cell. (d)  $J$ - $V$  curve of a 5-layer Gr/P3HT (10 nm)/CH3-Si nanohole array hybrid device in darkness and under AM1.5 illumination. (For interpretation of the references to colour in this figure legend, the reader is referred to the web version of this article.)  
Source: Figure adapted from Ref. [183].

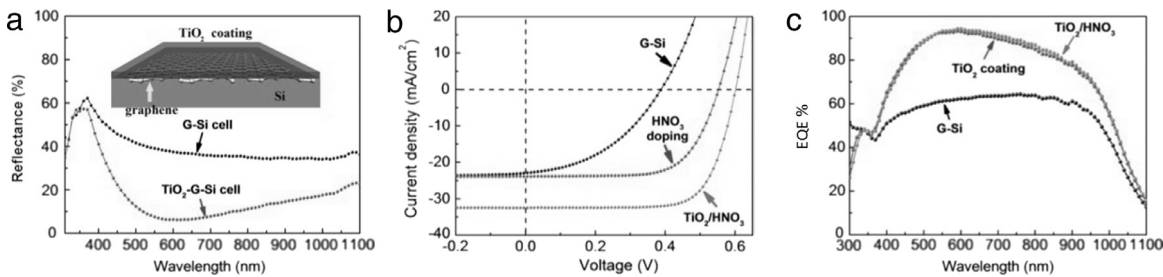


**Fig. 24.** (a) Light reflection spectra of a G/Si solar cell before (black) and after (red) coating the TiO<sub>2</sub> colloid. The inset shows a layout of the G/Si device covered by a thin layer of a TiO<sub>2</sub> colloidal solution. (b)  $J$ - $V$  characteristic of pristine G/Si device (black), after HNO<sub>3</sub> graphene doping and with the further addition of a TiO<sub>2</sub> anti-reflecting layer (d) EQE vs wavelength for pristine G/Si device and after doping/addition of TiO<sub>2</sub> layer. (For interpretation of the references to colour in this figure legend, the reader is referred to the web version of this article.)  
Source: Figure adapted from Ref. [217].

Fig. 23(c) shows the principle of charge separation and transport in the graphene/P3HT/Si hybrid solar cells. The lowest unoccupied molecular orbital (*LUMO*) and the highest occupied molecular orbital (*HOMO*) for P3HT are 3.2 and 5.1 eV, respectively, and their alignment with respect to Si and graphene is pictured in Fig. 23(c).  $e-h$  pairs photogenerated in Si which diffuse at the P3HT/Si interface are separated by the built-in electric field of the heterojunction. The band alignment favors the diffusion of photogenerated holes from Si to P3HT due to the positive LUMO- $E_c$  offset and their collection in the graphene anode. Diffusion of photoelectrons in same direction is suppressed by the HOMO- $E_c$  barrier energy, but is enhanced in the opposite direction, towards the In/Ga electrode (cathode). Therefore, the P3HT layer acts as the hole transport layer and as an electrons blocking layer and helps reducing the carrier recombination at the anode. The polymer layer increases the ratio  $I_{ph}/I_0$  and leads to a larger  $V_{OC}$ , according to Eq. (59).

Through passivation of the Si surface, optimization of the thickness of polymer layer, and controlling the graphene HNO<sub>3</sub> doping level and layer number, substantial improvement of device performance was achieved, leading to a PCE of 9.94% and 10.34% for SiNW and SiNH arrays-based hybrid solar cells, respectively. As an example, Fig. 23(d) depicts the typical  $J$ - $V$  curve of a 5-layer Gr/P3HT (10 nm)/CH3-Si nanohole array hybrid device measured under AM 1.5.  $J_{SC}$ ,  $V_{OC}$  and FF of the device are 37.8 mA cm<sup>-2</sup>, 0.48 V, and 0.57, respectively, yielding a PCE as high as 10.34%. We emphasize that  $J_{SC}$  of this device is close to the best value ( $J_{SC} = 42.7$  mA cm<sup>-2</sup>) obtained for the conventional single-crystalline Si solar cells [214–216]. Moreover, its EQE is ~85% on the wide spectrum range from ~400 to ~1000 nm.

To push the PCE of GSJ solar cells beyond the 10% threshold for commercialization, E. Shi et al. [217] proposed adding an antireflection layer on graphene. In such way they demonstrated cells with efficiency up to about 15%, a figure competitive with the best CNT-Si and with  $\mu$ -Si *p-n* cells [218,219]. E. Shi et al. [217] deposited a thin film (50–80 nm thick) by spin-coating a colloidal solution containing TiO<sub>2</sub> nanoparticles (3–5 nm) on the entire surface of graphene (a schematic of the device is shown in the inset of Fig. 24(a)). Graphene had been synthesized by CVD on Cu and transferred onto the ethanol-

cleaned surface of a n-Si substrate. The purpose was to increase light absorption by minimizing reflection from the polished Si surface, trying to enhance the limited antireflection action of graphene on Si. The choice of TiO<sub>2</sub> (vs. other materials) was determined by its refractive index, large bandgap, and easy production of a thin, uniform coating layer. Fig. 24(b) shows the light reflection spectrum of the device before and after TiO<sub>2</sub> coating. A relatively high reflectance of nearly 40% across the wavelength range of 400–1100 nm is initially observed. After coating, the light reflectance in the same wavelength range is significantly reduced, with a dip to about 10% in the visible region (500–800 nm). This result is the proof that a suitable refractive index and film thickness can strongly inhibit reflected light from polished Si surface.

Fig. 24(b) shows how the *J*–*V* characteristic of the G/Si cell, obtained immediately after etching the oxide layer, can be improved with HNO<sub>3</sub> doping and further enhanced with the TiO<sub>2</sub> layer. HNO<sub>3</sub> doping increases *V<sub>OC</sub>* and the *FF*, while the TiO<sub>2</sub> coating mainly enhances *J<sub>SC</sub>*: the combined effects rise the efficiency of the cell. After doping the cell had an efficiency of ~10%, that was enhanced to ~14.5% by the addition of the coating layer. TiO<sub>2</sub> too might act as *p*-type doping, and further increase *V<sub>OC</sub>*. The final TiO<sub>2</sub>–G/Si cell had *V<sub>OC</sub>* = 0.60 V, *J<sub>SC</sub>* = 32.5 mA/cm<sup>2</sup>, and *FF* of 73%. Fig. 24(c) shows that an *EQE* up to 90% is achieved with TiO<sub>2</sub> for the improved light absorption in Si.

To investigate the device stability, the TiO<sub>2</sub> coated cell was stored in air without further encapsulation for 20 days and it was demonstrated that the antireflection effect, as seen in the improvement of the short-circuit current density, was stable over long time.

Y. Song et al. in Ref. [170] studied the effect of native oxide at the G/Si interface and recognized that tuning the thickness of the oxide can increase the open circuit voltage and the efficiency (from 10.0% to 12.4%). Furthermore, with the addition of a TiO<sub>2</sub> anti-reflecting layer, as in Ref. [217], they achieved a PCE of 15.6%, which is the highest reported efficiency for graphene–silicon solar cells thus far.

They fabricated devices on n-Si (Fig. 25(a)) cleaned in diluted (50:1) HF (for 30 s) to remove any native oxide. Oxide was afterwards regrown by leaving the substrates in air for varying amounts of time. In air, native oxide grows logarithmically with time and in this study was measured to be ~5 Å after HF and ~15 Å after 2 weeks. *I*–*V* characteristics were measured for different oxide thicknesses and a distinctive s-shaped kink (Fig. 25(b)) was observed when the oxide thickness was >9 Å. The kink, which is often observed in G/S solar cell, reduces the *FF* and the *PCE* of the cell, and was found more pronounced when the thickness of the native oxide and illumination level were increased, while chemical doping of graphene was observed to suppress it.

Following these observations, Ref. [170] proposed a model which explains the s-shaped kink as due to significant recombination current that reduces the tunneling current through the G/SiO<sub>2</sub>/Si junction. As the oxide thickness augments, recombination dominates over tunneling and a clear s-shaped kink corresponding to a reduction of the junction current appears in the *I*–*V* characteristic.

Holes from photogenerated *e*–*h* in silicon, pulled towards graphene by the built-in electric field, in the presence of an interfacial oxide layer, pile up near the silicon/oxide interface. These holes either recombine with electrons either tunnel through the oxide barrier contributing to the junction current.

According to the Shockley–Read–Hall model (Ref. [46]), *e*–*h* recombination through interface trap states becomes important when the product of excess carriers *n<sub>s</sub>p<sub>s</sub>* at the interface (*n<sub>s</sub>* and *p<sub>s</sub>* are the electron and hole densities at the interface, respectively) becomes higher than the square of the intrinsic concentration, *n<sub>i</sub><sup>2</sup>*: *n<sub>s</sub>p<sub>s</sub>* ≥ *n<sub>i</sub><sup>2</sup>*. The recombination rate is limited by the less abundant carrier at the interface, that is electrons in this application. On the other hand the higher the concentration of holes at the oxide interface the greater is the tunneling current through the oxide. The tunneling current, which is the measured junction current, can be expressed as (Ref. [220])

$$J_t = \frac{4\pi m_p^* e}{h^3 N_v} (kT)^2 p_s e^{-\sqrt{\varsigma}\delta} (1 - e^{-\Delta E_{Fp}/kT}), \quad (108)$$

with *m<sub>p</sub><sup>\*</sup>* the effective mass of holes in silicon, *p<sub>s</sub>* the density of holes at the interface, *ξ* the average barrier height, *δ* the oxide thickness and *ΔE<sub>Fp</sub>* the difference between the quasi Fermi level of holes in graphene and in silicon, under illumination. *p<sub>s</sub>* and *ΔE<sub>Fp</sub>* are related by

$$p_s = p_{s0} e^{\Delta E_{Fp}/kT}, \quad (109)$$

where *p<sub>s0</sub>* is the equilibrium hole concentration at the interface.

So, as the concentration of holes *p<sub>s</sub>* at the surface increases, both recombination rate (for the higher *n<sub>s</sub>p<sub>s</sub>*) and tunneling current (for the higher *p<sub>s</sub>* and *ΔE<sub>Fp</sub>*) increase. However, these two mechanisms are competing to determine the total current at the junction: for a given illumination, more recombination means less tunneling, i.e. reduced junction current.

With this in mind, the qualitative behavior of the *I*–*V* curves can easily be understood. Fig. 25(c) shows the band diagram for reverse bias. Because of band-bending, the electron concentration at the interface is lowered and this strongly limits the recombination rate. In this case the pile up of holes at the interface favors tunneling and most of the separated holes from the photogenerated *e*–*h* pairs contribute to the junction current. At zero or forward bias (Fig. 25(d)), the electron concentration at the interface increases, and so does the recombination rate. At the same time, the hole concentration *p<sub>s</sub>* diminishes since holes recombine with the many available electrons. According to Eqs. (108) and (109) the tunneling current is reduced. This reduction is seen as a kink and a drop of the *FF* value in the *I*–*V* characteristic of the cell (Fig. 25(d)).

If the oxide is thinner than 10 Å, the condition *n<sub>s</sub>p<sub>s</sub>* ≥ *n<sub>i</sub><sup>2</sup>* is unlikely to be reached, given the high tunneling probability, and recombination remains negligible (unless *n<sub>s</sub>* becomes very large under significant forward bias) and no S-shaped kink

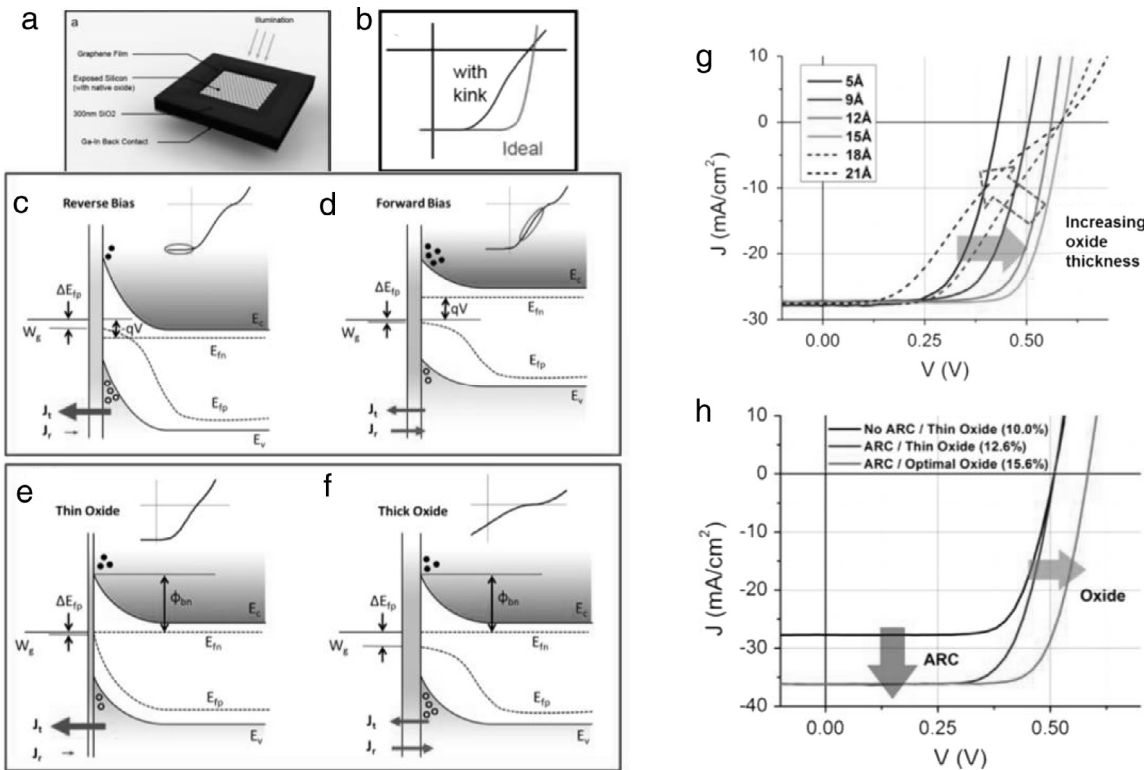


**Fig. 25.** Layout of a G/SiO<sub>2</sub>/n-Si solar cell (b) I–V characteristic with a kink commonly found in G/S solar cell devices. Energy band diagrams of a G/S junction with an interfacial oxide and under illumination, with surface electron/hole densities, in reverse (c) and forward (d) bias. Energy band diagrams and interfacial electron/hole densities for a device with thin (e) and thick (f) oxide. (g) I–V characteristic of the G/SiO<sub>2</sub>/n-Si solar cell (after doping) for varying oxide thickness. (h) Effect of oxide interface and anti-reflecting coating on the efficiency of the cell. (For interpretation of the references to colour in this figure legend, the reader is referred to the web version of this article.)  
Source: Figure adapted from Ref. [170].

is observed (Fig. 25(e)). With a thicker oxide, however  $p_s$  becomes larger. Therefore,  $n_s$  does not need to be as large to satisfy the  $n_s p_s \geq n_i^2$ . In this case recombination becomes dominant at lower forward biases and causes the reduction of the current and the appearance of a kink (Fig. 25(f)).

Doping of graphene affects band-bending at the interface. For an increased band bending,  $n_s$  decreases. Since the electrons limit the recombination rate, usually doping effectively suppresses the recombination contribution and thus the kink in the I–V characteristic.

From the technology of MIS (Metal-Insulator-Silicon) solar cells, it is well known that a thin layer of oxide, typically in the range 15–25 Å, is beneficial for efficiency. A thin oxide layer presents a tunneling barrier for electrons, which increases the effective SBH and reduces the reverse saturation current. According to Eq. (59), lower  $I_0$  means higher  $V_0$  until the oxide layer becomes thick enough to suppress the photogenerated current.

On the other hand a too thick oxide reduces the cell current. Therefore optimal performance can be achieved only with a balanced choice of the oxide thickness. Fig. 25(g) shows the effect of the oxide thickness on the I–V characteristics of the G/SiO<sub>2</sub>/Si cell after doping with AuCl<sub>3</sub> (sheet resistance of graphene 120 Ω/□ corresponding to a series resistance of ~9 Ω). Thickening the native oxide clearly increases  $V_0$  till a plateau value (0.59 V in Fig. 25(g)); after that, a further increase of the thickness (>15 Å in Fig. 25(g)), only results in the appearance of a kink, which limits the cell efficiency.

L. Lancellotti et al. [221] used the generalized equivalent circuit model of Fig. 5(e), with circuital parameters adapted to the physical properties of the graphene/semiconductor junction, to simulate devices made of graphene sheets with different numbers of layers  $N_L$ , coupled to n- and p-type Si or Ge. The PCEs of devices with different combinations of semiconductor substrate and number of layers of graphene showed values ranging from less than 1% to 11%. N- and p-type Si based devices show an opposite dependence of efficiency on  $N_L$ . For n-Si based devices the PCE increases with  $N_L$ , as a consequence of the augmented graphene workfunction which increases the SBH. The benefit of higher SBH compensates the transmittance reduction in this case. For p-Si based devices the efficiency decreases with increasing  $N_L$  for the combined effect of SBH lowering and transmittance reduction. According to Ref. [221], for  $1 \leq N_L \leq 4$ , p-Si based devices are preferable with respect to n-Si based ones, in agreement with some experimental results (e.g. Ref. [132]). This is due to the fact that the barriers of G/p-Si structures are higher and the diffusion length of electrons is larger than that of holes.

For  $N_L > 6$  the effect of a further increase of graphene thickness is only a transmittance reduction, and PCE decrease both n and p-Si.

The photovoltaic properties of graphene on p-Si substrate were investigated in Ref. [222]. Graphene was in this case obtained by borohydride ( $\text{NaBH}_4$ ) reduction of graphene oxide. Spin-coated films of rGO of various thickness were used to study the simplest rGO/p-Si heterojunction without any doping or special configuration.

A power conversion efficiency of 0.02% (possibly extended to 1.32% for optimized devices) with  $V_{\text{OC}} \approx 0.27$  V,  $I_{\text{SC}} \approx 0.11$  mA and  $FF \approx 0.12$  fill factor (under light illumination of  $1 \text{ kW/m}^2$ ) was demonstrated. A computational study was undertaken to investigate the influence of rGO thickness on PCE and a maximum efficiency of 6.74% was predicted using single-layer and high-quality rGO with optimized values of transmittance and sheet resistance.

Despite the low reported efficiency, rGO/Si heterojunction are still appealing devices due the simple and cheap fabrication technique and the higher transparency of r-GO [223].

(c) *Chemical sensors.* Graphene has an intrinsic high sensitivity for detecting chemical species. Its all-surface nature allows the  $\pi$ -conjugated system to be entirely exposed to external influences. Even the adsorption of a single molecule can affect the electronic properties of graphene, as demonstrated by Schedin et al. [224] in ultrahigh vacuum conditions.

Absorption of molecules can enable transfer of charge and modulate the graphene Fermi level. In a GSJ, molecules can affect the graphene conductivity, the SBH and have dramatic effects on the  $I$ - $V$  characteristics of the junction. These effects can be used for identification purpose or to measure the concentration.

Chemical sensors are highly required for environmental and air quality control, process monitoring, safety, etc. G/S Schottky junction have been proposed as cheap and highly performant new type of sensing platforms.

Most graphene based sensors reported so far are in the form of chemiresistor or chemical field effect transistors. In these sensors adsorbed molecules change the charge carrier density and hence the conductivity in direct proportion with their number [225–232]. However, the detection sensitivity of these sensors, for a specific analyte, is determined by the mobility of the carriers in graphene, and is largely affected by the substrate on which graphene is synthesized or transferred [233]. Devices, based on the utilization of a gate, can achieve higher sensitivity at the cost of design complexity, power consumption and more complicate fabrication process [234]. In addition, the mass production of devices with the required reproducibility can be challenging.

H.-Y. Kim et al. [235] successfully used monolayer G/Si diodes as sensors exposing graphene to liquids and gases. These sensors showed sensitivity to liquid and gaseous electron donor (ED) and acceptor (EA) substances, such as anisole, benzene, chlorobenzene, nitrobenzene, and gaseous ammonia. The G/Si junction parameters were found to be very sensitive to the charge transfer from various adsorbates. Any change introduced by exposure was quite reversible and stable in time, two important requisites to qualify G/Si diodes as sensors.

The devices studied in [235] were fabricated with graphene grown by CVD on Cu foils, transferred on n and p-type Si substrates, with preformed Ti/Au electrodes. Both n and p substrates formed a Schottky junction with graphene well described by thermionic emission with ideality factor and barrier height  $\eta \approx 1.41$  and  $\Phi_B \approx 0.79$  eV for n-Si and  $\eta \approx 1.31$  and  $\Phi_B \approx 0.74$  eV for p-Si.

The bare graphene surface of the G/Si junctions was exposed to various liquids, with droplet volumes of 60–120  $\mu\text{L}$ , covering the entire G/Si area. The analytes were exchanged by rinsing the chip with a solvent and blow-drying with nitrogen.

Fig. 26(a) shows the  $J$ - $V$  characteristics of a G/n-Si diode, after applying the aromatic molecules anisole, benzene, chlorobenzene, and nitrobenzene, which have increasing electron-accepting behavior. Different curves, with different ideality factors and SBHs, are obtained, depending on the molecule used. As shown in Fig. 26(b), the ideality factor decreases with stronger EAs for the G/n-Si diode (the opposite effect is observed for the p-Si case) while the SBH increases from 0.79 to 0.80 eV with stronger EAs (the SBH decreases from 0.75 to 0.73 eV for the p-Si devices). Similarly, changes were observed in the series resistance of the diode: when exposed to liquid aromatic molecules,  $R_S$  increased with EDs, and decreased with EAs, independent of the substrate type (Fig. 26(c)).

This behavior was explained by considering the doping difference between pristine and exposed (doped) graphene, as shown in the schematic band diagram of Fig. 26(d)–(f). Exposure to EDs causes extra electrons to be transferred to graphene with an up-shift of the Fermi level (i.e. a lowering of the SBH, Fig. 26(d)); conversely, EAs induce extra holes giving rise to an increase in the SBH because the Fermi level is downshifted (Fig. 26(f)). The liquid on graphene directly controls the SBH and the current of the G/Si junction, which can be used to evaluate the doping behavior of liquids and gases. Furthermore, the change in  $R_S$  is a way to determine the concentration of EAs or EDs in a neutral solvent.

H.-Y. Kim et al. [235] also demonstrated that G/Si junctions are suitable to determine the extent of charge transfer from gaseous molecules. They exposed G/p-Si devices to ammonia ( $\text{NH}_3$ , which is an electron donor) with concentrations from 0 to 8% in Ar (as for carbon nanotubes, one  $\text{NH}_3$  molecule has been predicted to induce 0.03 electrons onto graphene [236] and showed that the current drops (since  $\text{NH}_3$  increases the SBH) with increasing ammonia concentration while  $R_S$  increases linearly with  $\text{NH}_3$  concentration).

The percentile series resistance change:

$$S = \frac{\Delta R_S}{R_{S0}} \times 100\% \quad (110)$$

( $\Delta R_S = R_S - R_{S0}$  where  $R_S$  and  $R_{S0}$  are the series resistances with and without  $\text{NH}_3$ ), also referred to as sensor response, is plotted vs. time in Fig. 26(g), where the resistance changes are recorded for repeated  $\text{NH}_3$  injections (gray boxes) at various

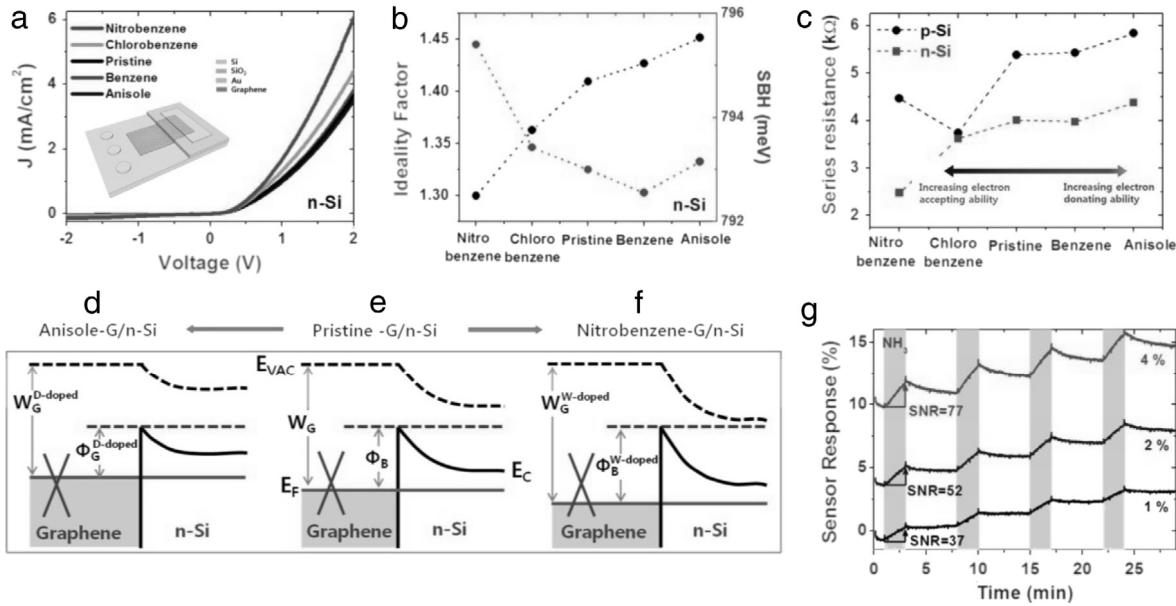


**Fig. 26.** (a)  $J$ - $V$  of  $G/n$ -Si sensor when exposed to various aromatic molecules (inset shows the schematic of the device) (b) Ideality factor and SBH of  $G/n$ -Si exposed to several liquids (c) Change of  $R_s$  for graphene exposed to various aromatic molecules. Schematic band diagram of the  $G/n$ -Si interface with electron donors (d), pristine state (e), and electron acceptors (f). (g) The  $G/p$ -Si sensor response vs. time at 1, 2, and 4% concentration of  $\text{NH}_3$ . (For interpretation of the references to colour in this figure legend, the reader is referred to the web version of this article.) Source: Figure adapted from Ref. [235].

concentrations. Each injection results in a resistance change with respect to gas atmosphere, with a delay mainly caused by the large volume of the sensing chamber. The steady up-shift is due to incomplete recovery between measurements since  $\text{NH}_3$  desorbs slowly from graphene at room temperature. The recovery time can be accelerated by vacuum annealing or UV illumination in fully integrated sensors.

The sensors of H.-Y. Kim et al. [235] uses the variation of the forward characteristic of the  $G/\text{Si}$  junction as detection principle. Some peculiarities of the  $G/\text{Si}$  junction are not fully exploited in this approach. On the other hand, using the reverse part of the  $G/\text{Si}$  Schottky junction can have the further advance of higher and bias tunable sensitivity and low power consumption, as proposed in Ref. [237].

The alteration of SBH due to molecular adsorption on graphene surface affects the junction current exponentially when operated in reverse bias, thus resulting in ultrahigh sensitivity. The reverse bias operation results in a drastic reduction in the operating power of the sensor (with consequent minimization of heating effects), which is highly desirable from the sensor design perspective. In addition, by operating the device in reverse bias, the work function of graphene, and hence SBH, can be controlled by the bias magnitude, leading to a wide tunability of the molecular detection sensitivity.

Fig. 27(a) shows a schematic diagram of a  $G/p$ -Si junction, which was fabricated on the same chip together with a graphene chemiresistor (a chemiresistor is a sensor based on the variation of resistance of graphene, which is inversely proportional to number of charge carriers in graphene). The  $I$ - $V$  characteristic, showing the usual rectifying behavior, is shown in Fig. 27(b) (note that the positive voltage bias is applied to the Si contact). The reverse saturation current increases monotonically with increasing bias magnitude (Fig. 27(c) and (d)), due to the graphene work function changes typical of  $G/S$  junction. Devices, fabricated both on p and n-substrate were exposed for different durations to dilute  $\text{NH}_3$  (electron donor) and  $\text{NO}_2$  gases (electron acceptor), both in dark and illuminated ambient conditions. The effect on the reverse characteristics of a  $G/p$ -Si is shown in Fig. 27(c) and (d).

With  $\text{NO}_2$  exposure, the current increases dramatically both in dark and illuminated conditions due to lowering of the SBH (Fig. 27(c)), while for  $\text{NH}_3$  exposure the reduction in current is rather small in dark, but is enhanced under illumination (Fig. 27(d)). Adsorption of  $\text{NH}_3$  increases the SBH, thus reducing the current. However, since the current is already small, the change in current is not very large. Under illumination, the reduction in current is much more noticeable since the current is increased significantly due to excess carrier generation and barrier lowering.

The sensor response was in this work equivalently expressed as percentage change of conductivity,

$$\sigma = \frac{\Delta\sigma}{\sigma_0} \times 100\%, \quad (111)$$

where  $\Delta\sigma = \sigma - \sigma_0$  with  $\sigma_0$  the initial sensor conductivity and  $\sigma$  the conductivity after exposure to an analyte gas.

Fig. 27(e) and (f) make direct comparison of the  $G/p$ -Si sensor with conventional graphene chemiresistor fabricated using the same transferred graphene film. The responses of the two sensors for 10 min  $\text{NO}_2$  exposure (shaded region) show that

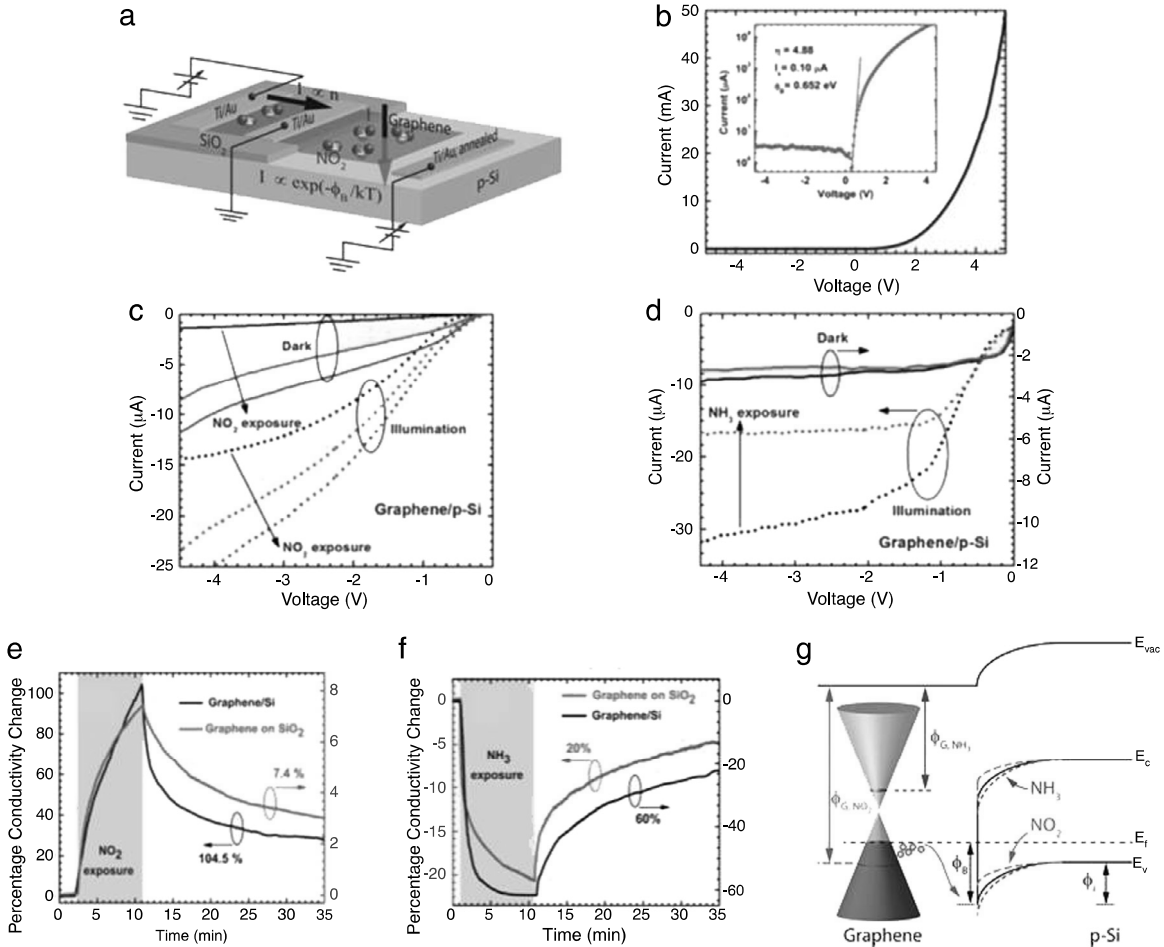


**Fig. 27.** (a) Device schematic and biasing of a graphene chemiresistor and a G/Si Schottky diode sensor fabricated on the same chip. (b)  $I$ – $V$  characteristics of a G/p-Si (the positive voltage bias is applied to the Si contact). (c–d) Reverse  $I$ – $V$  characteristics of G/p-Si diode in dark (solid curve) and under illumination (dotted curve) for different exposure times to (c)  $\text{NO}_2$  and (d)  $\text{NH}_3$ . The black curves represent pre-exposure characteristics, while the red and blue curves represent characteristics after 10 min and 30 min of gas exposure. (e–f) Comparison between  $\text{NO}_2$  (e) and  $\text{NH}_3$  (f) responses of graphene/p-Si (black line) and graphene chemiresistor (red line) fabricated on the same chip, side by side. The exposure duration (10 min) and bias voltage magnitude (4 V) is the same in both cases. (g) Energy band diagram of G/p-Si in three different conditions, showing reduction in SBH for  $\text{NO}_2$  and increase in SBH for  $\text{NH}_3$  exposure, as compared to the pre-exposure condition. (For interpretation of the references to colour in this figure legend, the reader is referred to the web version of this article.)

Source: Figure adapted from Ref. [237].

the chemiresistor conductivity changes by only 7.8% while that of the diode sensor changes by 104%, under the same applied bias magnitude of 4 V. The G/p-Si sensor has a response  $\sim 13$  times higher than the chemiresistor. For  $\text{NH}_3$  the difference in response is less dramatic, with a factor 3 enhancement.

Fig. 27(e) and (f) show that the conductivity changes faster with exposure to  $\text{NO}_2$  with respect to  $\text{NH}_3$ . This is explained by considering that the rate for charge transfer between adsorbed molecules and graphene decreases as the graphene Fermi level moves closer to the defect level introduced by the adsorbed molecules. The band diagram in Fig. 27(g) shows how  $\text{NO}_2$  and  $\text{NH}_3$  change the graphene–semiconductor band alignment. Initially, the graphene Fermi level, although slightly below the Dirac point, is closer to  $\text{NH}_3$  than to  $\text{NO}_2$ , therefore the charge transfer process between  $\text{NO}_2$  and graphene is much faster compared to  $\text{NH}_3$ . This is an important point since it suggests the way for optimized sensor design. The tunable Fermi level difference between graphene and semiconductor needs to be carefully chosen, keeping in mind the specific analyte to be detected. Ref. [237] demonstrates a sensing response down to 200 ppb of  $\text{NO}_2$  and 10 ppm for  $\text{NH}_3$ , and anticipates that with proper optimization of the sensor, higher detection sensitivity can be achieved. Furthermore, by exposing the detector to successive cycles they show good repeatability both for electron acceptor and donor gas molecules.

The tuning the SBH and barrier width at the tiny area of contact between graphene and  $\text{SnO}_2$  nanowires through the adsorption/desorption of gas molecules is at the origin of the outstanding  $\text{NO}_2$  gas sensing properties of monolayer G/ $\text{SnO}_2$  nanowire Schottky junction devices presented in Ref. [238]. The devices were prepared by directly growing single crystal  $\text{SnO}_2$  nanowires on interdigitated Pt electrodes via thermal evaporation. A CVD graphene monolayer was subsequently

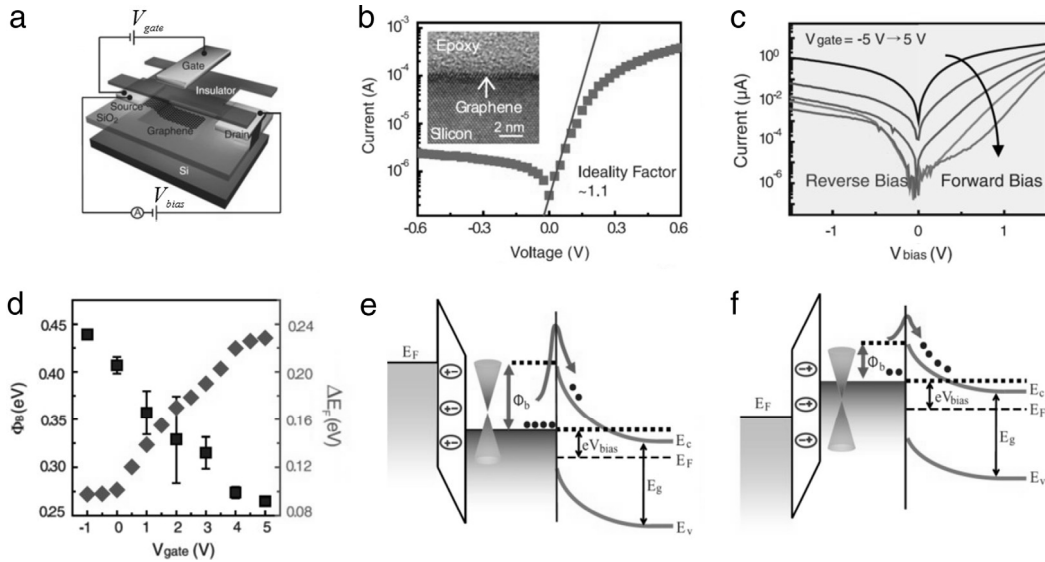


**Fig. 28.** Layout of a graphene barristor with top gate. (b)  $I$ - $V$  characteristic of graphene/p-Si barristor at  $V_{GS} = 0$  V. (c)  $I$ - $V$  characteristics of the p-type barristor for biases in the range  $-1.5$  V to  $1.5$  V and gate in the range  $(-5, 5)$  V by steps of  $2$  V. (d) SBH and field-effect induced Fermi level change,  $\Delta E_F$ . (e-f) Band diagram of graphene/n-Si barristor (from left to right: gate-insulator-graphene-silicon) for (e) negative voltage on the gate ( $V_{gate} < 0$  V and holes induced in graphene), and (f) positive voltage on the gate ( $V_{gate} > 0$  V and electrons induced in graphene). (For interpretation of the references to colour in this figure legend, the reader is referred to the web version of this article.) Source: Figure adapted from Ref. [239].

transferred on top of the nanowire chip. The Schottky junction-based sensor showed sensitivity to NO<sub>2</sub> gas with the remarkable detection limits of about 0.024 ppb at the low operating temperature of 150 C and bias voltage of 1 V and with a response/recovery time of less than 50 s.

#### (d) Barristors and other applications.

H. Yang et al. [239] proposed adding a top gate to the G/Si junction to control the Schottky barrier height and achieve a large modulation of the diode current (with on/off ratio up to  $10^{+5}$ ). They fabricated three terminal devices, of the type sketched in Fig. 28(a), which are known as graphene barristors, i.e. variable barrier devices, consisting of CVD graphene on hydrogen terminated n- or p-Si. An optimized transfer process was used to yield atomically sharp interfaces (as illustrated in the inset of Fig. 28(b)) with minimum number of atomic defects or silicon dioxide formation to prevent charge trapping sites. The purpose was to avoid Fermi level pinning at the G/Si interface and make the graphene  $E_F$  controllable by the gate through field effect.

Fig. 28(c) shows the  $I$ - $V$  characteristic of a G/p-Si barristor with zero voltage on the gate,  $V_{GS} = 0$  V. The ideality factor is very close to 1 confirming the high quality of the junction. It can be noticed that, both in forward and reverse bias, the G/p-Si current is strongly modulated by the gate voltage: by stepping  $V_{GS}$  from  $-5$  V to  $+5$  V reduces the current by a factor that can be as high as  $10^{+5}$ .

The barristor works on the principle that the SBH (Fig. 28(d)) and the current are modulated by the electric field of the gate [69]. The field of the gate induces holes or electrons in graphene (Fig. 28(e) and (f)) which shift the graphene Fermi level and modify the SBH. Fig. 28(d), referred to a G/n-Si barristor, shows that increasing  $V_{GS}$  decreases the SBH and increases the Fermi level variation in graphene,  $\Delta E_F$  ( $E_F$  is estimated from the measurement of Hall carrier density  $n$  and from Eq. (75)).  $\Delta E_F$  and the SBH are strictly correlated,  $\Delta \Phi_B = -\Delta E_F$ , confirming that the field-induced modulation of  $E_F$  in the absence of Fermi-level pinning is fully responsible for the variation of the SBH of the barristor.

H. Yang et al. [239] also demonstrated inverter and half-adder logic circuits by developing a fabrication process of n- and p-type G/Si barristors on a 150 mm wafers with CVD transferred graphene.

We quickly mention here a few other remarkable applications of the G/S Schottky junction.

M. Liu et al. [240] proposed a graphene based optical modulator for on-chip optical communications that has the advantage of compact footprint, low operation voltage and ultrafast modulation speed across a broad range of wavelengths. They fabricated a waveguide-integrated electro-absorption modulator based on monolayer graphene, which achieved modulation of the guided light at frequencies over 1 GHz. Integration of graphene with an optical waveguide greatly increased the interaction length through the coupling between the evanescent waves and graphene.

T. Gu et al. [241] used G/Si junctions as optoelectronic devices for coherent four-wave mixing.

Electrophoresis was used by K. Wu and coworkers [242] to fabricate G/Si electrodes which displayed high photoresponse and high stability in aqueous solution, thus constituting solar energy materials to use in aqueous solution.